

AD-A093 417

PITTSBURGH UNIV PA SCHOOL OF ENGINEERING

F/G 20/11

SCIENCE OF FRACTURE. (U)

OCT 80 M L WILLIAMS; C C YATES

F49620-78-C-0101

UNCLASSIFIED

SETEC-SF-80-048

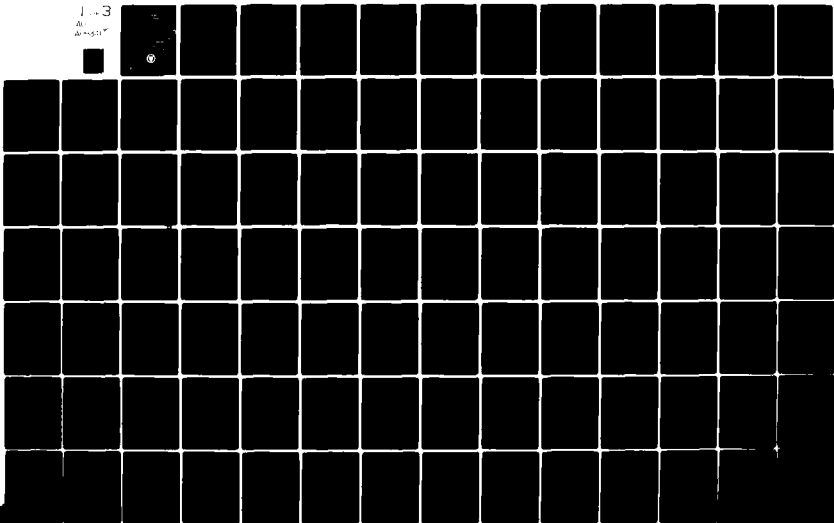
AFOSR-TR-80-1322

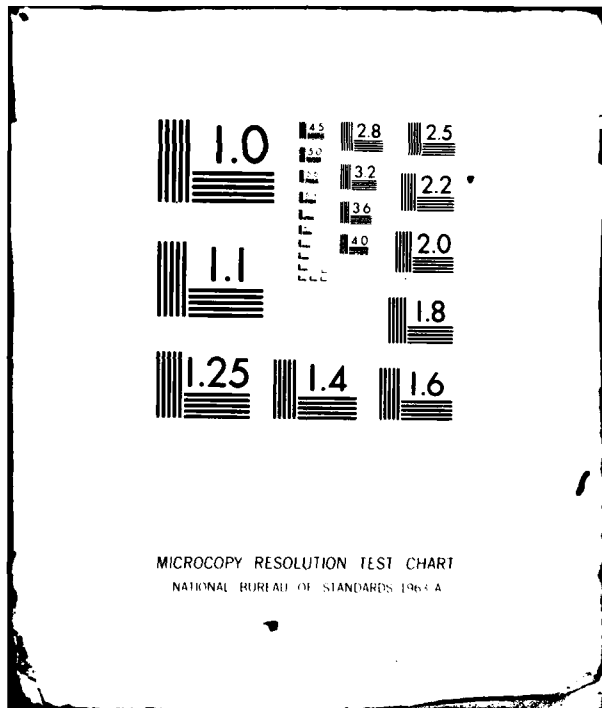
NL

1-3

AD-A093 417

AD-A093 417





MICROCOPY RESOLUTION TEST CHART
NATIONAL BUREAU OF STANDARDS 1963-A

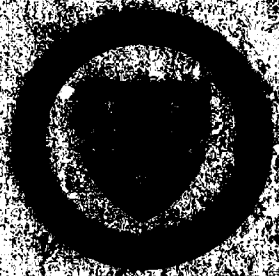
APR 20 1962

UNIV

AD A093417



SCHOOL OF ENGINEERING
University of Pittsburgh
Pittsburgh, Pennsylvania



ENC FILE COPY

80 12

~~UNCLASSIFIED~~

process upon the preparation of specimens made from standardized model materials representative of polymers and metals. Major results during this year include (1) additional analysis and development of a cracked Brazil specimen for deducing Mode II fracture toughness, (2) further parametric analysis of the effect of geometry in an embedded fiber or rod and the location of initial interfacial debonding from the matrix upon resulting adhesive fracture under load, (3) determination that initial phase of fracture in a cobalt-nickel alloy (MP 35) is probably void nucleation caused by grain boundary sliding during dynamic recrystallization, (4) plasma activated sintering can product apparently clean, active particle surfaces in silicon carbide powders, and (5) that it is realistic to plan generating two standard reproducible materials - one epoxy resin and one linear viscoelastic polymer - which can be used to relate chemical structure to mechanical properties.

S

~~UNCLASSIFIED~~

3

14 SETEC-SF-84-048 ✓

6 SCIENCE OF FRACTURE,
Annual Report

15 to

USAF Office of Scientific Research
Contract No. F49620-78-C-0101

7 Annual rept. 15 August 1979 to 30 September 1980

DTIC ELECTED
JAN 2 1981

10 M. L. Williams C.C. Yates
Principal Investigator

C. C. Yates
Project Coordinator

12 262

School of Engineering
UNIVERSITY OF PITTSBURGH
PITTSBURGH, PENNSYLVANIA
15261

16 2347

17 B2

14 22 October 1980

18 AFOSR

19 TR-84-1322

AIR FORCE OFFICE OF SCIENTIFIC RESEARCH (AFOSR)
NOTICE OF TRANSMITTAL TO DDC
This technical report has been reviewed and is
approved for public release IAW AFR 190-12 (7b).
Distribution is unlimited.
A. D. BLOSH
Technical Information Officer

408 140

JOB

PREFACE

Beginning in late 1978, the United States Air Force through the Office of Aerospace Research initiated a major science of fracture project at the University of Pittsburgh. The rationale for this special effort emerged from the recognition that, in some form, fracture analysis was becoming more and more generally employed as an engineering design tool to assess structural integrity. Fracture technology was increasingly sophisticated and complex. With the many static, fatigue, and spallation problems being attacked using different analytical, numerical, and experimental approaches, and the many theories - Griffith, Wiebull, maximum strain, and hydrodynamic - appropriate for metals, plastics, elastomers, ceramics, and composites, it seemed timely to inquire; is there sufficient experience to generalize the state-of-the-art, i.e. to provide the basis for a comprehensive fracture analysis discipline which is fundamentally consistent and complete?

The University of Pittsburgh program was designed to answer this question. The effort was organized in terms of five program categories each containing difficult but fundamental problems whose solution would significantly contribute to the desired unification. The five areas, to be construed in a broad sense, were

1. Analytical efforts and basic mechanism
2. Structure-property relationships
3. Numerical analysis methods
4. Instrumentation science
5. Technology transfer and applications

Primary emphasis during the early phases was upon the first two categories, with, simultaneously, a lower level of effort devoted to the latter three.

In a research sense, the program is high-risk and for this reason was initially proposed for a five-year period. Subsequently as a result of an administrative review by the Office of Scientific Research in May 1978, the technical effort was reduced and redirected to emphasize specific tasks structured in the more traditional manner. Consequently this report, covering the period 15 August 1979 to 30 September 1980, reflects a transition to more concentrated attention upon the first two of the above five areas.

M.L. Williams
C.C. Yates

October 1980
Pittsburgh, Pennsylvania

Table of Contents

	Page
1.0 Introduction.....	1
2.0 Status of Research.....	1
2.1 Analytic Efforts & Basic Mechanisms	
2.2 Structure Property Relations	
3.0 Statement of Work.....	6
4.0 Appendices - Task Reports - University of Pittsburgh.....	9
4.1 The 3-D Stress Singularity Problem.....	11
Dr. Colin Atkinson	
4.2 A Note on Stress Concentration and Energy Release Rates.....	33
4.3 Non-Local Elasticity and the Line Crack Problem.....	51
Dr. Colin Atkinson	
4.4 Combined Mode Fracture Via the Cracked Brazilian Disk Test.....	63
Dr. Colin Atkinson	
Dr. Ronald E. Smelser	
Mr. J. Sanchez	
4.5 Effects of Change in Crack Diameter on Critical Load - Preliminary Study.....	97
Dr. Shan Somayaji	
4.6 Bibliographic Overview of Composite Materials with Special Focus Upon Recent Publications on Fracture.....	111
Ms. Melba C. Williams	
4.7 Current Status and Future Prospects of Micromechanical Failure Theories for Fibrous Composites.....	121
Dr. Samuel B. Batdorf	
4.8 The Correlation of Viscoelastic Behavior with Fracture Properties.....	153
Dr. Donald J. Plazek	
4.9 Feasibility Demonstration of Melt Fracture Set-Up.....	163
Dr. Jan T. Lindt	
4.10 Fracture in Fully Plastic Bodies.....	171
Dr. Howard Kuhn	

Accession For	
NTIS	<input checked="" type="checkbox"/>
DTIC	<input type="checkbox"/>
Unannounced	<input type="checkbox"/>
Justification	
By	
Distribution/	
Availability	
Mail an	
Dist	Special
A	

4.11 Evaluation of Non-Oxide Based Silicon Ceramics..... 197
Dr. Richard L. Porter

5.0 Task Reports - Subcontracts

5.1 Structure Property Relationships for Time Dependent Fracture
of Polymers.....221

The University of Akron, Institute of Polymer Science
Dr. Frank N. Kelley
Dr. Patricia Dreyfuss

5.2 Numerical Studies of Crack Problems in Finite Elasticity....293
Dr. Eric Becker
Dr. Tinsley Oden

1.0 INTRODUCTION

The initial thrust of this program was directed toward the analysis of continuum fracture and the structural integrity as influenced by materials science, mechanics, and the loading environment. Five components of the program were identified.

1. Analytical Efforts and Basic Mechanisms
2. Structure-Property Relationships
3. Numerical Analysis Methods
4. Instrumentation Science
5. Technology Transfer and Applications

As a result of a USAF Office of Scientific Research administrative review, the technical work will be reduced and redirected to emphasize tasks structured in a more traditional task oriented manner. Consequently, during this current transition year, the work will reflect a concentration primarily upon the first two of the original five component parts.

2.0 STATUS OF RESEARCH

2.1 Analytical Efforts and Basic Mechanisms

The keystone for understanding fracture rests upon knowledge of mechanisms which control the process and upon the accompanying analytical work. This approach generally proves more cost-effective than an unguided testing program and engineering history. The method chosen is to study a class of idealized problems which are analytically tractable yet reveal key elements and mechanisms of fracture behavior.

Four illustrations were given in the original proposal. They were (i) the three-dimensional stress singularity, (ii) the elemental "toothpick" problem, (iii) resolution and comparison of fracture criterion for metals, polymers, and ceramics, and (iv) crack growth and environmental effects.

Nearly all of modern fracture analysis is based upon the characteristic inverse square root elastic stress singularity which was deduced for plane stress (thin plate stock) or plane strain (infinitely thick plates). Practically speaking, all plates have a finite thickness and when they fracture they usually exhibit important features which cannot be predicted using two-dimensional theory. Consequently, with success obtained using the simple plane stress result, it is appropriate to encourage continuing work on the still unsolved 3-D stress distribution. Our internal effort has been devoted, as planned, to maintaining contact with others attempting to solve this problem, particularly Dr. E.S. Folias (University of Utah), and Dr. T. Kawai (Institute of Industrial Science, University of Tokyo). In addition, Dr. Atkinson who has followed this work has prepared a commentary included herein as Appendix 4.1. At best the present situation can be described as unsettled; there is no present analytical solution which can be used confidently. Dr. Atkinson has also contributed a position paper (Appendix 4.2) dealing with the use of strain energy release rates in connection with the mathematically important problem of discontinuous elastic stress singularities which occur, for example, when a crack suddenly appears at a 90 degree corner. The order of singularity in this latter case jumps discontinuously from its uncracked 90 degree geometry to the stronger - 1/2 value characteristic of the zero degree, free-sided crack geometry. The present conclusion is that there is no viable answer to the problem: the transition from no-crack to crack remains fundamentally discontinuous. The analogy to a circular hole in a plane stress specimen can be drawn. The stress at a circular hole, regardless how small - but finite - it may be, varies as the inverse square of the distance from the flaw radius. If, however, there is no hole in the plate in the first place, the stress is bounded by a constant. Hence, there is a jump in singularity with geometry. Appendix 4.3, also by Atkinson, summarizes some

recent work on non-local elastic media and its application to the line crack problem. He concludes that recent claims that such theories lead to a finite stress at a crack tip are unjustified.

Atkinson, Smelser and Sanchez (Appendix 4.4) have combined to report continuing work utilizing the cracked, diametrically loaded Brazil disk to deduce the Mode II fracture toughness. This shear mode, which is difficult to generate experimentally, is characteristic of a pure shear failure as might occur in a spinning disk or turbine rotor. One of the virtues of this Brazil test is the possibility of assessing mixed mode fracture toughness, perhaps in a better way than using angled cracks in a plane stress tensile specimen.

In a manuscript being prepared for journal publication, the Avila and Betz work on the adhesive debonding of circular rods from the matrix will be reported. This class of free-surface debond geometries, as well as encapsulated (fiber) rods are important in composite materials. The primary characteristic controlling the debonding is believed to be the specific adhesive fracture energy along the interface. One way of measuring this interfacial energy to engineering accuracy is to use a variation of the blister test. Somayaji (Appendix 4.5) has assembled the requisite experimental assembly for a plexi-glass-steel combination using a point loading for these relatively stiff materials. A pressure loading is also contemplated for possible use with a glass-polymer or glass-epoxy bimaterial combination. Such an independent measurement of the adhesive energy permits one to then use its (now known) value in analytical work using the same bimaterial combination, e.g. fiberglass reinforced epoxy resins. Our experiments would hopefully use the "standard materials" being developed by Kelley at the University of Akron. To prepare for such analytical work a literature survey of various contributions to the behavior, including fracture, of composite materials has been assembled for later use (Appendix 4.6).

Fracture criteria for various materials, preferably in some universal form, is being investigated analytically and experimentally (see University of Akron sub-contract). In principle, the idea may be understood by considering the usual Griffith fracture criterion expressed in the form $\sigma^2 a = \kappa E \gamma$, in which κ is a numerical constant depending upon geometry, E is the modulus and γ the fracture energy. If it is written in the form $\sigma^2 / (2E) = (\kappa/2) (\gamma/a)$, and the (uniaxial) strain energy density, W , is recognized as $W = \sigma^2 / (2E)$ which at failure, say W_f , is the area under the brittle stress-strain curve to failure, then one has $\gamma = \kappa' a W_f$, with κ' a numerical constant and "a" the crack size. One might then jump to a hypothesis that in any material, the fracture energy for a given geometry and crack size (obtained say from NDE) may be deduced from the area under the uniaxial tensile stress-strain curve to failure. Kelley at the University of Akron has used essentially this result, as proposed by Andrews for linear viscoelastic polymers. The strength of materials approach recognized this principle many years ago in denoting the area under any material's stress-strain curve to failure as "toughness". It is hoped that the results of the numerical analysis being conducted by Becker (Appendix 5.2) can be used in checking a general fracture criterion through a knowledge of the actual large strain at a crack tip.

Another comparative fracture analysis has been pursued by Batdorf (Appendix 4.7) during his one month visit with us. His contribution is a position paper dealing with the micro-mechanics of failure as applied to mixed media, in particular to fibrous composites. The eventual aim, which may not be achieved during the next year, is to see if there is any common ground or criteria for which both the energy balance (Griffith) criterion and statistical (Weibull) criterion, applicable principally to ceramics, can be combined or compared.

2.2 Structure - Property Relationships

The relation between the chemical structure of a material and its mechanical behavior is perhaps the most fundamental problem of all. It affects not only the constitutive law, but controls processing characteristics and the failure mode.

We contemplated the development of an Interaction Matrix which relates parameters describing the material structure (Burger's vector, cross-link density, Weibull modulus, etc.) with those describing its mechanical properties. In the subcontract arrangement with Dr. F.N. Kelley and Dr. P. Dreyfuss, University of Akron, the intent is to synthesize a "standard elastomer" and a "standard epoxy" having controlled and known chemical compositions. The current status of the work is given in Appendix 5.1. During this first year the principal effort has been concentrated upon designing the experimental setups and obtaining reproducible synthesized material from systems which are chemically clean and as environmentally insensitive as practicable. (Subsequent doping for environmental effects was originally contemplated, but this effort will not now be conducted on this program.) Two systems were proposed: the polymeric because there is already linearly viscoelastic analysis capability in the community which can therefore be used to relate theory and experiment, and the epoxy resin because as a usually non-linear material the analysis capability is very limited and definitive material property data is needed to guide the theoretical assumptions. So, in both cases material characterization is needed - in the first to verify the analysis techniques, and in the second to guide the stress-strain assumptions incorporated into possible analyses. As the University of Akron, (Appendix 5.1) reinforced by internal support from Plazek (Appendix 4.8), preliminary mechanical and thermal characterization of rubbery and glassy network polymers has been completed with an emphasis on fracture and tear energies as a function of temperature reduced strain rate. Current chemical structure variables

are controlled cross-link density and chain back-bone flexibility. In the model epoxy system, a method has been found to describe local homogeneities by placing accurately known spherical particles in the polymer matrix.

One of the important factors affecting the mechanical properties of a material is the effect of the fabrication process and precursor material variability. Dr. J.T. Lindt has completed a preliminary investigation of "melt fracture" (Appendix 4.9). This work will not be continued, however, due to funding limitations.

Two other topics complete our present activities in structure-property relationships. The first, by Dr. H. Kuhn (Appendix 4.10) is related somewhat to Dr. J.T. Lindt's polymer processing experiment. Dr. Kuhn is investigating the strain threshold at fracture during forming, especially in compression, such as during a forging operation. He has also made micro-analyses of a cobalt-nickel alloy, known as MP 35, and found that void nucleation is the mechanism which controls the first stage of the fracture process. It occurs by grain boundary sliding induced by dynamic recrystallization. Finally, the only laboratory work dealing with ceramics has been conducted by Porter (Appendix 4.11). The work he has completed to date has concentrated upon obtaining consistent powders and evaluating the reproducibility of simple shaped fabricated specimens. The only processing variable considered so far is surface contamination of silicon carbide powder particles. Low temperature plasma heating during the sintering was shown to produce apparently clean, active surfaces in the powder compacts. Continuing tests will probably be directed toward varying the initial green densities of the powder.

3.0 Statement of Work

The following research is to be conducted:

- a) Investigate a class of idealized problems which are analytically tractable but key to the understanding of fracture mechanisms and their control. This class of problems will include, but not be limited to, the following:
 1. Study the three dimensional stress singularities along a crack surface and its interface with free surfaces or other material interfaces, as well as the engineering importance of these singularities. Investigate the nature of this stress singularity in terms of typical crack geometric parameters and the nature of the mathematical discontinuity as these parameters approach zero.
 2. Investigate the fracture behavior of an elastic fiber in a matrix material considering typical interfacial defects and uniaxial and combined stress states on the fiber. Investigate the adhesive and cohesive strength mechanisms of the fiber matrix interface.
 3. Investigate the extension of models of fracture mechanisms of the micro/macro scale in order to predict fatigue crack growth, including as appropriate, strain rate effects, temperature, environmental conditions, and nonlinear behavior.
 4. For the classes of problems to be addressed under "a" - metals, polymers and ceramics, individually and in combination, will be considered in the development of fracture criteria in which particular significance can be attributed to constitutive equations, thermodynamics, kinetics or material processing.
- b) Investigate the structure-property characteristics of metals, poly-

mers and ceramics with respect to both adhesive and cohesive fracture behavior.

1. Review the existing literature and develop an interaction matrix between the chemical and crystalline or noncrystalline structure of a material and its mechanical properties.
 2. Investigate, both theoretically and experimentally, the quantitative nature of this interaction and its significance to fracture.
 3. Coordinate with AFOSR the planned investigation to develop the quantitative relationship of the interaction matrices.
- c) Review the current state-of-the-art in numerical analysis methods which are applicable to the science of fracture, considering, in particular, the micro/macro modeling levels, kinetic phenomena, and thermodynamic considerations.
- d) Investigate the state-of-the-art in the field of instrumentation and measurement science which has application to the science of fracture and structure/property relationships. In particular, include investigation of techniques which may be developed to study in a nondestructive manner internal material, i.e., nonsurface, behavior.
- e) Develop an active program to transfer fracture research results to the user community and to maintain an assessment of critical fracture technology requirements on a national level.

Although some work was continued during the second year in the last three areas, i.e. numerical analysis, instrumentation science and technology transfer, it was at a considerably reduced level in view of the changed emphasis in the overall program.

4.0 APPENDICES
TASK REPORTS

Appendix 4.1

The 3 - D Stress Singularity Problem

A Position Paper

Dr. Colin Atkinson
Imperial College, London
Visiting Professor, University of Pittsburgh

Science of Fracture Research Project
AFOSR Contract #F49620-78-C-0101

School of Engineering
University of Pittsburgh
Pittsburgh, PA 15261

PRECEDING PAGE BLANK-NOT FILLED

1. Introduction

The way in which the stress field varies at notches and angular corners in plates is obviously of importance to failure analysis. In particular the square root stress singularity at the tip of a line crack in plane stress/plane strain plays a central role in fracture mechanics. An enormous amount of work has been done in this subject, much of the recent work being reviewed in (1).

As a representative of early work note the work of Knein (2,3) who considered an elastic wedge of angle $\pi/2$ in plane strain, one side having zero tractions, the other having zero displacement. Assuming displacement components of the form

$$u_i = r^\lambda f_i(\lambda, \theta), \quad i = 1, 2 \quad (1.1)$$

with (r, θ) polar coordinates, then the eigenvalues λ are solutions of the equation

$$\{\sin(\pi\lambda/2)\}^2 = \{4(1 - \nu)^2 - \lambda^2\}/(3 - 4\nu) \quad (1.2)$$

Later Williams (4,5) considered various boundary conditions in angular corners for plates under bending or extension. For a wedge of angle α in plane strain with traction free sides he looked for separable solutions of type (1.1) and deduced an eigenvalue equation for λ , i.e.,

$$\{\sin(\lambda\alpha)\}^2 - \lambda^2(\sin \alpha)^2 = 0 \quad (1.3)$$

Many other results of this type have been found, some of which are referred to in (1).

The method used in (3) and (4) is to assume a solution separable in polar coordinates and then to deduce the eigenvalue equation for λ such that zero boundary conditions are satisfied on the infinite wedge sides.

The usefulness of such expressions is that close to the corner the terms with λ small should dominate, the associated stress field often being singular (i.e., leading to infinite stresses as $r \rightarrow 0$). Furthermore the smallest λ allowed by considerations of finite energy may be complex. This happens, for example, in the case of a crack at an interface between two dissimilar elastic media ((6), see also (1)).

For plane elastic systems the above-mentioned results are relatively simple to deduce, although some care is still required. For example it may not be sufficient to assume a solution of the form $u = r^\lambda f(\theta)$, the r dependence may involve $\log r$ terms. To illustrate this we give in Appendix A a solution to a plane potential problem (anti-plane elasticity) where this is easily seen. The approach we use in Appendix A is to employ the Mellin transform and in this way the eigenvalue results appear quite naturally as the poles of the resulting transform. Furthermore, arguments based on the Mellin transform are potentially useful in discussing the question of completeness of the eigenfunctions for the wedge. It is worth enlarging on the completeness question here since the reader will see it being mentioned in the context of the '3-d singularity' discussed later. Given the set of eigenfunctions (1.1) and their associated eigenvalues, λ , a natural question to ask is whether they are complete in the sense that they can represent fairly general boundary data on the arc $r = 1$ say. It is not sufficient to show that infinite sums of such eigenfunctions converge on $r = 1$, it is also necessary to show that they converge to the data. Considerations of this type have been made most recently by Gregory (7) for plane elastic problems. In particular he shows that William's eigenfunctions for $\nabla^4 \phi = 0$ in the wedge are complete in the sense that they may be used to expand the data

$$\left. \frac{\partial}{\partial r} \left(\frac{1}{r} \phi \right) \right|_{r=1} = f(\theta) \quad (1.4)$$

$$\left. \frac{\partial^2 \phi}{\partial \theta^2} \right|_{r=1} = g(\theta)$$

where $f(\theta)$, $g(\theta)$ are 'arbitrary' independent functions prescribed on $(-\alpha_1, \alpha_1)$, if $2\alpha_1$ is the wedge angle (α of (1.3) corresponds to $2\alpha_1$ here). See (7) and (8) for more details of these results. Thus stress singularities in the two dimensional elastic situation are reasonably well understood. However it should be noted that the nature of the singularity (i.e., the exponent λ) and its angular variation $\{f(\lambda, \theta)\}$ although essential are only the first step for a realistic stress analysis. The coefficient of the eigenfunction which will result from the influence of the applied load is equally important, and the determination of this coefficient (e.g., the stress intensity factor when $\alpha = 2\pi$, $\alpha_1 = \pi$) may involve extensive numerical analysis.

The situation regarding three dimensional stress-singularities where cracks intersect free surfaces, etc., is much more difficult to analyze and the nature of the singularity has 'perhaps' only recently been illuminated. We use the adverb 'perhaps' because there is not yet total agreement on the results and also because naturally there is not yet complete mathematical rigor associated with the calculations. Nevertheless a plausible and fairly comprehensive investigation of the singularity at the quarter-infinite crack in a half-space has been made by Benthem (9), (10), and (11). His work has the additional virtue that he has repeated his earlier calculations by a different method in his later paper. Furthermore, there is some measure of agreement between Benthem's results and results obtained by

Bazant and Estenssoro (12) who used a finite element method of determining critical eigenvalues. Each of the above-mentioned authors (9-12) use spherical polar coordinates (r, θ, ϕ) with origin 0 at the terminal point at which the crack front edge meets the free surface (see Fig. 1). They then assume the solution to be separable in the form $r^\lambda F(\lambda, \theta, \phi)$ and look for the eigenvalues λ and associated eigenfunctions F . The methods used for doing this will be discussed later.

Before discussing the results of the above work in more detail it is appropriate to indicate other work which has appeared in the literature. In (12) these other works are referred to by the sentence: - "Other analytical solutions for orthogonal cracks (13,14) have also been presented, but they disagree with the results of Benthem (10) as well as the present paper". We have changed the reference number to agree with the numbering used here. In (11), Benthem referring to his papers (9) and (10) states "The need was felt to confirm these results independently by quite another method. In some private correspondences and concept-papers kindly sent to the author the results of (9,10) were questioned". He does not refer to any of the opposing work specifically. Note, however, that Benthem and Koiter (15) discuss the paper by Folias (14) and in his reply Folias raises questions concerning Benthem's report (9). One of these questions, as to whether the problem admits a solution in separable form, particularly in θ and ϕ , is avoided by the approach used in Benthem's later paper (11).

No reference at all to (13) and (14) is made by Benthem in (10) and (11) and only the sentence quoted above made by Bazant and Estenssoro (12). This is unfortunate since constructive criticism would have been useful in forming a balanced view (such criticism may have occurred, of course, in references we have overlooked). There is available however a reported

discussion by Kawai and Folias which is useful insofar as it gives another view of the problem and highlights possible criticisms of the other work. The report of this discussion which was prepared by Dr. R.E. Smelser is included as Appendix 2. It is clear from this discussion that these authors are not entirely satisfied with the approach of (9) and (10) but are not really ready to offer a viable alternative.

In this paper we shall adopt the position that the results of Benthem (11) are the best available at the moment, while leaving our options open just in case more exotic behavior at the corner point is discovered in the future. Even if the singularity at the corner point were more exotic, involving $\log r$ terms say, the exponents calculated by Benthem would still probably be a good approximation since $\log r$ tends to infinity very slowly as r tends to zero making $r^\lambda \log r$ and r^λ hardly discernible as $r \rightarrow 0$.

2. Benthem's Results for the Quarter-Infinite Crack in a Half-Space (Fig. 1)

The crack geometry is shown in Figure 1. Cartesian coordinates (x, y, z) and spherical coordinates (r, θ, ϕ) are used where

$$\begin{aligned}x &= r \sin \theta \cos \phi \\y &= r \sin \theta \sin \phi \\z &= r \cos \theta\end{aligned}\tag{2.1}$$

The half-space is the region $z > 0$ (free-surface $z = 0$) and the crack occupies the quarter-plane $y = 0, x > 0, z > 0$. Thus the region to be investigated is a conical region (with vertex at $r = 0$) between the three planes $\theta = \pi/2$, $\phi = +0$ and $\phi = 2\pi - 0$. These planes are taken to be stress free. In this conical region Benthem considers a state of stress which in terms of the cartesian stress-components is written

$$\sigma_{xx} = r^\lambda f_{xx}(\lambda, \theta, \phi), \quad \sigma_{xy} = r^\lambda f_{xy}(\lambda, \theta, \phi) \text{ etc.}\tag{2.2}$$

If these stress components are required to leave the half-space surface and the crack surfaces stress free, then this will only be possible for an infinite enumerable set of values of λ . These λ are the eigenvalues and the corresponding functions f_{ij} the eigenfunctions, the numerical determination of which is the aim of Benthem's papers (9-11). Assuming for the moment that the numerical method is capable of determining the λ 's, etc., with sufficient accuracy, there still remains the possibility of other kinds of functions of r in addition to r^λ which might appear in a complete set. Consider the illustration the simple example of Appendix 1, where $r \log r$ terms appear. In a paper on conical regions in elasticity theory (16), Benthem discusses a theorem which says that if λ_1 is an eigenvalue so is $-1 - \lambda_1$ and in the course of that work he is aware that occasionally terms like $r^{\lambda_1} \ln r$ appear instead

of r^{λ_1} , his definition of λ_1 is in terms of displacements, i.e., $u \sim r^{\lambda_1} f(\lambda_1, \theta, \phi)$. If such did occur in the problem under discussion then the assumption (2.2) would miss them. Also it is clear from the work of Kondratev (17) that rigorous analysis of such problems can be very involved.

Possible values of λ are constrained by the condition that the strain energy be finite, this means that in a neighborhood of the vertex, only eigenfunctions with

$$\operatorname{Re} \lambda > -3/2 \quad (2.3)$$

are allowed. Hence within the framework of linear elasticity, displacements $u \sim r^\gamma$, $\operatorname{Re} \gamma > -1/2$ which become infinite at the vertex are not ruled out by such a finite energy condition. In the results of Folias (14) such infinite displacements were reported, i.e., he reported $u \sim r^{1/2-2\nu}$ which becomes infinite as $r \rightarrow 0$ if $\nu > 1/4$. Such a result is disturbing to physical intuition and was criticized for this reason by Benthem and Koiter in (15) (see also Appendix 2).

To find the smallest possible eigenvalue λ subject to the constraint (2.3) the equations of elasticity theory are applied to the demi-spherical surface $r = 1$, there is no loss of generality in doing this since along a given radius all stresses are assumed proportional to r^λ and all displacements to $r^{\lambda+1}$. On the surface $r = 1$ the range of the two remaining spherical coordinates is

$$0 < \theta \leq \pi/2, \quad 0 \leq \phi \leq 2\pi \quad (2.4)$$

The eigenvalue problem is to find λ , $f_{xx}(\lambda, \theta, \phi)$, etc., as solutions of the equations of elasticity such that traction free boundary conditions hold on the crack surfaces at $r = 1$, i.e., $\phi = 0$, and 2π , $0 < \theta \leq \pi/2$ and on the free surface $\theta = \pi/2$, $0 \leq \phi \leq 2\pi$. In (9) and (10) Benthem applies a method based on separation of variables (θ, ϕ) . In (11) he uses finite differences

and in (12) and (18) Bazant and Estenssoro use a finite element method.

In (11) Benthem defines a new variable

$$\zeta = \theta^{1/2} \quad \text{so} \quad 0 < \zeta \leq (\pi/2)^{1/2} \quad (2.5)$$

and divides the ζ , ϕ range into $M \times N$ equal meshes $\Delta\zeta$, $\Delta\phi$.

Tables 1, 2 and Fig. 2 are abstracted from his paper (with our numbered reference notation). Symmetrical (Table 1) and antisymmetrical (Table 2) states of stress refer to symmetry (antisymmetry) about the plane $\phi = \pi$.

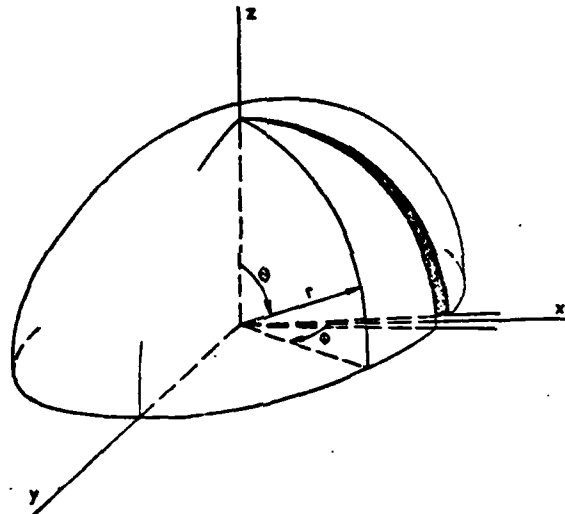


Fig. 1. The half-space $z > 0$ with the quarter-infinite crack $y = 0, x > 0, z = 0$. Cartesian coordinates x, y, z . Spherical coordinates r, θ, ϕ .

Table 1. Eigenvalues λ for symmetrical states of stress ($\sigma \sim r^{\lambda}$)

Poisson's ratio	Obtained with $M \times N$			Benthem Refs. (7,10)	Bazant [†] Refs. (12,18)	Exact values
	10 x 30	14 x 42	16 x 48			
-1	-0.146			-0.155		
-0.965	-0.223			-0.241		
-0.75	-0.4404			-0.4516		
-0.5	-0.4998	-0.5007	-0.50084	-0.50089		
0	-0.49997			-0.5		-0.5
0.15	-0.4835			-0.4836	-0.484	
0.3	-0.4519	-0.4519		-0.4523	-0.452	
0.4	-0.4141	-0.4129		-0.4132	-0.413	
0.5	-0.3452	-0.3381	-0.3367	-0.3318		
0.5				0		0
0.3	0.217			0.218		
0	0.430			0.410		
0				0.5		0.5
0.3	0.664			0.681		
0.5				1		1

[†]Bazant and Estenssoro do not actually give values, but state that their extrapolation to an infinite number of meshes gives values within 0.4% from those of previous column ($0 \leq \nu \leq 0.4$).

Table 2. Eigenvalues λ for antimetrical states of stress ($\sigma \sim r^1$)

Poisson's ratio	Obtained with $M \times N$ 10 x 30	Obtained with $M \times N$ 14 x 42	Bazant† Ref. (12)	Exact values
0	-0.4997	-0.4999		-0.5
0.15	-0.5668	-0.5668	-0.565	
0.3	-0.6076	-0.6073	-0.598	
0.4	-0.6291	-0.6286	-0.604	
0.5	-0.6462	-0.6462		
0	-0.271			
0.15	-0.157			
0.3	-0.057			
0.4	-0.030			
0.5				0
0.3	0.492			0.5
0	0.492			0.5
-1	0.482			0.5

†In (2) erroneously is stated that these eigenvalues are double.

The results shown in Tables 1 and 2 demonstrate a measure of agreement with those of Bazant and Estenssoro. Of course, both sets of authors use the same basic assumption (2.2), the subsequent methods used are however quite different. The agreement shown in the tables lends support to the accuracy of the results.

J. P. BENTON

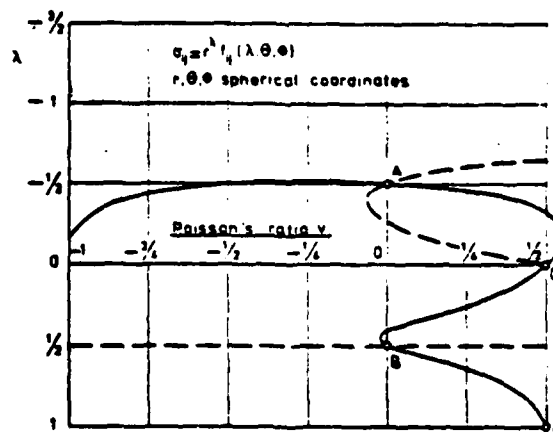


Fig. 2. Three-dimensional stress singularities of the quarter-infinite crack in the half-space. Solid line, λ -values belonging to symmetrical states of stress (Table 1). Broken line, λ -values belonging to antimetrical states of stress (Table 2). A, B, C, D, exact points.

Concluding Remarks

We have fixed attention on the Quarter-infinite crack shown in Fig. 1, since this is perhaps the simplest configuration in which the three dimensional nature of the singularity when a crack meets a free surface is present. It is expected, of course, that the nature of the singularity will be precisely the same for a finite plate provided the through crack is at a right angle to the plate surface. If the assumption (2.2) is correct then finding the lowest eigenvalue becomes a problem of doing accurate numerical analysis. There is still a measure of disagreement however, c.f., the paper by Fujitani (19) as well as the previously cited papers (13),(14). We have chosen the results presented in section 2 for the reasons given there, however the reader is again reminded of Appendix 2 for the other side of the discussion. As well as the eigenvalue λ for which tables of results are presented here there are graphical presentations of the eigenfunction given in (11) and much more detail than we have presented here. Furthermore, Bazant and Estenssoro (12) have applied their numerical method to the problem of a through crack which meets the surface obliquely to find the eigenvalues there. In this case there can be complex eigenvalues.

In conclusion, there now exist numerical results for the eigenvalue λ in assumed stress distributions of the form $\sigma \sim r^\lambda$ (r spherical radius) for the three dimensional singularity of a through crack at a free surface. Furthermore, there is some measure of numerical agreement between two sets of authors, i.e., (11) and (12). The associated eigenfunctions with this dominant singularity $\text{Re } \lambda > -3/2$ have been obtained numerically and presented graphically in (11) for example. Note that other related three

dimensional singularities have also been considered, e.g., cracks and inclusions of a wedge-plan form see (1) and (12) for references to some of these papers. Finally in references (20)-(27) we cite less sophisticated attempts at modelling three dimensional cracks.

References

- (1) Atkinson, C., Stress singularities and fracture mechanics, Appl. Mechs. Reviews, (1979) 123.
- (2) Knein, M., Zur Theorie des Druckversuchs, Z.A.M.M. 6, 414 (1926).
- (3) Knein, M., Der Spannungszustand bei ebener Formänderung und vollhommenen veränderter Querdehnung, Abh. Aero. Inst. Techn. Hochschule, Aachen 7, 43 (1927).
- (4) Williams, M.L., Surface stress singularities resulting from various boundary conditions in angular corners of plates under bending, Proc. 1st U.S. Nat. Congr. Appl. Mech. 325 (1951).
- (5) Williams, M.L., Surface stress singularities from various boundary conditions of plates in extension, J. Appl. Mech. 19, 526 (1952).
- (6) Williams, M.L., The stresses around a fault or crack in dissimilar media, Bull. Seismological Soc. Am. 49, 199 (1959).
- (7) Gregory, R.D., The semi-infinite strip $x \geq 0$, $-1 \leq y \leq 1$; completeness of the Papkovitch-Fadle eigenfunctions when $\phi_{xx}(0,y)$, $\phi_{yy}(0,y)$ are prescribed, J. of Elasticity, 10, 57 (1980).
- (8) Gregory, R.D., Green's functions, bi-linear forms, and completeness of the eigenfunctions for the elastostatic strip and wedge, J. of Elasticity 9, 283 (1979).
- (9) Benthem, J.P., Three dimensional state of stress at the vertex of a quarter-infinite crack in a half-space, Report WTHD No. 74, Dept. of Mechanical Engineering, Delf Univ. of Technology (Sept. 1975).
- (10) Benthem, J.P., State of stress at the vertex of a quarter-infinite crack in a half-space, Int. J. Solids. Structures 13, 479 (1977).
- (11) Benthem, J.P. The quarter-infinite crack in a half-space, Int. J. Solids. Structures, 16, 119 (1980).
- (12) Bazant, Z.P. and Estenssoro, L.F., Surface singularity and crack propagation, Int. J. Solids Structures 15, 405 (1979).
- (13) Kawai, T., Fujitani, Y. and Kumagai, K., Analysis of singularity at the root of the surface crack problem, Proc. Int. Conf. Fracture Mech. and Tech., Hong Kong, March 1977 (Ed. G.C. Sih and C.L. Chow) Vol. II, pp. 1157-
- (14) Folias, E.S., On the three dimensional theory of cracked plates, Trans. A.S.M.E. (Ser. E) J. Appl. Mech. 42, 663- (1975).
- (15) Benthem, J.P. and Koiter, W.T., Discussion of (14), J. Appl. Mech, 43, 374 (1976). This includes Author's Closure by Folias.

- (16) Benthem, J.P., On an inversion theorem for conical regions in elasticity theory, *J. of Elasticity*, 9, 159 (1979).
- (17) Kondratev, V.A., Boundary problems for elliptic equations in domains with conical or angular points, *Trans. Moscow. Math. Soc.* 16, 209 (1967) (*Trans. Am. Math. Soc.*).
- (18) Bazant, Z.P. and Estenssoro, L.F., General numerical method for three dimensional singularities in cracked or notched elastic solids. In *Proc. 4th Intl. Conf. on Fracture, Unif. of Waterloo, Canada*, (D.M.R. Taplin, Editor) Vol. 3a, 371 (1977) (Pergamon Press, Oxford).
- (19) Fujitani, Y., Finite element analysis of the singular solution in crack problems, *Proc. 1st Intl. Conf., Num. Methods in Fracture Mechanics*, (Ed. A.R. Luxmoore and D.R.J. Owen) 398 (1978).
- (20) Tracey, D.M., Finite elements for three-dimensional elastic crack analysis, *Nuclear Engineering & Design*, 26, 1974, 282-290.
- (21) Barsoum, R.S., A degenerate solid element for linear fracture analysis of plate bending and general shells, *Int. J. for Num. Meth. Eng'g*, 10, 1976, 551-564.
- (22) Atluri, S.N. & Kathiresan, K., An assumed displacement hybrid finite element model for three-dimensional linear fracture mechanics, *Proc. 12th Annual Meeting of the Society of Engineering Science, Univ. of Texas, Austin, 1975*, 77-87.
- (23) Pian, T.H.H., & Moriya, K., Three dimensional crack element by assumed stress hybrid model, *Proc. 14th Annual Meeting of the Society of Engineering Science, Lehigh, 1977*, 913-917.
- (24) Blackburn, W.S. & Hellen, T.K., Calculation of stress intensity factors in three dimensions by finite element method, *Int. J. for Num. Meth. Eng'g*, 11, 1977, 211-230.
- (25) Hall, C.A., Raymund, M., & Palusamy, S., A macro element approach to computing stress intensity factors for three dimensional structures, *Int. J.F.*, 15, 1979.
- (26) Hilton, et al., Specialized finite element procedures for three dimensional crack problems, *Numerical Methods in Fracture Mechanics*, 1978, 411-421.
- (27) Yamamoto, Y., & Sumi, Y., Stress intensity factors for three dimensional cracks, *Int. J. F.*, 14, 1978, 17-38.

Appendix 1

Consider Laplace's equation in plane polar coordinates,

$$r \frac{\partial}{\partial r} \left(r \frac{\partial \phi}{\partial r} \right) + \frac{\partial^2 \phi}{\partial \theta^2} = 0 \quad (\text{A.1})$$

in the region $0 \leq \theta \leq 3\pi/2$, $0 < r < \infty$ of the (r, θ) plane subject to the boundary conditions

$$\phi = 0 \quad \text{on} \quad \theta = 0 \quad \text{for all } r$$

$$\frac{\partial \phi}{\partial \theta} = r \quad \text{for} \quad 0 < r < 1$$

$$\text{on } \theta = 3\pi/2 \quad (\text{A.2})$$

$$= 0 \quad \text{for} \quad r > 1$$

and $\phi \rightarrow 0$ as $r \rightarrow \infty$.

Multiplying (A.1) by r^{s-1} and integrating over r from 0 to ∞ gives the equation

$$\frac{d^2 \bar{\phi}}{d\theta^2} + s^2 \bar{\phi} = 0 \quad (\text{A.3})$$

for the Mellin transform of ϕ , $\bar{\phi} = \int_0^\infty \phi r^{s-1} dr$. Solving (A.3) subject to the transform of the boundary conditions (A.2) and using the inversion theorem of the Mellin transform leads to the result

$$\phi = \frac{1}{2\pi i} \int_{\gamma-i\infty}^{\gamma+i\infty} \frac{\sin s \theta \cdot r^{-s}}{s(s+1) \cos(\frac{3\pi s}{2})} ds \quad (\text{A.4})$$

The condition that ϕ be finite at the origin $r = 0$ together with $\phi \rightarrow 0$ as $r \rightarrow \infty$ designates the strip of regularity of $\bar{\phi}(s)$ so that

$$-1/3 < \gamma < 1/3 \quad (\text{A.5})$$

The solution near $r = 0$ can be deduced from (A.4) by closing the contour in the left half-plane and evaluating the residues. These poles are simple with the exception of a double pole at $s = -1$. The final result for $r < 1$, is

$$\phi = \sum_{\substack{N=0 \\ N \neq 1}}^{\infty} \frac{3(-1)^{N+1} (2N+1)/3 \operatorname{Sin}\left\{\left(\frac{2N+1}{3}\right)\theta\right\}}{\pi(2N+1)(N-1)} \quad (\text{A.6})$$

$$+ \frac{2r}{3\pi} (\theta \operatorname{Cos} \theta + \log r \cdot \operatorname{Sin} \theta - \operatorname{Sin} \theta)$$

That the last expression is a solution of $\nabla^2 \phi = 0$ can be easily checked.

The interesting feature from the present point of view is the presence of the $\log r$ term which may not have been suspected a priori.

Appendix 2

Summary of Discussion of T. Kawai
and E.S. Folias, Austin, Texas
March 29, 1979

The discussion centered on two points. The first was the discrepancy between J.P. Benthem's and Kawai's solution and the second was an inquiry into whether the 3-D problem possessed a separable solution in a form similar to Williams 2-D eigenfunction expansion. Benthem and Kawai both chose similar starting points for their attempts to solve the 3-D crack problem. They both assumed the solution to be separable in the form $r^\lambda F(\lambda, \theta, \phi)$ where r, θ, ϕ are spherical coordinates and λ is an eigenvalue. While Benthem constructed a solution which satisfied the stress free boundary conditions on the crack flanks and then satisfied the stress free surface conditions, Kawai began by satisfying the stress free surface conditions and then satisfying the conditions that the crack flanks be stress free. Kawai felt it was easiest to find functions which were zero on the plate surface. The approach of Kawai produced eigenfunctions which Benthem did not find. Kawai noted that he had a student do additional work on the problem but was unable to resolve this discrepancy and had not published this work.

Folias pointed out that Benthem's 1972 paper contained an incomplete set of functions which Benthem had added to in 1976. However, the question of completeness of Benthem's solution has not been resolved. Folias had at an earlier meeting in San Francisco suggested that Kawai show Benthem's solution was incomplete. By showing one of the eigenfunctions which Benthem's method had not produced satisfied both the differential equation and boundary conditions, Kawai would be able to demonstrate that the solution of Benthem was still incomplete. Kawai has not attempted this and seemed reluctant to pursue

the point. The reason for this reluctance was two-fold; (i) lack of a capable graduate student to follow up the initial work, and (ii) the adverse reaction of the fracture community to ideas challenging Benthem's hypothesis. It was also noted that the singularity which Folias had found was reproduced by Kawai's technique. The result was found to be caused by a singular condition of the matrix in the eigenvalue determination. This indicates that the functions $f_{ij}(\theta, \phi)$ of Folias are most probably zero on the surface. Folias and Kawai agreed that Benthem's method was not systematic and Folias concluded that on the basis of Kawai's adopting a more systematic approach to the solution his results were more likely to be complete.

Further, work of J. Newman also furnishes indirect evidence that the work of Folias and Kawai is correct. Newman found that near the surface of a plate the stress intensity factor rises slightly as a function of the plate thickness for a crack length to thickness ratio much less than one. This is in agreement with the work of Folias and Kawai. Kawai also had found that the first eigenvalue changes as the plate thickness increases. Elasto-plastic finite element work of Kawai (presented at Swansea in January) on the cracked plate also indicated that the yielding begins on the plate surface and spreads into the interior. From this he inferred that the strength of the singularity changes near the surface. A final problem was proposed by Kawai as an alternative method for determining the strength of the singularity. The problem is equivalent to the Inglis solution of an elliptic hole. The solution would be sought for the elliptic hole in a plate and the minor axis would be allowed to approach zero. In this way some insight may be gained concerning the 3-D crack singularity.

The problem of separability of the solution was discussed. Kawai pointed to the fact that the problem of the conical cavity in a half space was separable and by inference the crack solution should be also. Folias had some reservations and pointed out that the eigenvalue's slow rate of convergence in the numerical solution technique is possible evidence that the solution may not be separable. This Kawai admitted may indeed be true and thought that while the solution for the stress analysis may be separable, separability may not apply to the solution of the singularity. Folias pointed out that spherical coordinates were not the natural coordinates for the problem, and while the solution may not be separable in spherical coordinates, it may be in some other system. Folias noted that it may be possible to obtain the dominant singularity by a separation technique. Kawai agreed that expansions in Legendre polynomials may not be appropriate but another special function such as Bessel functions or a generalized function may work. Agreement was reached that the final solution may not be obtainable through a generalization of the Williams solution techniques. Thus to date the dominate singularity is not known for the 3-D problem and may not be obtainable through standard techniques.

Appendix 4.2

A Note on Stress Concentrations
and Energy Release Rates

Dr. Colin Atkinson
Imperial College, London
Visiting Professor, University of Pittsburgh

Science of Fracture Research Project
AFOSR Contract #F49620-78-C-0101

School of Engineering
University of Pittsburgh
Pittsburgh, PA 15261

1. Introduction

There are many situations where pre-existing stress concentrators exist in a solid, either because of particular design requirements or because of defects which occur during fabrication or subsequent handling. One particular kind of defect is, of course, a crack and much attention has been given to this, leading to the well developed subject of fracture mechanics. For a recent review of stress-concentrations and fracture mechanics see (1). Our concern here is not with the crack defect per se but rather with its relation and/or comparison with other stress concentrations such as corners or holes. However, since the concept of 'energy release rate' is useful in discussing crack extension it is perhaps natural to ask whether an energy balance approach can in some analogous way quantify the effect of other stress singularities and 'perhaps' explain the transition from a corner (without a crack starter) to a crack-like singularity. We use the adverb perhaps here, because it is natural when using energy arguments to discuss the change in energy with a change in configuration of the defect, and it may be that configuration changes other than crack initiation are energetically favorable. A useful tool for such energy calculations is the elastic energy momentum tensor which has been used for expressing the force on a dislocation or point defect (Eshelby (2) and (3)) and for calculating the energy flow into a moving crack tip (Atkinson and Eshelby (4)). We shall give a brief account of this in Section 2 which is based to some extent on a paper by Eshelby (5). In Section 3 we discuss the implications of the formulae derived in Section 2 when applied to cracks or blisters forming on corners or holes. Our conclusion will be that the initiation of a small crack from a hole will lead to an energy release rate or crack extension force which usually tends to zero as

the crack length tends to zero. On the other hand, there will usually be a finite effective normal force (per unit surface area) on a hole boundary (c.f. equation (2.12)). However, although this finite force can be used to give a finite energy release rate in erecting a blister (c.f. for example (2.10)) this must be balanced by the energy required to produce a blister. This required energy may be large since removal of material is required for blister formation.

2. Energy Change Calculations and The Energy Momentum Tensor

For completeness, we give here results (abstracted from (5)) which apply to finite deformation with a general stress-strain relation, though our subsequent applications will be to infinitesimal elasticity. We use rectangular coordinates X_i to label particles in the reference configuration (initial unstrained state). The cartesian coordinates x_i (in the same coordinate system) refer to the current configuration to which the particle X_i is moved on deformation by a vector displacement u_i such that

$$u_i(X_m) = x_i(X_m) - X_i \quad (2.1)$$

The nominal (Piola-Kirchoff or Boussinesq) stress p_{ij} is defined so that $p_{ij} dS$ is the component parallel to the X_i axis of the force on an element of area which, before deformation, was an element of area dS perpendicular to the X_j axis. Thus if W is the strain energy in unit initial volume then

$$p_{ij} = \frac{\partial W(u_{m,n})}{\partial u_{i,j}} \quad (2.2)$$

where $u_{i,j} = \partial u_i / \partial X_j$;

In the absence of body forces the equations of equilibrium are

$$\frac{\partial p_{ij}}{\partial X_j} = 0 \quad (2.3)$$

Note that for finite deformation the p_{ij} are not symmetric.

In terms of the energy density W , the energy momentum tensor is defined as

$$P_{lj} = W \delta_{lj} - p_{ij} u_{i,l} \quad (2.4)$$

δ_{lj} being the dirac delta function. It can be shown by direct calculation that wherever W does not depend on X_m its divergence vanishes, i.e.,

$$\partial P_{lj} / \partial X_j = 0 \quad (2.5)$$

(c.f. (5)) This latter property still holds if the energy momentum tensor is defined as

$$P_{lj} = \frac{\partial L}{\partial u_{i,j}} u_{i,l} - L \delta_{lj} \quad (2.6)$$

where L is a Lagrangian. The Euler equations, such that the integral of L over a region of X_m space is an extremum, then correspond to the equilibrium equations (2.3) when $L = -W$. With this formalism more general situations can be considered see (5—10) for some application.

We are primarily interested here with the elastic situation and hence equation (2.4) and its connection with the force on a defect. In (5) the situation shown in Fig. 1 is considered; Fig. 1 represents a body subject to surface loading and containing a defect D_1 together with other defects D_2 . If D_1 suffers a small vector displacement $\delta \xi_i$, it is shown that the change in total energy of the system (elastic energy plus potential energy of the loading mechanism) δE_{tot} is given as:

$$\delta E_{tot} = -\delta \xi_l F_l \quad (2.7)$$

where

$$F_l = \int_S P_{lj} dS_j \quad (2.8)$$

S is any surface surrounding D_1 and isolating it from D_2 . F_l is thus the force on the defect, where, following (5), the rate of decrease of the total energy of the system with respect to a parameter is defined as the generalized force acting on that parameter. Furthermore from (2.5) S may be deformed without altering F_l provided it remains in material where W does not depend explicitly on X_l (S still isolates D_1 from D_2 , of course).

It is also possible to use the energy-momentum tensor to calculate the force on an interface. Consider the situation shown in Fig. 2 where we assume the material inside B is a cavity with surface S. S may be closed or, as indicated by the dotted lines, may extend to the specimen surface. It is now supposed that S has developed a blister changing it to S', geometrically this can be specified by erecting a small vector $\delta \xi_{\ell}$ at each point of S. It can then be shown see (5) that the change in the total energy due to the formation of the blister is

$$\delta E_{\text{tot}} = - \int_S \delta \xi_{\ell} P_{\ell j}^A dS_j \quad (2.9)$$

where $P_{\ell j}^A$ is the energy momentum tensor on the A side of S and the normal in $dS_j = n_j dS$ is directed outwards from B to A. The results derived in (5) also apply to the situation when B may be 'transformed' elastic region which may have different elastic properties but such that the displacement is continuous across S and then (2.9) is written as

$$\delta E_{\text{tot}} = - \int_S \delta \xi_{\ell} ([W] \delta_{\ell j} - P_{ij} [u_{i,\ell}]) dS_j \quad (2.10)$$

where $[W]$ means the jump in W across S. Using the result

$$[u_{i,\ell}] = \left[\frac{\partial u_i}{\partial n} \right] n_{\ell} \quad (2.11)$$

where $\partial/\partial n$ denotes differentiation along the normal it is possible to interpret (2.10) as saying that there is an effective normal force

$$F = [W] - T \cdot \left[\frac{\partial u}{\partial n} \right] \quad (2.12)$$

per unit area of interface where T is the surface traction at the interface. Note that for a stress free cavity this result says that F becomes the energy density at the surface (a necessarily positive quantity), hence any increase in volume leads to a decrease of E_{tot} (this result has been derived in the small-displacement case by Rice and Drucker (11)).

Thus we have two important expressions for the change in total energy with respect to different kind of configurational change. The first given by (2.7) and (2.8) applies directly to a crack like defect. When the crack extends in its plane in the 1 direction say then F_1 given by (2.8) is equivalent to G , the crack extension force. Moreover, by its nature this crack extension involves no removal of material. Expression (2.9) on the other hand extends a cavity by forming a blister which does remove material. Even though a physical mechanism can be involved for this, e.g., diffusion or perhaps multiple cracking it does seem to have a different character. Nevertheless, applying the blister argument to a thin cavity can be shown to give the same result as that produced by applying (2.8) in the limit that the cavity is very thin (c.f. (5)).

In addition to the above uses of the energy-momentum tensor in calculating energy release due to defect motion or blister formation, it is also possible to calculate energy release due to cavity expansion or rotation. To do this some useful tools are path-independent integrals first discovered by Gunther (12) and rediscovered more recently by Knowles and Sternberg (13). These can be written as

$$L_{kl} = \int (X_k P_{lj} - X_l P_{kj} + u_k P_{lj} - u_l P_{kj}) dS_j \quad (2.13)$$

and

$$M = \int (X_l P_{lj} - \frac{1}{2} u_l P_{lj}) dS_j \quad (2.14)$$

The L_{kl} are path-independent for a non-linear homogeneous isotropic medium, whereas the integral M is path independent for a homogeneous linear anisotropic medium (c.f. (9)). In particular for plane strain it can be shown that the expression (2.14) reduces to

$$M = \int X_l P_{lj} dS \quad (2.15)$$

See Eshelby (14) for some applications of this result. In (15), Atkinson and Leppington show how an amended M integral (which is not path-independent) can be deduced for materials with couple-stresses and how it can be used to prove a useful theorem about energy release rates in such materials.

Furthermore, the L and M integrals defined in (2.13) and (2.14) have been shown to be related to energy-release rates associated with cavity or crack rotation or expansion by Budiansky and Rice (16).

3. Simple Applications

In the last section we have outlined how the energy momentum tensor can be used to give a fairly unified approach to calculations of the force on a defect, or change in total elastic energy, under a variety of configuration changes. In this section we shall explore by means of simple examples the energy released when (i) a cavity changes position slightly, due to a slight displacement of a position coordinate or (ii) a small blister, such as discussed in Section 2, forms on a cavity surface. For comparison we shall also consider the situation when a crack initiates from a cavity. The important point to notice here is that these calculations tell us only what the release of elastic energy is, whether or not such changes can occur in practice depends on the amount of energy required to effect them.

Ex. 1 The circular hole in an infinite plate

Consider a small circular hole of radius a in an infinite plate (under plane stress or plane strain conditions) and a tensile loading at infinity in the 1 direction such that at $r = \infty$,

$$P_{11} = S, \quad P_{12} = 0 = P_{22} \quad (3.1)$$

and

$$P_{rr} = P_{r\theta} = 0 \quad \text{on the hole boundary}$$

A well known result in this case is that the stress-field given in polar coordinates (r, θ) , with origin at the hole center, is

$$\begin{aligned}
p_{rr} &= \frac{S}{2} (1 - a^2/r^2) + \frac{S}{2} (1 + 3a^4/r^4 - 4a^2/r^2) \cos 2\theta \\
p_{\theta\theta} &= \frac{S}{2} (1 + a^2/r^2) - \frac{S}{2} (1 + 3a^4/r^4) \cos 2\theta \\
p_{r\theta} &= -\frac{S}{2} (1 - 3a^4/r^4 + 2a^2/r^2) \sin 2\theta
\end{aligned} \tag{3.2}$$

Thus on the boundary of the hole $p_{rr} = p_{r\theta} = 0$ and

$$p_{\theta\theta} = S(1 - 2 \cos 2\theta) \tag{3.3}$$

Calculating F_ℓ as defined in Equation (2.8), by evaluating the integral around a closed contour enclosing the hole, gives the force on the hole (recall that $\delta E_{\text{tot}} = -\delta\xi_\ell F_\ell$, Equation (2.7)) when the origin of the hole is moved by $\delta\xi_\ell$. The value turns out to be zero which is not so surprising since any position of the hole in the infinite plate is as good as any other. However, if we imagine that a blister forms on the hole we can calculate the energy change using Equations (2.9) or (2.10) of the last section. An elementary calculation gives

$$\int_{\theta_1}^{\theta_2} a W d\theta = \frac{aS^2}{2E} (3\theta - 2 \sin 2\theta + \frac{1}{2} \sin 4\theta) \tag{3.4}$$

and hence if a blister forms on $-\pi/4 < \theta < \pi/4$ say we have a release of energy $(aS^2/2E)(3\pi/2 - 4) |\delta\xi|$ whereas if a blister forms on $\pi/4 < \theta < 3\pi/4$ the energy released is $(aS^2/2E)(3\pi/2 + 4) |\delta\xi|$ making it energetically favorable for the blister to form on the side at right angles to the applied stress, an intuitively obvious result. The important point here is that these results give rise to a finite force per unit area of interface. Opposing this, of course, is the amount of energy required to form a blister which may be very large.

Suppose we consider an infinitesimal 'rectangle' of blister to be formed near $\theta = \pi/2$, then integrating (3.4) with $\theta_2 = \pi/2 \pm \delta\theta$ and applying (2.9) gives the change in total energy as

$$\begin{aligned}\delta E_{\text{tot}} &= -\frac{9S^2}{E} a\delta\theta \cdot \delta\xi \\ &= -\frac{9S^2}{2E} \delta A\end{aligned}\quad (3.5)$$

where $\delta A = 2a \delta\theta \cdot \delta\xi$ is the area of the blister which has been formed. It is of interest to compare this result with that of a crack of length ϵ initiated on the hole boundary at $\theta = \pi/2$ at right angles to the applied stress. For this case it is not difficult to show that if $\epsilon \ll a$ then the energy release rate or crack extension force, G , is

$$G = \epsilon(1.1215)^2 \pi \cdot \frac{9S^2}{2E}\quad (3.6)$$

Thus as the crack length ϵ tends to zero so does the energy release rate. This result is to be contrasted with the result (3.5) recalling that $\delta E_{\text{tot}} = -F\delta\xi$ where F is the force on the defect (the blister in this case). Thus

$$F = \frac{9S^2 a\delta\theta}{2E}\quad (3.7)$$

and as the blister gets very thin (almost crack like) F tends to zero with $a\delta\theta$. Note that for plane strain E (Young's modulus) is replaced by $E/(1 - \nu^2)$

Ex. 2 A step on the surface of a solid

For simplicity, we consider anti-plane deformation in a half-space $x_2 > 0$ with a step of height h situated on $x_2 = h$, $x_1 > 0$ and an external shear stress $P_{13} = \sigma$ applied at infinity.

This problem can be solved by conformal mapping and has been treated by Smith (17). The following results are obtained near the corner (0,h).

$$p_{13} = \sigma \left(\frac{4h}{3\pi r} \right)^{1/3} \cos \theta/3$$

$$p_{23} = \sigma \left(\frac{4h}{3\pi r} \right)^{1/3} \sin \theta/3$$
(3.8)

(p_{13} and p_{23} are, of course, the only non-zero stresses in anti-plane strain), r and θ are polar coordinates centered on the corner (0,h), $\theta = 0$ corresponds to the surface $x_2 = h$, $x_1 > 0$ and $\theta = 3\pi/2$ to the edge $x_1 = 0$, $0 < x_2 < h$. The energy density is now $(1/2\mu)(p_{13}^2 + p_{23}^2)$ and is infinite at the corner $r = 0$. However, integrating along $\theta = 0$, with respect to r will give a finite energy release rate (per unit surface area) for formation of a blister in the x_2 direction. Similar conclusions apply to the edge $x_1 = 0$, $0 < x_2 < h$. Note that in either case the effective force per unit surface area of the step will be proportional to $\sigma^2 h^{2/3}$. It is interesting to compare this with the energy release rate, G , associated with a crack of length ϵ emitting from (0,h) in the direction x_2 to the point (0,h + ϵ). For $\epsilon \ll h$ it is shown in (17) that this is

$$G = \sigma^2 (3\pi)^{1/3} h^{2/3} \epsilon^{1/3} / 2\mu$$
(3.9)

This tends to zero as ϵ tends to zero like $\epsilon^{1/3}$ so the presence of the corner although increasing $dG/d\epsilon$ compared with the corresponding result for a hole (Equation 3.6) still does not provide a finite crack extension force for crack initiation. The best we can do in this regard is to employ the force on an interface idea discussed in Section 2 (e.g., Equation 2.10). The result is often a finite effective force per unit area, but as indicated earlier this is offset by the energy required to remove material for such blister formation to be possible.

Perhaps, we must be content when discussing fracture from holes or corners to discuss the increased likelihood of fracture due to results like (3.9). Results of this general type have been derived for the more realistic plane strain situation by Atkinson (18) and in work in preparation by Atkinson and Avila (19).

References

- (1) Atkinson, C., Stress concentrations and fracture mechanics, Applied Mechanics Reviews,
- (2) Eshelby, J.D., The force on an elastic singularity, Phil. Trans. A244, 87 (1951).
- (3) Eshelby, J.D., The continuum theory of lattice defects, in F. Seitz and D. Turnbull (eds.) "Prog. Solid State Physics", Vol. 3, 79, (1956).
- (4) Atkinson, C. and Eshelby, J.D., The energy flow into the tip of a moving crack, Int. J. Fracture Mech. 4, 3 (1968).
- (5) Eshelby, J.D., Energy relations and the energy-momentum tensor in continuum mechanics, in Inelastic behavior of solids (ed. M.F. Kanninen et al) McGraw Hill (1970) 77-
- (6) Atkinson, C. and Leppington, F.G., Some calculations of the energy release G for cracks in micropolar and couple stress elastic media, Int. Jnl. of Fracture 10, 599- (1974).
- (7) Atkinson, C., Some results on crack propagation in media with spatially varying moduli, Int. Jnl. of Fracture 11, 619- (1975).
- (8) Atkinson, C., A note on some crack problems in a variable modulus strip, Arch. of Mechanics, 27, 639- (1975).
- (9) Eshelby, J.D., The elastic energy-momentum tensor, Jnl. of Elasticity, 5, 321 (1975).
- (10) Rice, J.R., A path independent integral and the approximate analysis of strain concentration by notches and cracks, J. Appl. Mech. 35, 379 (1968).
- (11) Rice, J.R. and Drucker, D.C., Energy changes in stressed bodies due to void and crack growth, Int. J. Frac. Mech. 3, 19 (1967).
- (12) Gunther, W., Abh. braunsch. wiss. Ges. 14, 54 (1962).
- (13) Knowles, J.K. and Sternberg, E., On a class of conservation laws in linearized and finite elastostatics, Arch. Rat. Mech. and Anal. 44, 187 (1972).
- (14) Eshelby, J.D., The calculation of energy release rates, 69, Prospects of Fracture Mechanics (ed. G.C. Sih et al) No-ordhoff, Leyden (1975).
- (15) Atkinson, C. and Leppington, F.G., The effect of couple stresses on the tip of a crack, Int. J. Sol. Structures 13, 1103 (1977).
- (16) Budiansky, B. and Rice, J.R., Conservation laws and energy release rates, J. Appl. Mech. 40, 201 (1973).

- (17) Smith, E., The stress concentration at a step on the surface of a brittle crystalline solid, Int. J. Engng. Sci. 6, 9 (1968).
- (18) Atkinson, C., On the stress intensity factors associated with cracks interacting with an interface between two elastic media, Int. J. Engng. Sci. 13, 489 (1975).
- (19) Atkinson, C. and Avila, J., in preparation.

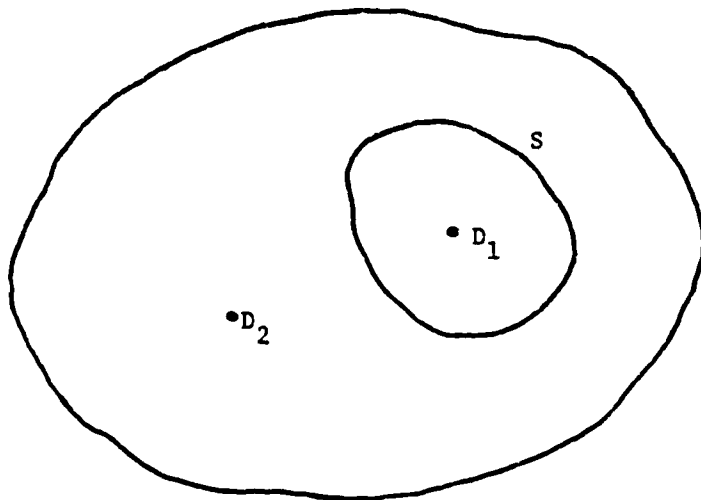


Figure 1

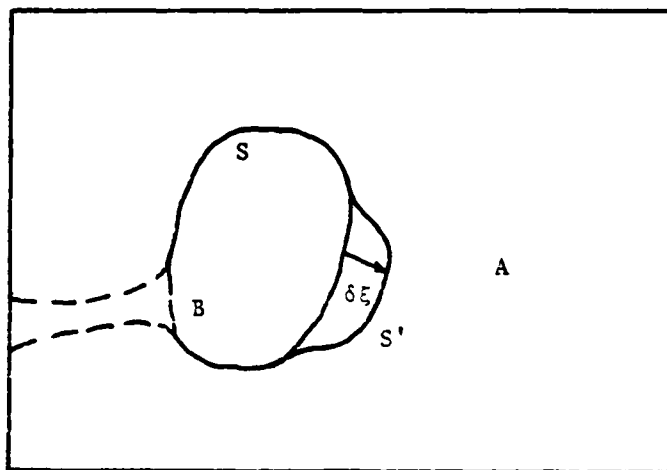


Figure 2

Appendix 4.3

Non-Local Elasticity and The Line Crack Problem

Dr. Colin Atkinson
Imperial College, London
Visiting Professor, University of Pittsburgh

Science of Fracture Research Project
AFOSR Contract #F49620-78-C-0101

School of Engineering
University of Pittsburgh
Pittsburgh, PA 15261

NON-LOCAL ELASTICITY AND THE LINE CRACK PROBLEM

C. Atkinson

Department of Mechanical Engineering, University of Pittsburgh

ABSTRACT

Further evidence is given to show that the classical line crack problem formulated for non-local elastic media with 'smooth' moduli may have no solution with non-infinite crack opening displacements. In particular, claims of finite crack tip stresses, etc., with this theory are likely to be incorrect. We give numerical results which support our earlier theoretical conclusions (1) and (2). Computations are made for a modulus which has an elastic component as well as the 'smooth' non-local moduli referred to above.

INTRODUCTION

In two recent papers (1) and (2) we have discussed calculations made by Eringen and co-workers of stresses around line cracks in a non-local elastic continuum (3,4,5). Our main conclusions in (1) were (i) that the approximation used (3,4,5) had a non-uniform character and hence would probably give unreliable results and (ii) that problems of the type solved numerically by Eringen et al. in (3) could be shown to have no solution with finite (i.e., non-infinite) crack opening displacements. In (2) we extended these results to plane strain situations and constructed solutions for a non-local theory with moduli which had a delta function component in addition to the 'smooth' moduli used by Eringen et al. With these amended non-local moduli it is not difficult to see that solutions should exist. However, the line crack problem will have the usual square root stress singularity at its tip. In principle it is possible to do calculations with such moduli and hence deduce stress intensity factors for media with such non-local constitutive laws. Thus stress intensity factors could then be used just as in classical fracture mechanics. The question, of course, is whether sensible (specific) constitutive relations can be obtained which are relevant to real materials. The constitutive laws chosen by Eringen et al. did attempt to connect with lattice theory through dispersion relations, but as we have suggested above and in (1) and (2) there are difficulties with the application of such a theory to the classical line crack problem.

In a private communication concerning (1) Dr. Eringen has claimed that for the non-local theory, boundary conditions cannot be applied in the classical sense. We do not know precisely what this means but he appears (in retrospect) to be trying to avoid just those regions of non-uniformity that we show exists in his approximation scheme. He also makes the comment that our proofs in (1) are not rigorous mathematical ones. To counter this criticism we present here in more rigorous form one of these proofs; filling in the gaps in the other proofs of (1) and (2) is left to the reader. It may be thought that the application of non-local theories to the fracture problem is only of academic interest, however some publicity has been given to non-local calculations which predict finite stresses at crack tips (6) and it would seem useful to attempt to clarify the matter, perhaps this conference can contribute something in this direction?

The plan of this paper is as follows: in Section 2 we state equations of equilibrium and constitutive equations for the linear non-local theory, and show how mathematical rigor can be added to the non-existence proofs of (1). Finally in Section 3 we describe some numerical results for a crack in a non-local elastic solid with modulus of the form

$$\alpha(|\underline{x}|) = b \delta(|\underline{x}|) + (1 - b) \alpha_1(|\underline{x}|) \quad (1.1)$$

(compare Section 2 for a fuller description of such constitutive laws) b is a constant $0 < b < 1$ and $\alpha_1(|\underline{x}|)$ is a smooth function of \underline{x} depending on a small parameter a (the lattice parameter). We have shown in (2) that for moduli of this general type when a (crack length) tends to zero, the crack tip displacement and stress field become respectively, the classical crack tip elastic displacement multiplied by $b^{-1/2}$ and the classical crack tip stress field multiplied by $b^{1/2}$. When $b \rightarrow 0$ equation (1.1) is a modulus of the type considered by Eringen. In this case our asymptotic results say that the crack opening displacement tends to infinity like $b^{-1/2}$ which supports the non-existence results of (1) and (2). As can be seen in Section 3, the numerical results confirm this asymptotic result.

2 ANALYSIS

The basic equations of linear, homogeneous, isotropic, non-local elasticity with vanishing body and inertia forces can be written as:

$$t_{kl,k} = 0 \quad (2.1)$$

$$t_{kl} = \int_V \{ \lambda'(|\underline{x} - \underline{x}'|) e_{rr}(\underline{x}') \delta_{ki} + 2\mu'(|\underline{x} - \underline{x}'|) e_{kl}(\underline{x}') \} dv(\underline{x}') \quad (2.2)$$

with

$$e_{kl} = \frac{1}{2} (u_{k,l} + u_{l,k}) \quad (2.3)$$

In the above equations the summation convention with respect to repeated indices is used, and the indices run from 1 to 3 in general. Clearly from (2.2) the stress $t_{k\ell}(\underline{x})$ at a point \underline{x} depends on the strains $e_{k\ell}(\underline{x}')$ at all points of the body. The integral in (2.2) is over the volume V of the body enclosed within a surface ∂V .

Various expressions for the non-local moduli $\lambda'(|\underline{x}|)$ and $\mu'(|\underline{x}|)$ have been used in the cited papers. Each of these is of the form

$$(\lambda', \mu') = (\lambda, \mu) \alpha(|\underline{x}' - \underline{x}|) \quad (2.4)$$

where (λ, μ) are constants and the function α is normalized so that

$$\int_V \alpha(|\underline{x}' - \underline{x}|) dV(\underline{x}') = 1 \quad (2.5)$$

the integration being over the whole body. Expressions for α which have been obtained by Eringen et al. by comparison with (one-dimensional) dispersion relations of lattice dynamics are:

$$(i) \quad \alpha(|\underline{x}' - \underline{x}|) = \alpha_0 (a - |\underline{x}' - \underline{x}|) \quad \text{for } |\underline{x}' - \underline{x}| \leq a \quad (2.6) \\ = 0 \quad \text{if } |\underline{x}' - \underline{x}| > a$$

a is the lattice parameter and α_0 is a normalization constant deduced from (2.5).

$$(ii) \quad \alpha(|\underline{x}' - \underline{x}|) = \alpha_0 \exp\left\{-\left(\frac{\beta}{a}\right)^2 (x'_k - x_k)(x'_k - x_k)\right\} \quad (2.7)$$

where the summation convention applies to k , β is a constant. See (3) and (4) for a justification of the use of these expressions.

Other examples for α were considered in (1) for illustrative purposes. One of these, for example, is

$$(iii) \quad \alpha(|\underline{x}|) = \frac{1}{\pi} \frac{a}{(|\underline{x}|^2 + a^2)} \quad (2.8)$$

Note that each of (2.6), (2.7) or (2.8), with the correct normalizing factor α_0 , have the property that formally letting $a \rightarrow 0$ implies $\alpha(|\underline{x}' - \underline{x}|) \rightarrow \delta(|\underline{x}' - \underline{x}|)$. This limiting case is, of course, classical elasticity, however with $a \neq 0$ moduli such as (2.6), (2.7) and (2.8) behave quite differently. Later as a contrasting example to the moduli of (2.6), (2.7) or (2.8) we shall consider moduli of the form

$$(iv) \quad \alpha(|\underline{x}' - \underline{x}|) = b \delta(|\underline{x}' - \underline{x}|) + (1 - b) \alpha_1(|\underline{x}' - \underline{x}|) \quad (2.9)$$

where b is a constant $0 < b < 1$ and α_1 is a function of the 'smooth' type discussed above {(2.6), (2.7) or (2.8)}. Expressions of type (2.9) have been suggested by Kroner (7).

Using equations (2.1), (2.2) and moduli (2.6) or (2.7) in the two dimensional form applicable to plane-strain, Eringen and co-workers in a series of papers (3,4,5) have treated boundary value problems of line cracks under various loading conditions, plane strain shear, plane strain tension and anti-plane shear. In (3) they treat a model problem via numerical solution of an integral equation and then develop an approximation procedure to which they attribute good accuracy. On the other hand we show in (1) and (2) that their approximation procedure is a non-uniform one and hence is likely to lead to unreliable results. Moreover in (1) and (2) we show that no solution with finite (i.e., non-infinite) crack opening displacements, can exist for the problems posed and treated numerically by Eringen et al (3,4,5). The way this was done was to reduce the problem to an integral equation and then use analytic continuation arguments to show that no solution with non-infinite displacements could exist. For example in(1) we reduced the model problem considered in (3) to the integral equation

$$1 = \int_{-L}^L K(x - \xi) f(\xi) d\xi, \quad |x| \leq L \quad (2.10)$$

(for convenience we have replaced a constant by unity) $f(\xi)$ is a dislocation density (for laplaces equation) so that the integrability of $f(\xi)$ is necessary for non-infinite crack opening displacements. The problem is to find integrable $f(\xi)$ satisfying (2.10) for a specified kernel K resulting from a given non-local modulus. The reader is referred to (1) and (2) for more details, here we consider again the simple example given by (2.8). In this case

$$K(x) = \frac{x}{x^2 + a^2} \quad (2.11)$$

Note that when a equals zero (2.10) is a singular integral equation which has a well known solution and is similar to that derived by representing a crack by a distribution of dislocations. However for $a \neq 0$ the following non-existence proof can be devised.

Non-Existence Proof

For complex z , define

$$\phi(z) = \int_{-L}^L K(z - \xi) f(\xi) d\xi \quad (2.12)$$

This makes sense in the strip $|\text{Im } z| < a$ and is analytic in z . Furthermore, $\phi(z) = 1$ for $z = x$, $|x| \leq L$ hence $\phi(z) \equiv 1$ in the whole region $|\text{Im } z| < a$, and in particular for $z = x$ (real) for all x . (Here the theorem used is that if $\psi(z)$ is analytic in region D , and $\psi(z) = 0$ at a sequence of points $z = z_n$ with $z_n \rightarrow z^*$ in D then $\psi(z) = 0$ in D .) However, for real $x > L$, and $|\xi| \leq L$

$$|K(x - \xi)| \leq \frac{1}{|x - \xi|} \leq \frac{1}{x - L} \quad (2.13)$$

so

$$|\phi(x)| \leq \frac{1}{x - L} \int_{-L}^L f(\xi) d\xi$$

This gives $\phi(x) \rightarrow 0$ as $x \rightarrow +\infty$ contradicting $\phi(x) \equiv 1$.

This rigorises the non-existence argument given in (1). In the next section we consider the numerical solution of line crack problems with moduli of the form given by (2.9), i.e., where there is an 'instantaneous' elastic component to the modulus.

3 NUMERICAL SOLUTION OF LINE CRACK PROBLEMS IN NON-LOCAL MEDIA WITH MODULI OF THE FORM $\alpha(|\underline{x}|) = b \delta(|\underline{x}|) + (1 - b) \alpha_1(|\underline{x}|)$

In this section we consider a line crack problem of length 2 in anti-plane shear where the non-local modulus is of the form given in (2.9). In this case there is only one non-zero displacement component u_3 , equation (2.1) reduced to

$$t_{13,1} + t_{23,2} = 0 \quad (3.1)$$

and (2.2) reduces to

$$t_{k3} = \int_S \mu'(|\underline{x} - \underline{x}'|) u_{3,k} dS(\underline{x}') \quad (3.2)$$

with $\underline{x} = (x_1, x_2)$ and the integral in (3.2) being over the whole (x_1, x_2) space. We use the usual line crack formulation and consider the stress boundary condition on the crack line as

$$t_{23}(x_1^0) = -t_0(\text{constant}), \quad |x_1| < 1 \quad (3.3)$$

Because of the normalizing condition (2.5) on the modulus μ' it is clear that $u_{3,2} = t_0$ in (3.2) corresponds to $t_{23} = t_0$ so a uniform stress could be added to the problem giving a stress free crack. A formulation like this is common to the cited papers. For the numerical analysis given here, we consider a specific form for $\mu'(|\underline{x}|)$, this is $\mu'(|\underline{x}|) = \mu\alpha(|\underline{x}|)$ where

$$\alpha(|\underline{x}|) = b \delta(|\underline{x}|) + \frac{(1 - b)}{2\pi\ell} \delta(|\underline{x}| - \ell) \quad (3.4)$$

Note that $\int_S \alpha(|\underline{x}|) dS(\underline{x}) = 1$ and δ is the delta function. Defining

$$\sigma_{k3} = \mu u_{3,k} \quad (3.5)$$

arguments are given in (3), (4) and (5) to show that equation (3.1) implies the equation

$$\sigma_{k3,k} = 0 \quad (3.6)$$

Using screw dislocation solutions of (3.6) with (3.5) and thus automatically satisfying the condition of continuity of displacement outside the crack the following integral equation is derived in (2).

$$t_{23}(x_1, 0) = \frac{\mu}{2\pi} \int_{-1}^1 f_3(\eta) K(x_1 - \eta) d\eta \quad (3.7)$$

where $f_3(\eta)$ is the unknown dislocation density, $\int_{-1}^1 f_3(\eta) d\eta = 0$ is a necessary condition for the crack to close at $x_1 = \pm 1$ and

$$K(t) = 2 \int_0^{\infty} dx_2^1 \int_{-\infty}^{\infty} \frac{\alpha(|x_1^1|, |x_2^1|) (x_1^1 + t) dx_1^1}{(x_1^1 + t)^2 + x_2^1{}^2} \quad (3.8)$$

Using (3.4) equation (3.7) can be written as

$$\frac{2\pi}{\mu} t_{23}(x_1, 0) = b \int_{-1}^1 \frac{f_3(\eta) d\eta}{x_1 - \eta} + (1 - b) \int_{-1}^1 f_3(\eta) K_1(x_1 - \eta) d\eta \quad (3.9)$$

The kernel K_1 comes from using the second part of (3.4) in (3.8). We have solved the singular integral equation (3.9) by turning it into a Fredholm equation in the manner described in (8) and then solving this equation numerically (the derivation is too lengthy to include here).

Writing

$$f_2(\eta) = -N(\eta)/(1 - \eta^2)^{1/2} \quad (3.10)$$

we have calculated $N(1)$ for various ℓ and b values. Note that the crack opening displacement at the tip $x_1 = 1$ will be proportional to $N(1)(1 - x_1^2)^{1/2}$ so the square root singularity common to the classical elasticity problem occurs. The calculation is a sensitive one especially for small values of b so results are shown for increasing values of M the number of unknowns in the discretization of the Fredholm integral equation. When $b = 1$, the elastic case, the exact result is $N(1) = .31831$. Now according to the results derived in (2) when ℓ tends to zero the displacement at the crack tip should have $N(1) = (.31831) b^{-1/2}$, i.e., the elastic crack tip displacement multiplied by $b^{-1/2}$. As can be seen in the table the agreement with this limiting result is very good.

$\ell = .5$	$b = .9$.8	.7	.6	.5	.4
M = 40	.34142	.36866	.40143	.44192	.49385	.56406
M = 60	.34169	.36923	.40232	.44307	.49500	.56433
M = 100	.34186	.36966	.40315	.44458	.49768	.56926
$\ell = .2$						
M = 40	.33661	.35782	.38284	.41292	.4500	.4973
M = 60	.33730	.35938	.38551	.41716	.4574	.5085
M = 100	.33794	.36091	.38832	.42181	.4641	.5198
$\ell = .1$						
M = 50	.33348	.35074	.3706	.3938	.4215	.4552
M = 60	.33435	.3528	.3743	.4001	.4328	.4596
M = 100	.33549	.3554	.3788	.4070	.4416	.4857
$(.31831)b^{-1/2}$.33553	.3559	.3805	.4109	.4502	.5033

TABLE 1 Values of $N(1)$

4 CONCLUDING REMARKS

In the earlier sections and in references (1) and (2) we have specifically addressed the line crack problem and what certain non-local (continuum) calculations have to say about it. We hope to have supplied sufficient argument to suggest that the claims in (6) are unsubstantiated. Whether some modification of the boundary conditions, etc., may resolve the difficulties we have referred to, is at present unproven. Note, however that if one were satisfied with a singular stress at a line crack tip then one could still have continua with some non-local behavior such as considered in Section 3. Finally, we mention more abstract approaches such as those of Rogula (9). In principle we believe they should confirm the spirit of our conclusions.

ACKNOWLEDGMENT

We would like to thank the Air Force Office of Scientific Research under contract No. F49620-78-0101 for its financial support and G.E.H. Reuter for his suggestion of improving the rigor of the non-existence proof of (1).

REFERENCES

- (1) Atkinson, C., On some recent crack tip stress calculations in non-local elasticity. Arch. of Mechanics (1980) to appear.
- (2) Atkinson, C., Crack problems in non-local elasticity. Arch. of Mechanics (to appear).
- (3) Eringen, A C., Speziale, C.G. and Kim, B.S., Crack tip problem in non-local elasticity. J. Mech. Phys. Solids, 25, 339-356 (1977).
- (4) Eringen, A.C., Line crack subject to shear. Int. J. Fracture, 14, 367-379 (1978).
- (5) Eringen, A.C., Line crack subject to anti-plane shear. Eng. Frac. Mechs., 12, 211-219 (1979).
- (6) Advanced Elasticity Theory Solves Outstanding Problem in Fracture Mechanics, Naval Research Reviews, April 1977.
- (7) Kroner, E., Elasticity theory of materials with long range cohesive forces. Int. J. Solids Structures, 3, 731-742 (1967).
- (8) Atkinson, C., On dislocation densities and stress singularities associated with cracks and pile ups in inhomogeneous media. Int. J. Engng. Sci., 10, 127-136 (1972).
- (9) Rogula, D., On non-local continuum theories of elasticity. Arch. Mech., 25, 233-251 (1973).

PRECEDING PAGE BLANK-NOT FILLED

Appendix 4.4

Combined Mode Fracture Via The
Cracked Brazilian Disk Test

Dr. Colin Atkinson
Imperial College, London
Visiting Professor, University of Pittsburgh

Dr. Ronald E. Smelser
Assistant Professor

Jaime Sanchez
Graduate Assistant
(Now with: Universidad del Valle Cali, Columbia)

Science of Fracture Research Project
AFOSR Contract #F49620-78-C-0101

School of Engineering
University of Pittsburgh
Pittsburgh, PA ;5261

STATUS OF BRAZILIAN DISK TEST INVESTIGATION

The preliminary investigation of the cracked Brazilian disk test was completed. The results of this work are summarized in the attached manuscript which has been accepted for publication in the International Journal of Fracture. Further analytical and experimental work on the test geometry are warranted to assess the applicability of the specimen for evaluation of mixed mode fracture.

In addition, J. Avila has completed an M.S. thesis on the rod pull out problem. The major finding of this work was that debonding of the rod from the surface was favored for most initial flaw configurations. The work also presented a simple scheme for obtaining energy release rates using only numerical data from an unflawed specimen. This obviates the need for numerous computer solutions of differing flaw lengths or the use of complicated data reduction schemes to obtain energy release data. The findings of this work are currently being summarized in a manuscript to be submitted for publication.

The parametric study of this problem is being pursued by M. Klienowsky. Some numerical difficulties have been encountered in the finite element scheme for certain of the geometries. These problems are currently being studied and should be resolved shortly. The results of this study should be available within the year.

1. INTRODUCTION

Recently, a series of papers by Eftis et al. [1,2,3] has re-examined the problem of an inclined crack in a plate under remote biaxial loading. Their purpose was to demonstrate the effect of remote stresses and load biaxiality on K_I and K_{II} as well as the effect on various fracture criteria. A critical review of the various fracture criteria has been given by Swedlow [4]. Here it is pointed out that the existing test data do not allow any selection to be made between the various competing criteria, and it is recommended that alternative tests be considered as well as an expansion of the data base for combined mode fracture.

It is in this later area where the current specimen would seem to be most useful. The specimen geometry is shown in Figure 1 and is a variant of the early work of Libatskii and Kovchik [5] and Yarema and Krestin [6]. The specimen of Figure 1 has been investigated by Ajawi and Sato [7] and by Sanchez [8] as an alternative to the compact shear specimen of Jones and Chisholm [9, 10]. In addition to the determination of K_{IIC} , Awaji and Sato [7] also examined the possibility of the existence of a fracture criteria in the form

$$\left(\frac{K_I}{K_{IC}}\right)^u + \left(\frac{K_{II}}{K_{IIC}}\right)^u = 1 \quad (1.1)$$

In contrast to the numerical analyses of [7,8], we present explicit formulae for K_I and K_{II} valid for any angle of crack orientation in the cracked Brazilian disk test, Eq. (3.1). Also, an approximate analysis valid for short cracks is given, and the effect of friction is included when crack closure is presented. Finally, experimental results are presented which demonstrate the feasibility of producing short cracks in moderate size specimens, thus indicating the usefulness of the approximate analysis and of the specimen geometry in expanding and illucidating the problem of combined mode fracture.

2. ANALYSIS

To give a complete numerical treatment of the problem, we follow a method outlined by Atkinson [11]. The crack is represented by a continuous distribution of edge dislocations, simulating discontinuities in the normal and tangential components of displacement. Because the crack lies on a diameter of the disc, there is no interaction between dislocations representing discontinuities in the normal displacement and those representing discontinuities in the tangential displacement. The tractions on the axis $y=0$ due to the unknown distribution of dislocations can be written in the form

$$\frac{\sigma_{i2}}{D} = \int_{-\ell}^{\ell} \frac{N_i(c)dc}{x-c} + \int_{-\ell}^{\ell} N_i(c)H_i(c,x) dc \quad i = 1,2 \quad (2.1)$$

The precise form for $H_i(c, x)$ can be deduced from [12] where the case of a circular inclusion was considered. Note, however, a misprint in equation (2.2.2) of [12]. The factor in the last term in the curly brackets should be $\frac{2}{\beta a}$ not $\frac{x^2}{\beta a}$. In (2.1), $D = \frac{2G}{(\kappa + 1)}$, G is the shear modulus, and $\kappa = 3-4\nu$ (plane strain) or $\kappa = \frac{3-\nu}{1+\nu}$ (plane stress) ν being Poisson's ratio. For convenience, we have taken the Burger's vector, \underline{b} , to be unity. The corresponding opening of the crack faces can be written

$$\Delta u_i = \int_x^{\ell} N_i(c) dc \quad i = 1,2 \quad (2.2)$$

where (u_1, u_2) are the (x, y) components of the displacement, and σ_{ij} is the usual stress tensor. The subsidiary conditions

$$\int_{-\ell}^{\ell} N_i(c)dc = 0 \quad i = 1,2 \quad (2.3)$$

ensure that the crack closes at the ends $(\pm \ell, 0)$.

The distributions $N_i(c)$ are to be determined from the condition that the crack be stress free and that it closes at the ends (condition (2.3)). The first of these conditions is met by replacing σ_{i2} in (2.1) by minus the stress induced on the crack line ($|x|=\ell$, $y=0$) by the applied stresses set up in the disc in the absence of the crack. Complete expressions for these stresses are given in Appendix 1. For the moment, we assume the stress is represented by

$$\sigma_{i2}(x) = -\sigma_i(x) \quad i = 1, 2 \quad (2.4)$$

given on $y=0$, $|x| \leq \ell$. Equation (2.1) then becomes an integral equation for the unknown densities $N_i(c)$.

Two methods of treating this equation numerically are given in [11]. One of these methods consists of solving (2.1) directly by expanding (2.1) in terms of Chebyshev polynomials. The other method consists of first transforming (2.1) into a Fredholm equation and then solving it numerically. We use the latter method here since it is possible to express the kernel in closed form.

Using (2.4) in (2.1) the resulting Fredholm equation can be written (see Atkinson [11])

$$N_{i1}(\eta) = \frac{-1}{\pi^2(1-\eta^2)^{1/2}} \left[\int_{-1}^1 \frac{\sigma_i(\ell x_1) (1-x_1^2)^{1/2}}{x_1 - \eta} dx_1 + \int_{-1}^1 N_{i1}(c_1) F_i(c_1, \eta) dc_1 \right] \quad i = 1, 2 \quad (2.5)$$

where $c = \ell c_1$, $a = \ell a_1$, $x = \ell x_1$,

$$F_i(c_1, \eta) = \int_{-1}^1 \frac{H_i(\ell c_1, \ell x_1) (1-x_1^2)^{1/2}}{x_1 - \eta} dx_1$$

and $N_{i1}(\eta) = N_i(\ell\eta)$. Making these coordinate transformations in (2.2), gives

$$\Delta u_i(x, 0) = \ell \int_{-1}^1 N_{i1}(c_1) dc_1 \quad (2.6)$$

We expect $N_{i1}(\eta)$ to have inverse square root singularities at $\eta = \pm 1$, so we write

$$N_{i1}(\eta) = N_{i0}(\eta) (1-\eta^2)^{-\frac{1}{2}} \quad (2.7)$$

Now make the substitutions $\eta = \cos \alpha$, $c_1 = \cos \psi$ and $x_1 = \cos \psi_1$ so that equations (2.5) become

$$N_{i0}(\cos \alpha) = \frac{-1}{\pi^2} \left[f(\cos \alpha) + \int_0^\pi N_{i0}(\cos \psi) F_i(\cos \psi, \cos \alpha) d\psi \right] \quad (2.8)$$

for $0 \leq \alpha \leq \pi$. $f(\cos \alpha)$ is to be derived from the first integral on the right of equation (2.5). Note that $F_i(\cos \psi, \cos \alpha)$ can be expressed in closed form by completing the integral following Equation (2.5).

The next step in the solution of the problem is to replace the integral in (2.8) as a sum and solve the resulting system of simultaneous equations. Once this is done, substituting into (2.6) shows that

$$\Delta u_i(x,0) = (2\ell)^{\frac{1}{2}} N_{i0}(1) (\ell-x)^{\frac{1}{2}} \quad (2.9)$$

as $x \rightarrow \ell_-$. Furthermore, from (2.2), the crack opening displacements along the crack flanks can be computed as

$$\Delta u_i(x,0) = \ell \int_0^{\psi_1} N_{i0}(\cos \psi) d\psi \quad (2.10)$$

where $\psi_1 = \cos^{-1}(x/\ell)$

3. RESULTS

The analysis of section 2 may be used to determine the stress intensity factors associated with cracks of varying length and orientation. Such a determination requires the evaluation of $f(\cos \phi)$ in Equation (2.8). $f(\cos \phi)$ may be evaluated through an expansion of $\sigma_i(x)$ in terms of Chebyshev polynomials and then numerically integrating to determine $f(\cos \phi)$. This procedure is numerically sensitive. Thus an alternate method of evaluating $f(\cos \phi)$ was used. Each term in the approximate stress distributions given in Appendix 1 may be independently used to solve Equation (2.8). The resulting $N_{I0}(1)$'s yield series approximations to the stress intensity factors in the form

$$N_I = \sum_{i=1}^n T_i \left(\frac{\ell}{a}\right)^{2i-2} A_i(\theta) \quad (3.1)$$

$$N_{II} = 2 \sin 2\theta \sum_{i=1}^n S_i \left(\frac{\ell}{a}\right)^{2i-2} B_i(\theta)$$

where $N_I = \frac{K_I}{\sigma_o \sqrt{\pi\ell}}$, $N_{II} = \frac{K_{II}}{\sigma_o \sqrt{\pi\ell}}$ are normalized stress intensities and

$\sigma_o = \frac{P}{\pi a}$. The T_i 's and S_i 's in (3.1) are numerical factors determined through the solution of (2.8). The first five values of T_i and S_i and the corresponding $A_i(\theta)$'s and $B_i(\theta)$'s are given in Tables 1 and 2 respectively.

The normalized uncracked disk stress distributions, $\sigma_{\theta\theta} = \frac{\bar{\sigma}_{\theta\theta}}{\sigma_o}$ and $\sigma_{\phi\theta} = \frac{\bar{\sigma}_{\phi\theta}}{\sigma_o}$ for $\frac{c}{a} = 0.6$ are shown in Figure 2. As can be seen, the two term approximation yields a stress distribution greatly differing from the analytical solution. However, the approximation improves

for small $\frac{\rho}{a}$, Figure 3. The stress distributions of Figure 2 produce only small differences in stress intensity factors as evidenced in Figure 4. Here N_I and N_{II} for the two and five term approximations for $\frac{\ell}{a} = 0.5$ are compared with the numerical results of Awaji and Sato [7]. For the five term approximations, no discernible differences can be detected in the results, while the two term approximation shows differences of less than ten percent. This small difference for the two term approximation is due to the dominance of the first term of the expansion. In addition, Figure 4 also contains a series of finite element calculations due to Sanchez [8]. These results were obtained using a special crack tip element of Tong et al. [13] in a mesh of constant strain elements. The computations are seen to be in agreement with the other numerical results for the coarse mesh of Figure 5.

Figure 4 shows that as the crack changes its orientation from the vertical to the horizontal the normalized stress intensity factor N_I changes from positive to negative indicating crack closure. At the point of crack closure, the model of the crack must be altered. This point was not considered in [7] and in general has not been incorporated in problems of mixed mode fracture [1-3]. Condition (2.2) must be modified so that

$$\Delta u_2 = 0 \quad (3.2)$$

for $\ell^* \leq |x| \leq \ell$ where ℓ^* is the position at which the crack first closes and $0 \leq \ell^* \leq \ell$ on $y = 0$. Now if Δu_2 is zero, an additional traction, $\sigma_{12}^*(x)$, is developed along the crack surface due to friction

$$\tau_{12}^*(x) \leq \mu \sigma_{22}(x) \quad (3.3)$$

In the following section, an analysis for short cracks is presented and the effect of friction is incorporated.

4. SMALL CRACK APPROXIMATION

If the crack length is small relative to the radius, then the second term on the right of (2.1) may be neglected, and the problem treated as a crack in an infinite media. Equation (2.1) becomes

$$\frac{\sigma_{i2}}{D} = \int_{-\ell}^{\ell} \frac{N_i(c) dc}{x - c} \quad i = 1, 2 \quad (4.1)$$

Now from Appendix 1, the normal and shear stresses along the crack line are approximately

$$\bar{\sigma}_{22}(x) = \frac{P}{\pi a} [A_1 + A_2 \left(\frac{x}{a}\right)^2] \quad (4.2)$$

$$\bar{\sigma}_{12}(x) = \frac{2P \sin 2\theta}{\pi a} [B_1 + B_2 \left(\frac{x}{a}\right)^2]$$

since $x = \rho$ on $y = 0$. Now, $\bar{\sigma}_{22}(x)$ and $\bar{\sigma}_{12}(x)$ are even functions of x , and the normalized stress intensity factors may be written as

$$N_I = \frac{1}{\sigma_o \pi} \int_{-\ell}^{\ell} \frac{\sigma_{22}(x) dx}{(\ell^2 - x^2)^{1/2}} \quad (4.3)$$

$$N_{II} = \frac{1}{\sigma_o \pi} \int_{-\ell}^{\ell} \frac{\sigma_{12}(x) dx}{(\ell^2 - x^2)^{1/2}}$$

[Note, N_I and N_{II} are not to be confused with the dislocation densities $N_i(c)$.]

Substituting (4.2) into (4.3) and integrating yields explicitly

$$N_I = A_1 + \frac{A_2}{2} \left(\frac{\ell}{a}\right)^2 \quad (4.4)$$

$$N_{II} = B_1 + \frac{B_2}{2} \left(\frac{\ell}{a}\right)^2$$

A comparison of expressions (4.4) with expressions (3.1) and the finite element results are given in Figure 6 with $\frac{\ell}{a} = 0.3$. The approximations of (4.4) are seen to be quite good.

From Equation (4.4)₁ we may obtain an explicit equation for the angle at which the crack just begins to close

$$N_I = A_1 + \frac{A_2}{2} \left(\frac{\ell}{a}\right)^2 = 0 \quad (4.5)$$

This expression has been evaluated for fixed values of $\frac{\ell}{a}$, and the results are compared with those of [7,8] in Table 3. For angles of inclination greater than those in Table 3, the crack closes over some portion of its surface and a frictional stress is developed.

If in (4.5) θ is fixed in deference to $\frac{\ell}{a}$, we obtain an equation for the position, ℓ^* , at which the crack closes. Now equations (4.4) obtain for $\rho \leq \ell^*$. If $\ell \geq \ell^*$, we have in addition to the stress intensity factor N_{II} given by (4.4)₂ an additional contribution due to the frictional stress. We note that this is true even if N_I is constrained from being negative by imposing $\Delta u_2 = 0$ on $y = 0$ for $0 \leq \ell^* \leq |x| \leq \ell$. Additionally, this is true in the general case since there is no interaction between the normal and shear dislocations.

To evaluate the additional contribution to N_{II} , we must evaluate the stresses in the region $\ell^* \leq |x|$. The stresses ahead of the crack in this small crack approximation are given by

$$\frac{\sigma_{22}(x)}{D} = \int_{-\ell^*}^{\ell^*} \frac{N_2^*(c) dc}{c - x} \quad (4.6)$$

The $N_2^*(c)$ can be determined from the first term on the right hand side of Equation (2.5) provided we replace ℓ by ℓ^* , η by c and use expression (4.2)₁ for $-\sigma_I(x)$ with the condition that $\Delta u_2 = 0$ on $y = 0$ $|x| > \ell^*$.

Equation (4.6) may then be evaluated to give, for $|x| > \ell^*$

$$\sigma_{22}(x) = \frac{\sigma_o x}{\sqrt{x^2 - \ell^{*2}}} \left[A_1 - \frac{A_2}{a_2} (x^2 - \ell^{*2}) \right] \quad (4.7)$$

and the friction stress within the contact zone is given by

$$\sigma_{12} = -\mu \sigma_{22} \quad (4.8)$$

μ being the coefficient of friction.

So in addition to the stress intensity factor N_{II} of (4.4)₂, we have from (4.3)₂

$$N_{II}^* = \frac{-2\mu}{\sigma_o \pi} \int_{\ell^*}^{\ell} \frac{\sigma_{22}(x) dx}{(\ell^2 - x^2)^{1/2}} \quad (4.9)$$

in the zone $\ell^* \leq |x| \leq \ell$. Inserting $\sigma_{22}(x)$ from (4.7), we find

$$N_{II}^* = \frac{-\mu A_2}{2} (\ell^2 - \ell^{*2})$$

which must be added to (4.4)₂ to account for the friction developed within the contact zone.

5. EXPERIMENTAL RESULTS

Tests were conducted on a commercial grade of polymethyl methacrylate (PMMA) with an elastic modulus of 0.5×10^6 lb/in² and a tensile strength of 8×10^3 lb/in². The specimens were 1.5 in. in diameter and approximately 0.125 in. thick. Details of the specimen preparation and testing procedures may be found in [8]. In addition, a series of three point bend tests were also conducted. To avoid errors which may be produced in specimen preparation, the beam specimens were cut from 3.0 inch disks which were prepared in a fashion identical with the 1.5 in disks. The results for the opening mode failure are given in Fig. 7. In Fig. 7, K_I has been normalized by using the average K_{IC} values from both the bend specimen and the disk test. As is evident, the experimental results follow the analytical curve of Libatskii and Kovchik [5] quite closely with maximum deviation at short crack lengths.

Figure 8 presents results for the mode II fracture of PMMA. The results here show greater scatter than in mode I. This is most probably due to the precision required in orienting the specimen. Nevertheless, it is felt that the above results demonstrate the feasibility of using the disk test as a reliable method for obtaining K_{IC} and K_{IIC} fracture parameters. Additionally, the testing also demonstrates that the production of specimens of modest size with small $\frac{l}{a}$ ratios is feasible. This coupled with analysis of Section 4 will allow a detailed study of the effects of combined mode fracture as well as the role of friction in the failure event.

6. CONCLUSIONS

The foregoing has presented an analysis of the cracked Brazilian disk test. The results of a numerical investigation yielded explicit formulae for the mixed mode stress intensity factors valid for any crack orientation. In addition, it was noted that for some angle the opening mode stress intensity factor became zero, and beyond this angle, the crack was closed. An approximate analysis was developed for short cracks and a scheme for the inclusion of friction was presented. Experiments were conducted on PMMA specimens, and it was demonstrated that modest size specimens could be produced with short crack lengths which yield reliable results. Thus, it is possible to analyze and investigate the problem of combined mode fracture using the cracked Brazil disk test.

Acknowledgement: The authors would like to thank the Air Force Office of Scientific Research for its financial support through the course of this work and M.L. Williams for his help and encouragement.

REFERENCES

1. J. Eftis, N. Subramonian, and H. Liebowitz, *Engineering Fracture Mechanics*, 9, 189-210 (1977).
2. J. Eftis, N. Subramonian, and H. Liebowitz, *Engineering Fracture Mechanics*, 9, 753-764 (1977).
3. J. Eftis and N. Subramonian, *Engineering Fracture Mechanics*, 10, 43-67 (1978).
4. J.L. Swedlow, in *Cracks and Fracture*, *ASTM STP 601*, 506-521 (1976).
5. L.L. Libatskii and S.E. Kovchik, *Soviet Materials Science*, 3, 334-339 (1967).
6. S. Ya. Yarema and G.S. Krestin, *Soviet Materials Science*, 2, 7-10 (1966).
7. H. Awaji and S. Sato, *Journal of Engineering Materials and Technology*, 100, 175-182 (1978).
8. J. Sanchez, Application of the Disk Test to Mode I-II Fracture Analysis, MS Thesis, Mechanical Engineering Department, University of Pittsburgh, Pittsburgh, PA (1979).
9. D.L. Jones and D.B. Chisholm, *Engineering Fracture Mechanics*, 7, 261-270 (1975).
10. D.B. Chisholm and D.L. Jones, *Experimental Mechanics*, 17, 7-13 (1977).
11. C. Atkinson, *International Journal of Engineering Science*, 10, 45-71 (1972).
12. C. Atkinson, *International Journal of Engineering Science*, 10, 127-136 (1972).
13. P. Tong, T.H.H. Pian, and S.J. Lasry, *International Journal for Numerical Methods in Engineering*, 7, 297-308 (1973).
14. S.P. Timoshenko and J.N. Goodier, *Theory of Elasticity*, Third Edition, McGraw-Hill, New York, (1970).
15. E.G. Coker and L.N.G. Filon, *A Treatise on Photo-Elasticity*, Cambridge University Press, London (1931).

APPENDIX

Following [14,15], the stresses relative to a cylindrical polar coordinate system ρ, θ , located at the center of the disk are*

$$\bar{\sigma}_{\rho\rho} = \frac{2P}{\pi a} \left[\frac{1}{2} - \frac{(1 - \frac{\rho}{a} \cos\theta) (\cos\theta - \frac{\rho}{a})^2}{(1 + \frac{\rho^2}{a^2} - 2 \frac{\rho}{a} \cos\theta)^2} - \frac{(1 + \frac{\rho}{a} \cos\theta) (\cos\theta + \frac{\rho}{a})^2}{(1 + \frac{\rho^2}{a^2} + 2 \frac{\rho}{a} \cos\theta)^2} \right]$$

$$\bar{\sigma}_{\theta\theta} = \frac{2P}{\pi a} \left[\frac{1}{2} - \frac{(1 - \frac{\rho}{a} \cos\theta) \sin^2\theta}{(1 + \frac{\rho^2}{a^2} - 2 \frac{\rho}{a} \cos\theta)^2} - \frac{(1 + \frac{\rho}{a} \cos\theta) \sin^2\theta}{(1 + \frac{\rho^2}{a^2} + 2 \frac{\rho}{a} \cos\theta)^2} \right] \quad (A.1)$$

$$\bar{\sigma}_{\rho\theta} = \frac{2P}{\pi a} \left[\frac{(1 - \frac{\rho}{a} \cos\theta) (\cos\theta - \frac{\rho}{a}) \sin\theta}{(1 + \frac{\rho^2}{a^2} - 2 \frac{\rho}{a} \cos\theta)^2} + \frac{(1 + \frac{\rho}{a} \cos\theta) (\cos\theta + \frac{\rho}{a}) \sin\theta}{(1 + \frac{\rho^2}{a^2} + 2 \frac{\rho}{a} \cos\theta)^2} \right]$$

These may be expanded in a power series in $\frac{\rho}{a}$ to give for $\bar{\sigma}_{\theta\theta}$ and $\bar{\sigma}_{\rho\theta}$

$$\bar{\sigma}_{\theta\theta} = \frac{P}{\pi a} \sum_{i=1}^n A_i(\theta) \left(\frac{\rho}{a}\right)^{2n-2} \quad (A.2)$$

$$\bar{\sigma}_{\rho\theta} = \frac{2P \sin 2\theta}{\pi a} \sum_{i=1}^n B_i(\theta) \left(\frac{\rho}{a}\right)^{2n-2}$$

where $A_1(\theta)$ to $A_5(\theta)$ and $B_1(\theta)$ to $B_5(\theta)$ are given in Table 2.

* These expressions are due to Prof. R.J. Erdlac, Dept. of Mechanical Engineering, University of Pittsburgh

LIST OF TABLES

Table 1: First Five Coefficients for Equation (3.1)

Table 2: First Five Angular Constants for Equation (3.1)

Table 3: Angles for Pure Mode II Behavior for Various Crack Lengths

TABLE 1

l/a	T_1	T_2	T_3	T_4	T_5
	S_1	S_2	S_3	S_4	S_5
0.1	1.014998	0.503597	0.376991	0.376991	0.314159
	1.009987	0.502341	0.376363	0.376363	0.314159
0.2	1.060049	0.514907	0.382430	0.383392	0.318086
	1.039864	0.509959	0.379956	0.380584	0.316245
0.3	1.135551	0.533477	0.391640	0.393835	0.325033
	1.089702	0.522272	0.386086	0.387518	0.320834
0.4	1.243134	0.559734	0.404603	0.408597	0.334831
	1.160796	0.539824	0.394822	0.397403	0.327411
0.5	1.387239	0.594892	0.421949	0.428353	0.347941
	1.257488	0.563966	0.406869	0.410966	0.336447
0.6	1.578258	0.642124	0.445387	0.454861	0.365559
	1.390654	0.597985	0.424037	0.430072	0.349219

TABLE 2

A_1	$1-4s^2$
A_2	$8s^2(1-4c^2)$
A_3	$-4s^2(3-36c^2+48c^4)$
A_4	$-16s^2(-1+24c^2-80c^4+64c^6)$
A_5	$-20s^2(1-40c^2+240c^4-448c^6+256c^8)$
B_1	1
B_2	$-5+8c^2$
B_3	$-3+8(1-2c^2)(2-3c^2)$
B_4	$3+16(1-2c^2) - 12(1-2c^2)^2 - 32(1-2c^2)^3$
B_5	$5-16(1-2c^2) - 60(1-2c^2)^2 + 32(1-2c^2)^3 + 80(1-2c^2)^4$

Note: $s = \sin\theta$; $c = \cos\theta$; $\cos 2\theta = 2c^2 - 1$

TABLE 3

ℓ/a	Eq(4.5)	Sanchez [8]	Awaji and Sato [7]
0.3	27.2	27.7	27.2
0.4	25.4	25.2	25.2
0.5	23.3	23.2	22.9
0.6	21.3	20.0	20.1

LIST OF FIGURES

- Figure 1: Geometry of the cracked Brazilian disk test.
- Figure 2: Stress distributions in the uncracked disk for $\frac{\rho}{a} = 0.6$.
- Figure 3: Stress distributions in the uncracked disk for $\frac{\rho}{a} = 0.3$.
- Figure 4: Stress intensity factors for $\frac{\ell}{a} = 0.5$
a) N_I , b) N_{II} .
- Figure 5: Finite element mesh for stress intensity factor determination.
- Figure 6: Stress intensity factors for the small crack approximation
a) N_I , b) N_{II} .
- Figure 7: Critical Mode I stress intensity factor for PMMA.
- Figure 8: Critical Mode II stress intensity factor for PMMA.

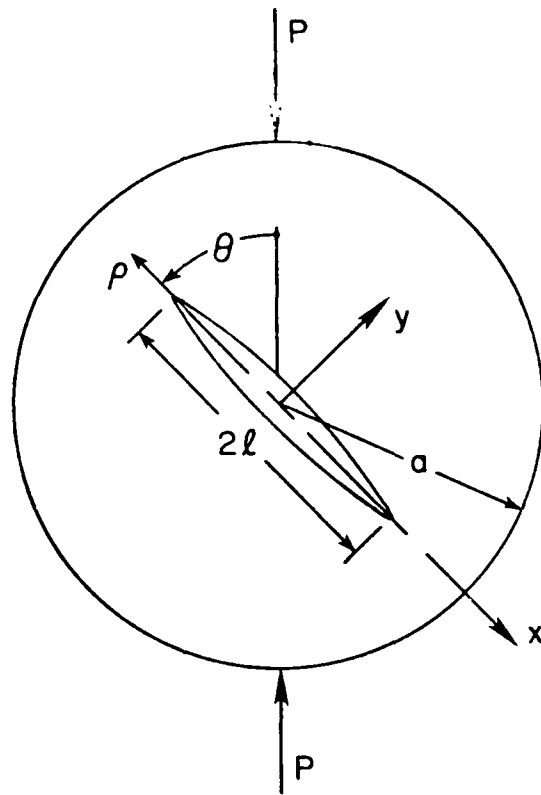


Figure 1

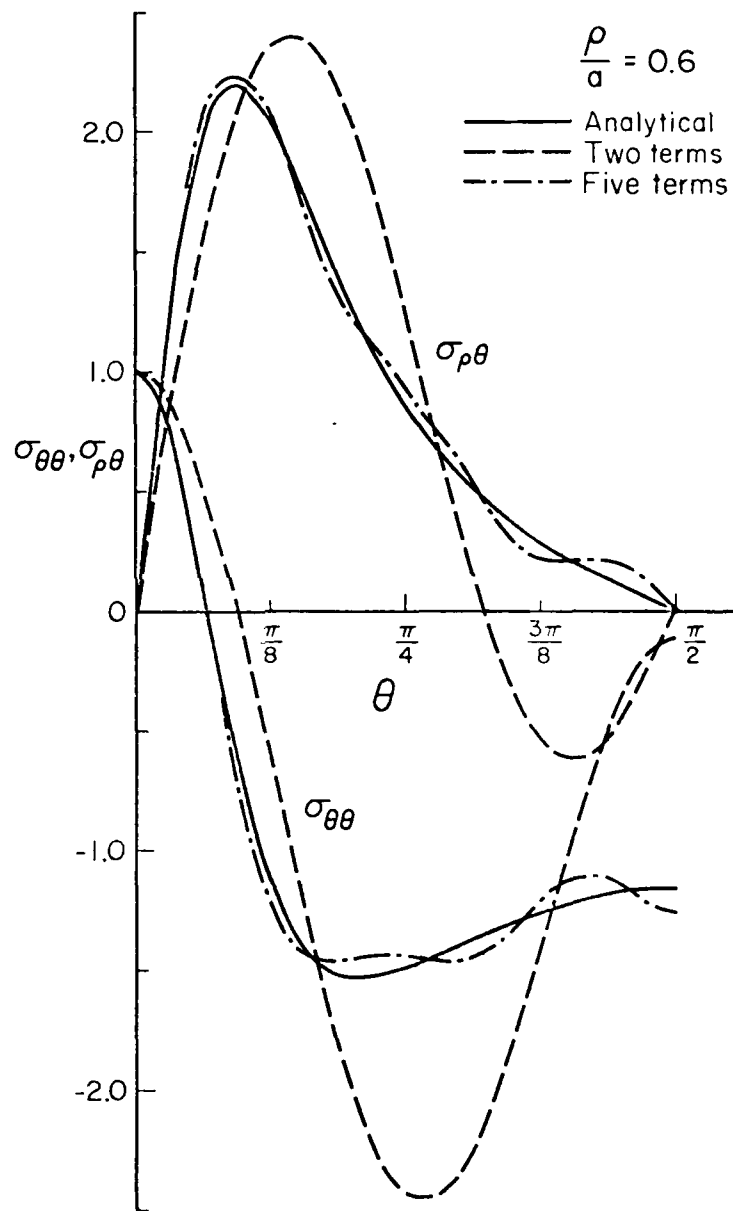


Figure 2

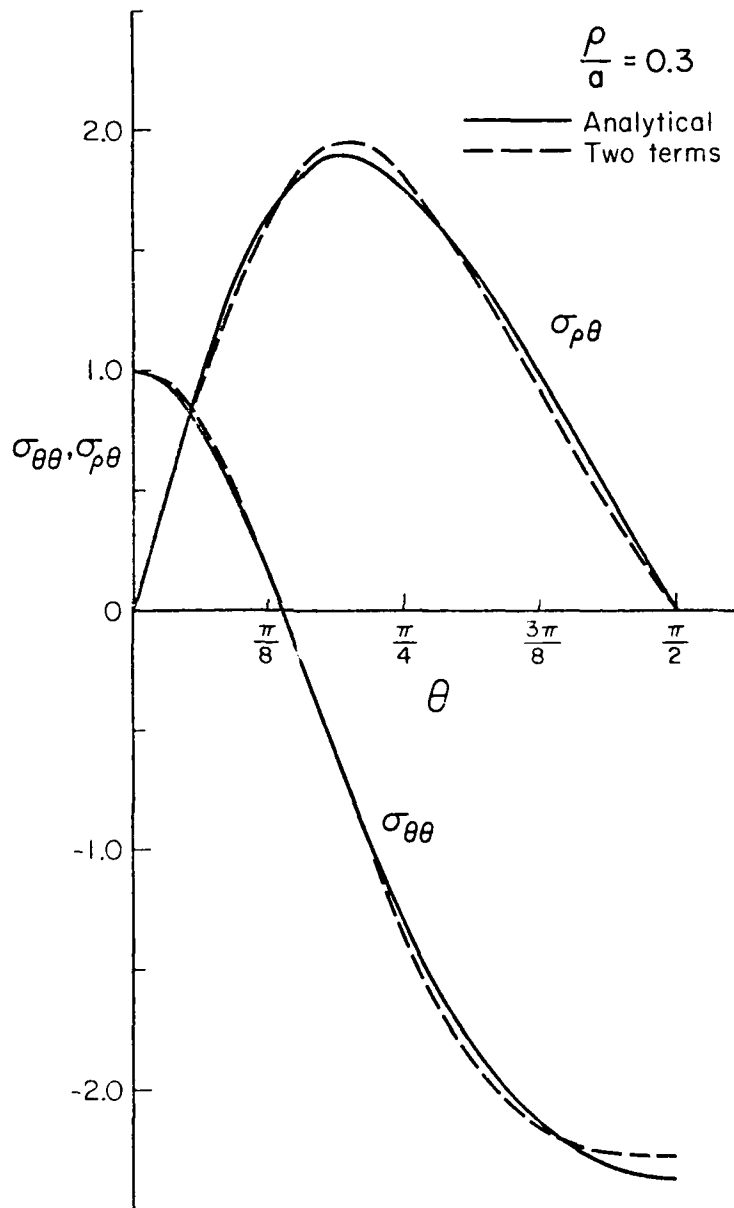


Figure 3

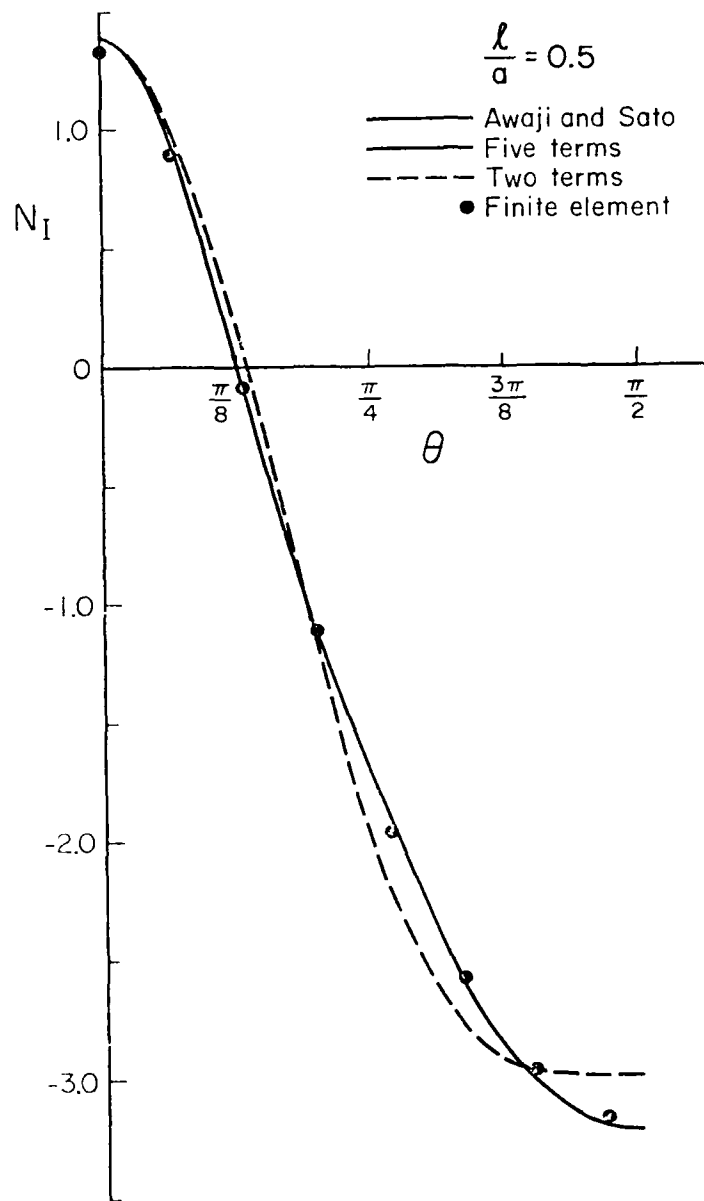


Figure 4a

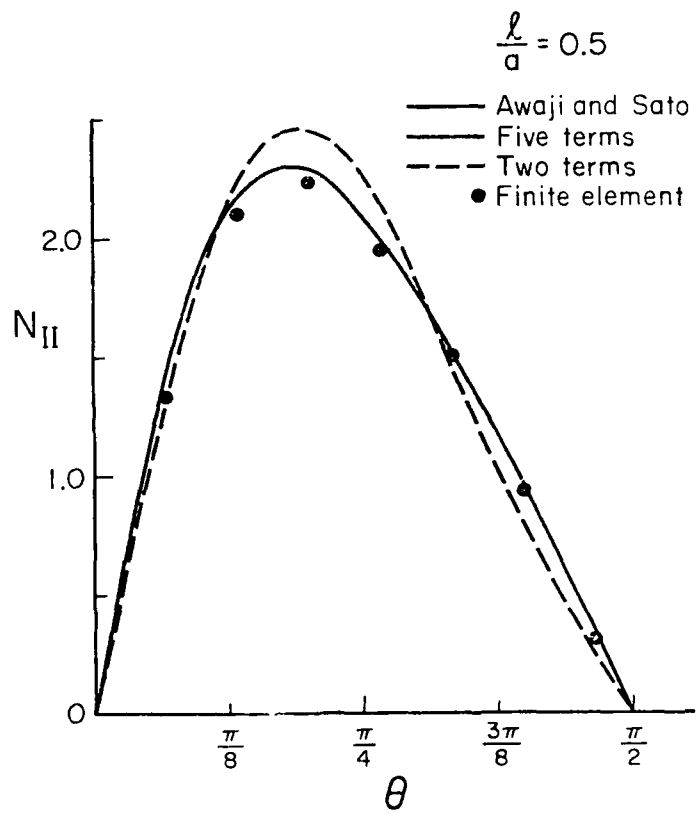


Figure 4b

r

r

IP

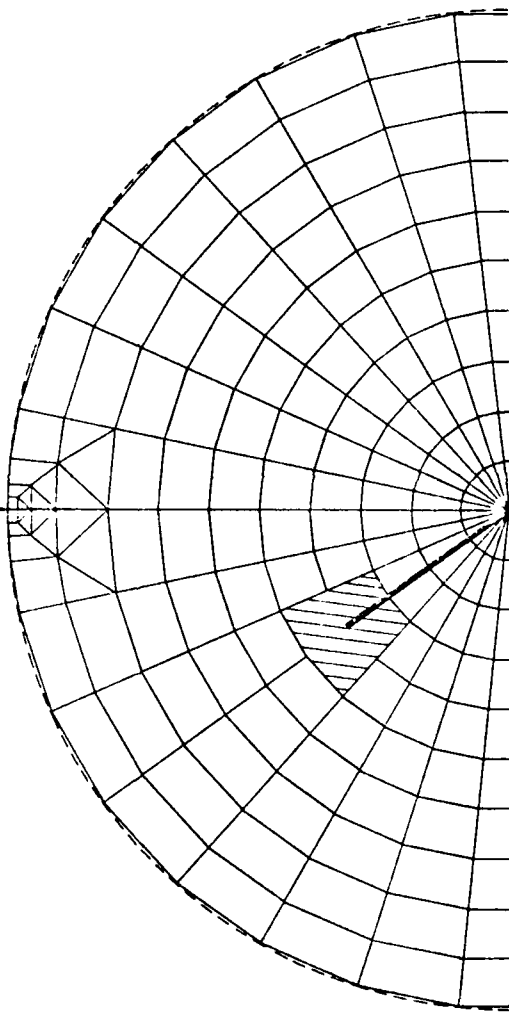


Figure 5

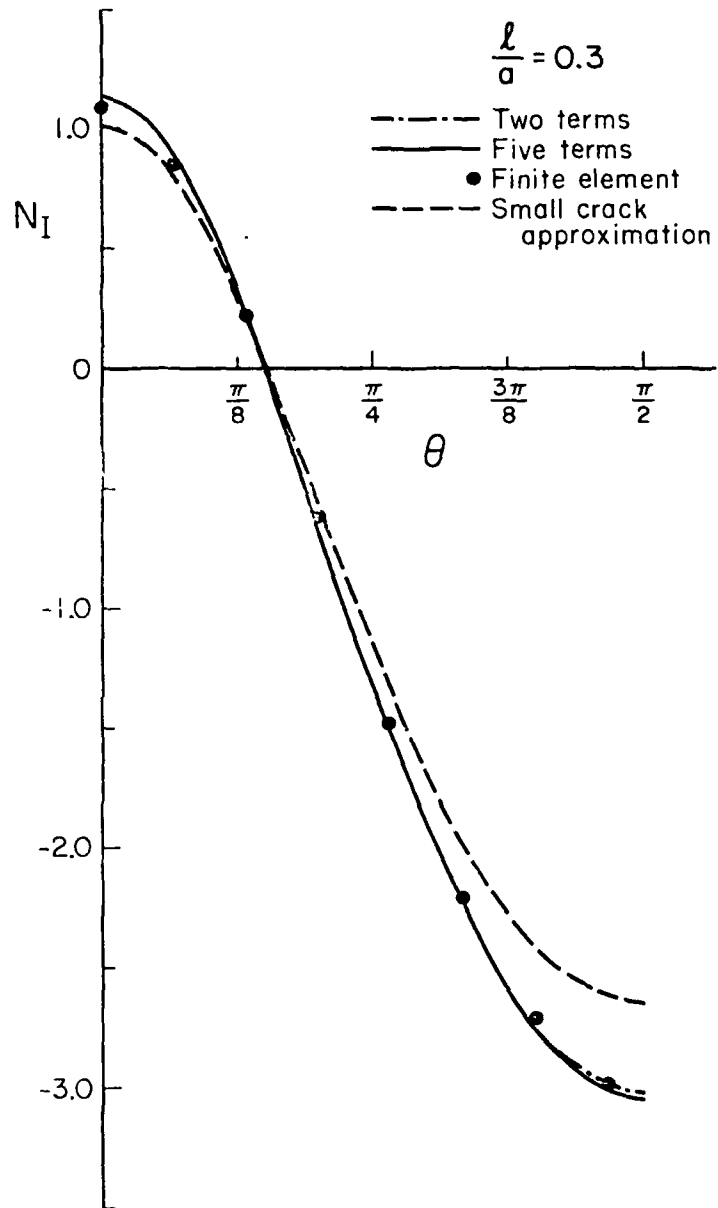


Figure 6a

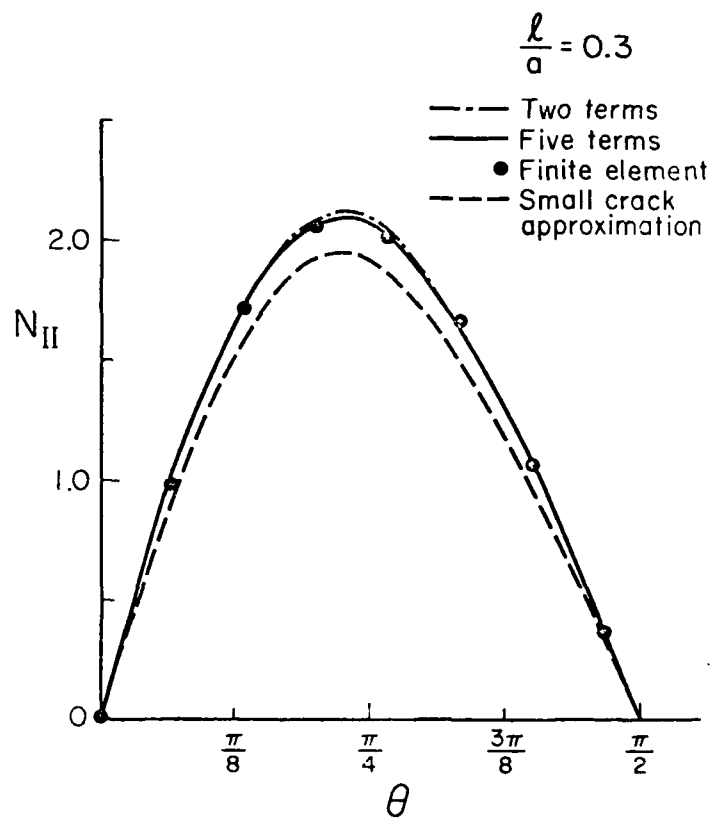


Figure 6b

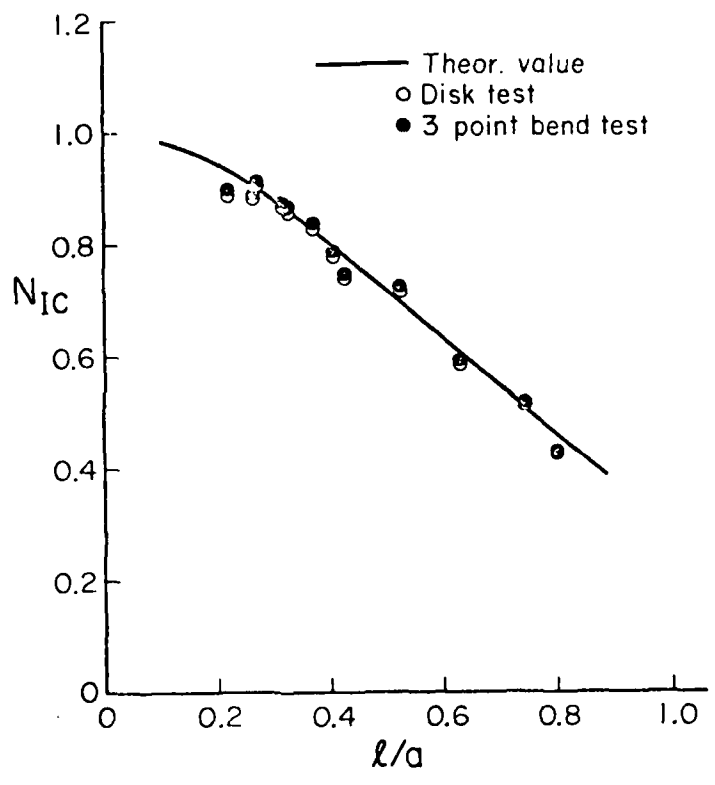


Figure 7

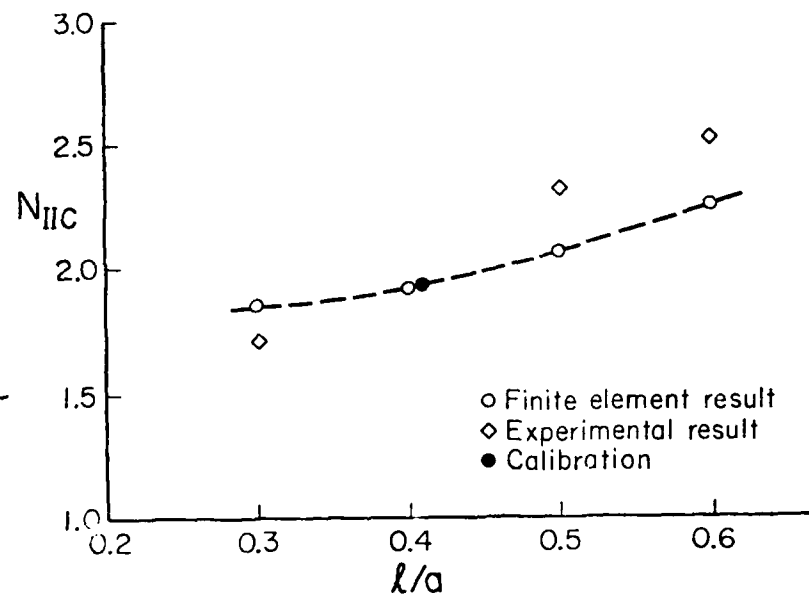


Figure 8

Appendix 4.5

Effects of Change in Crack Diameter
on Critical Load - Preliminary Study

Shan Somayaji
Department of Civil Engineering

Science of Fracture Research Project
AFOSR Contract #F49620-78-C-0101

School of Engineering
University of Pittsburgh
Pittsburgh, PA. 15261

EFFECTS OF CHANGE IN CRACK DIAMETER ON
CRITICAL LOAD-PRELIMINARY STUDY

By

Shan Somayaji

Introduction

Williams showed that from the viewpoint of continuum mechanics, and particularly the energy concept of fracture that adhesive and cohesive failure are similar (1). Experimental investigations such as blister tests and modified blister tests were carried out in the last decade, the results of which tend to prove the above hypotheses. Malyshev and Salganik (3) used a concentrated load to tear off a thin plate bonded flatwise to a rigid base and due to the axial symmetry, the crack was assumed to be penny-shaped. They tested a plexiglass-steel combination, loaded at the center to a point where the load stopped changing. The fracture energy so determined was found to be in close agreement with that determined by other types of tests. Jones and Williams used a method similar to that of Malyshev, et al., except that the central point load was replaced by a uniform pressure (2). They found that the pressure loading was simpler than the central load, and resulted in a smaller deflection. The test configuration consisted of a glass disk with a central hole bonded to a thin sheet of polyurethane rubber. Simultaneous measurements were made of the diameter of the unbonded area at that critical imposed pressure at which the unbond radius would increase.

In the Malyshev - Salganik investigations the debond radius was assumed to occur at a critical load but, with neutral stability, to increase as the load remained constant. Substantial test data are not available to verify this assumption and it is probable that the effects of non-linearity in material properties and other sources of energy dissipation may affect the critical load to induce debonding and whether it would then remain constant or not. The objective of this study is to make a preliminary estimate of such effects upon the critical load and on the adhesive fracture energy. An experimental model similar to the one adopted by Malyshev, et al (3) was therefore used to test a plexiglass-steel combination. The model was equipped with a dial-gage apparatus to measure the central deflections. A number of load-deflection diagrams were plotted for each specimen at different initial diameters from which a preliminary estimation of variation in the critical load was made. The details of the test procedure and test results are given in this report.

Test Details

The specimen details and the test set-up are shown in Fig. 1. The specimens were made up of 1/8 in. and 1/16 in. plexiglass plates of 2.25 to 2.4 in. diameter, bonded to 3 inch diameter steel plates using "Epoxy Cement" manufactured by G. C. Electronics, Rockford, Il. The load was applied to the plexiglass plate by a plunger passing through a central hole in the steel plate as shown in Fig. 1. A small area at the center of the specimen, of about 0.5 in. diameter, was covered with a circular piece of scotch tape to prevent clogging the central hole during the initial bonding of the specimen. Moreover, this area at the center of the specimen where the steel and plexiglass are unbonded, acts like a crack initiator. Proper precautions were taken such as

cleaning the surfaces with alcohol, uniform mixing of the epoxy cement, constant curing time, etc. The manufacturer's suggestions were followed for the mixing operation. The specimens were lab-cured for 24 hours after which they were tested using a Baldwin Universal Testing machine.

The loads and the central deflections were recorded during the test. A special dial-gage apparatus, shown in Fig. 2, was used to record the central (under the load) deflection. (The recorded readings were converted to deflection readings using the proportionality constants: deflection-gage readings \times 5). For a few specimens the loads were applied continuously until complete debonding occurred but for the majority of the specimens a number of load-deflection-crack diameter readings were taken prior to complete debonding. To accomplish this the test was stopped and the specimen was unloaded when the load remained steady or started to decrease. Indication of a decrease in the loading rate, (or when the load seemed to remain steady) was observed. The diameter of the actual debonded area as seen through the plexiglass plate then was measured using a scale. The specimen was set under the plunger again and the loading process was repeated. The specimen was again unloaded and the diameter of debonded area was recorded. This procedure of loading, unloading, and measurement of the crack extension was repeated a number of times prior to complete debonding. Tabulations of the load-deflection-crack diameter readings for most of the specimens that were tested in the program and the load-deflection curves are in Ref. 4. For the few specimens for which the loads were applied continuously until the final break-off, typical load-deflection diagrams are as shown in Fig. 3. The loads could be seen to increase linearly to a peak load, followed by a sudden drop and a gradual increase combined with an increase in deflections. Although no conclusive statements can be drawn at this stage due to the limited number of tests performed, there is an

indication that the extent of the load-drop may be influenced by the thickness of the specimen. It was also found that the variations in the initial peak-load between specimens of the same thicknesses are small.

Fig. 4 shows typical load-deflection-crack diameter diagrams. The initial and final crack diameters are indicated on each load-deflection diagram, the details of which are given in Ref. 4. The test results indicated that for most of the specimens, the diameter of the cracked area increased with increase in load, although this increase (in load) was quite small for a few specimens. Due to the preliminary nature of the investigation no solid conclusions can be drawn at this stage but it is felt that the shape of the load deflection diagram during the crack extension stage is dependent on the specimen thickness. For most specimens of 1/16 in. thickness the final break-off occurred at a load smaller than the initial-diameter peak load, whereas, for specimens of 1/8 in. thickness, the final break-off load was not much different from the initial-diameter peak load.

Fracture Energy Determination

Malyshev, et al (3) determined the adhesive fracture energy for centrally loaded bonded specimens as follows:

For a circular plate loaded at the center, the central deflection w is given by

$$W = \frac{Pa^2}{16 \pi D} \quad (1)$$

where P is the central load, a is the initial radius and D is given by:

$$D = \frac{Eh^3}{12(1 - \nu^2)} \quad (2)$$

where E is the modulus of elasticity, h is the plate thickness and ν is Poisson's ratio.

For an increase in crack radius of amount da , the area of debond extension is approximately equal to $(2 \pi a) da$. Using the energy balance fracture criteria

$$(2 \pi a da) \gamma_a = dU \quad (3)$$

where γ_a is the specific adhesive fracture energy and U is the elastic strain energy.

But, U is given by one half the applied load times the equilibrium displacement, or

$$U = \frac{1}{2} \left(\frac{P^2 a^2}{16 \pi D} \right) \quad (4)$$

from which dU can be calculated and inserted into (3) to give

$$\gamma_a = \frac{P^2}{32 \pi^2 D} \quad (5)$$

(Note that the absence of the radius in (5) indicates neutral stability.)

From this preliminary investigation, the critical loads were found to be in the range of 80 to 120 lbs for specimens of 1/16 in. thickness and 90 to 180 lbs for specimens of 1/8 in. thickness. This shows a large scatter in the test results for specimens of the same series, of the order of about 100 percent. But for a given specimen the average increase in the critical load with increase in crack diameter of about 100% (0.50 in. - 1.0 in.) was found to be about 16.5 percent. This, when compared with the above values of the experimental scatter in the critical load, can be regarded as small.

Since the adhesive fracture energy is proportional to the square of the critical load, a small change in the critical load can strongly affect its predicted value. But considering the fact that even specimens of the same thickness failed at critical loads that were distinctively different, it may be justified to neglect the effects of the

increase in critical load (with increase in initial crack diameter) in fracture energy determination. However, this is not intended to down-play the role of the critical load in fracture energy determination which is obvious from Eq. 5.

A revised method which makes use of direct measurements of the strain energy for each increase in crack diameter is suggested in Ref. 4. Due to the preliminary nature of this investigation, no conclusive statements can be drawn using that method at this stage. Further research is suggested.

Discussions and Conclusions

The Malyshev-Salganik model to determine the specific adhesive fracture energy has been re-examined and verified for a plexiglass to steel bond.

The preliminary test results have suggested that there may be a load with change in crack diameter which is not predicted by the elementary strength of materials analysis. Further investigations are recommended to determine the effects of plate thickness and plate diameter on the adhesive fracture energy and load-deflection diagrams. As an alternative, direct measurement of fracture energy from the load-deflection diagrams is also recommended.

AD-A093 417

PITTSBURGH UNIV PA SCHOOL OF ENGINEERING
SCIENCE OF FRACTURE, (U)

F/6 20/11

UNCLASSIFIED

OCT 80 M L WILLIAMS, C C YATES
SETEC-SF-80-048

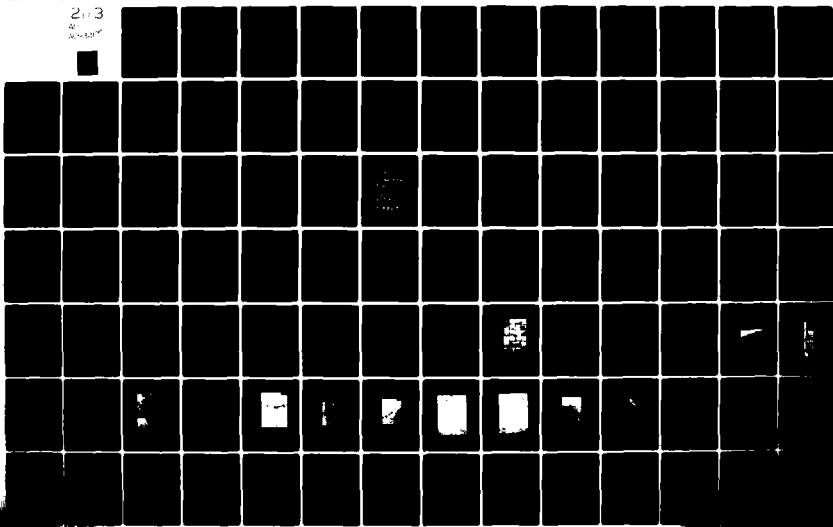
AFOSR-TR-80-1322

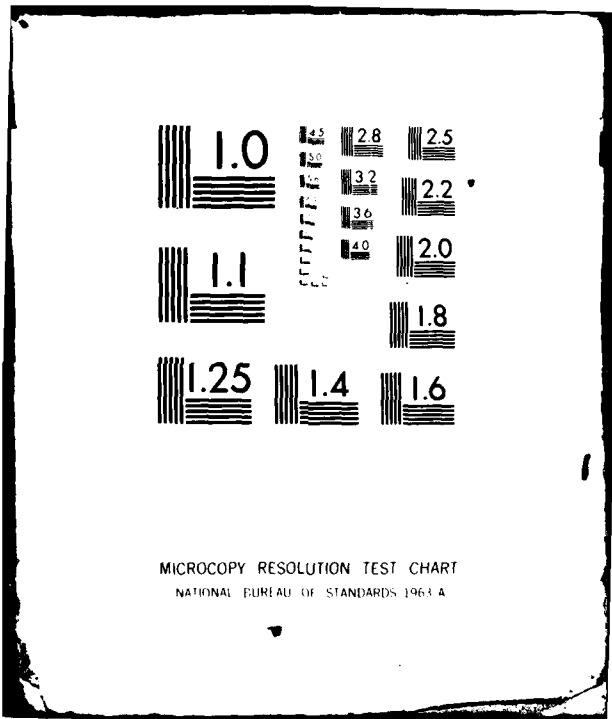
F49620-78-C-0101
NL

213

41

20/11





MICROCOPY RESOLUTION TEST CHART
NATIONAL BUREAU OF STANDARDS 1963 A

REFERENCES

1. Williams, M.L., J. of App. Polymer Sci., 13, 29, 1969.
2. Jones, W.B. and Williams, M.L., UTEC DO 68-019, University of Utah, Feb. 1968.
3. Maylshev, B.M. and Salganik, R. L., Int. J. of Fracture Mech., 1, 114.
4. Adhesive Fracture Energy - Preliminary Study using Blister tests - SETEC SF-047 80 - Technical Report University of Pittsburgh,

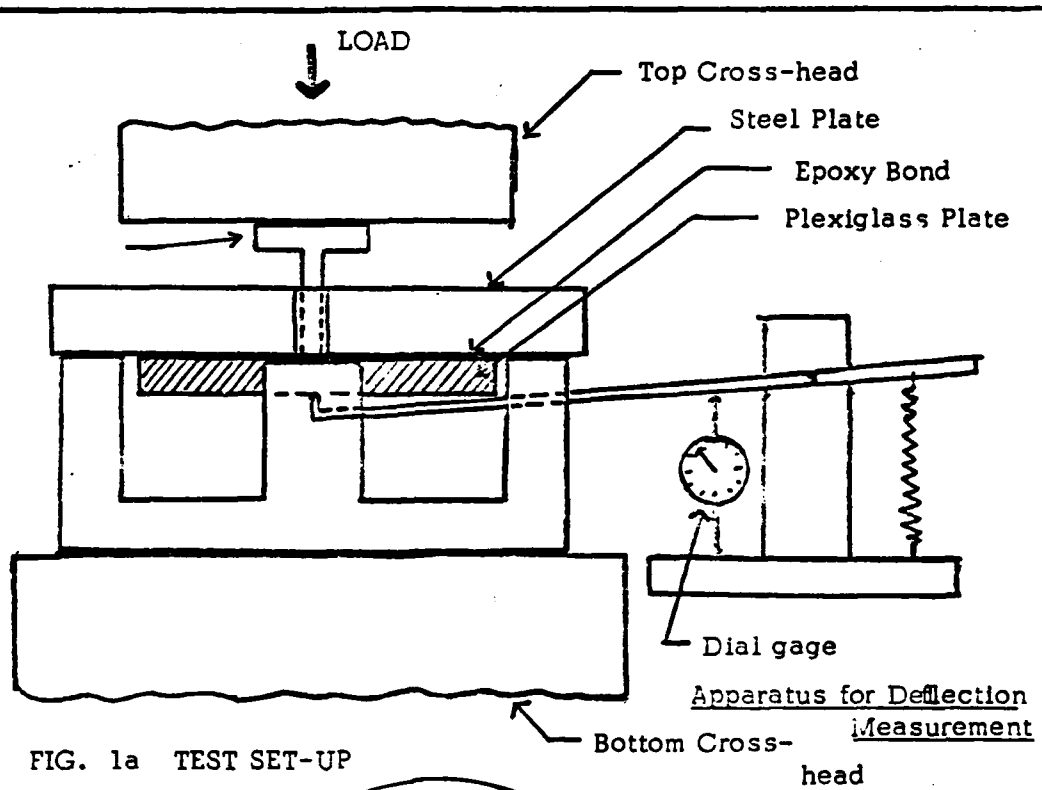


FIG. 1a TEST SET-UP

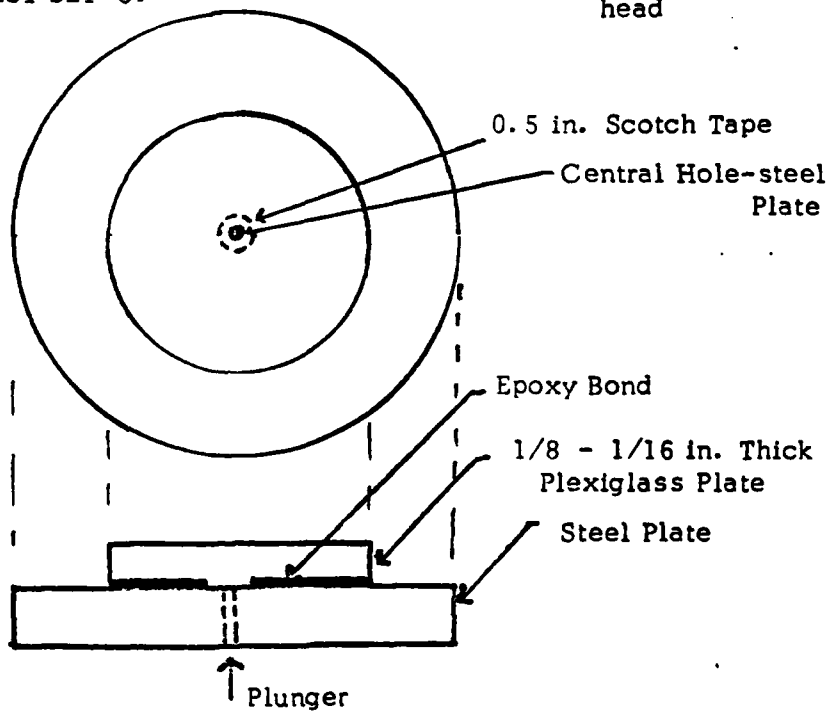


FIG. 1b SPECIMEN DETAILS

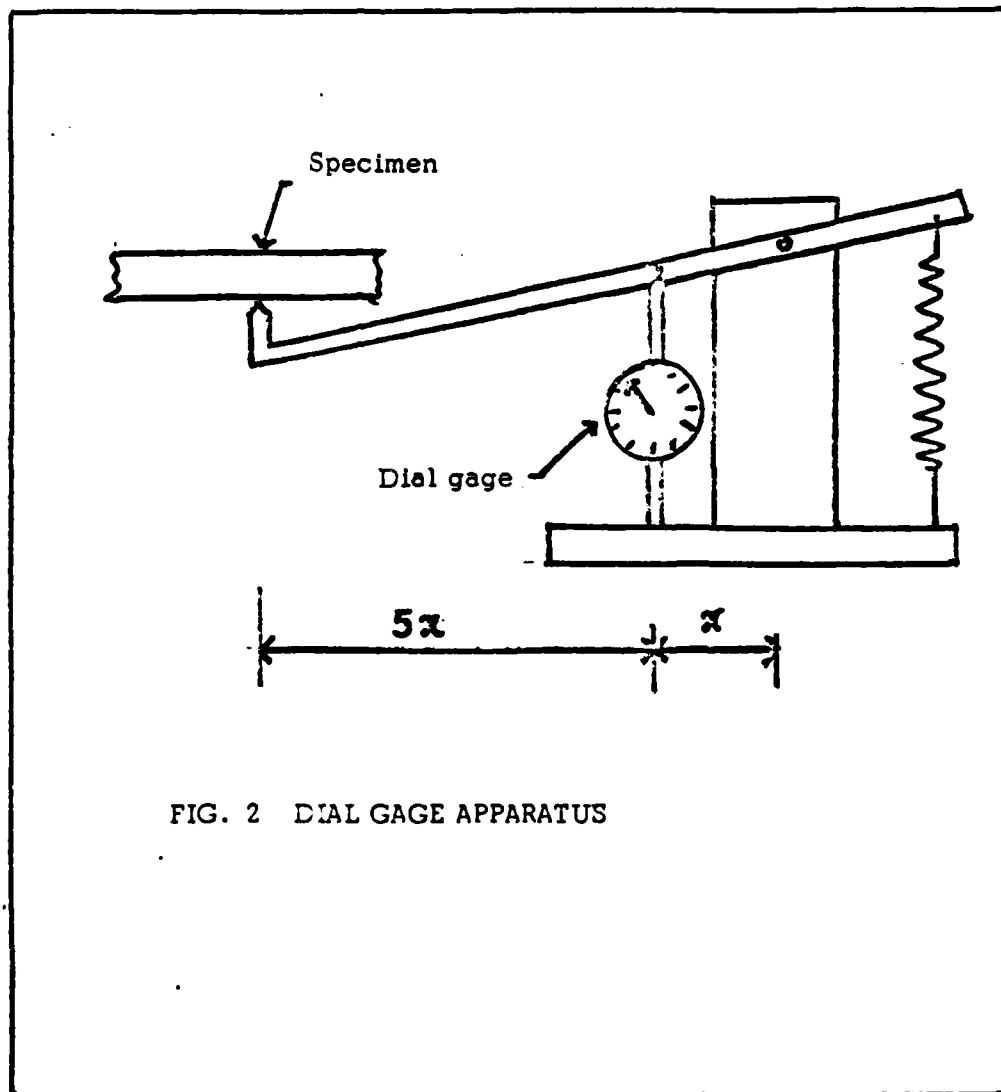


FIG. 2 DIAL GAGE APPARATUS

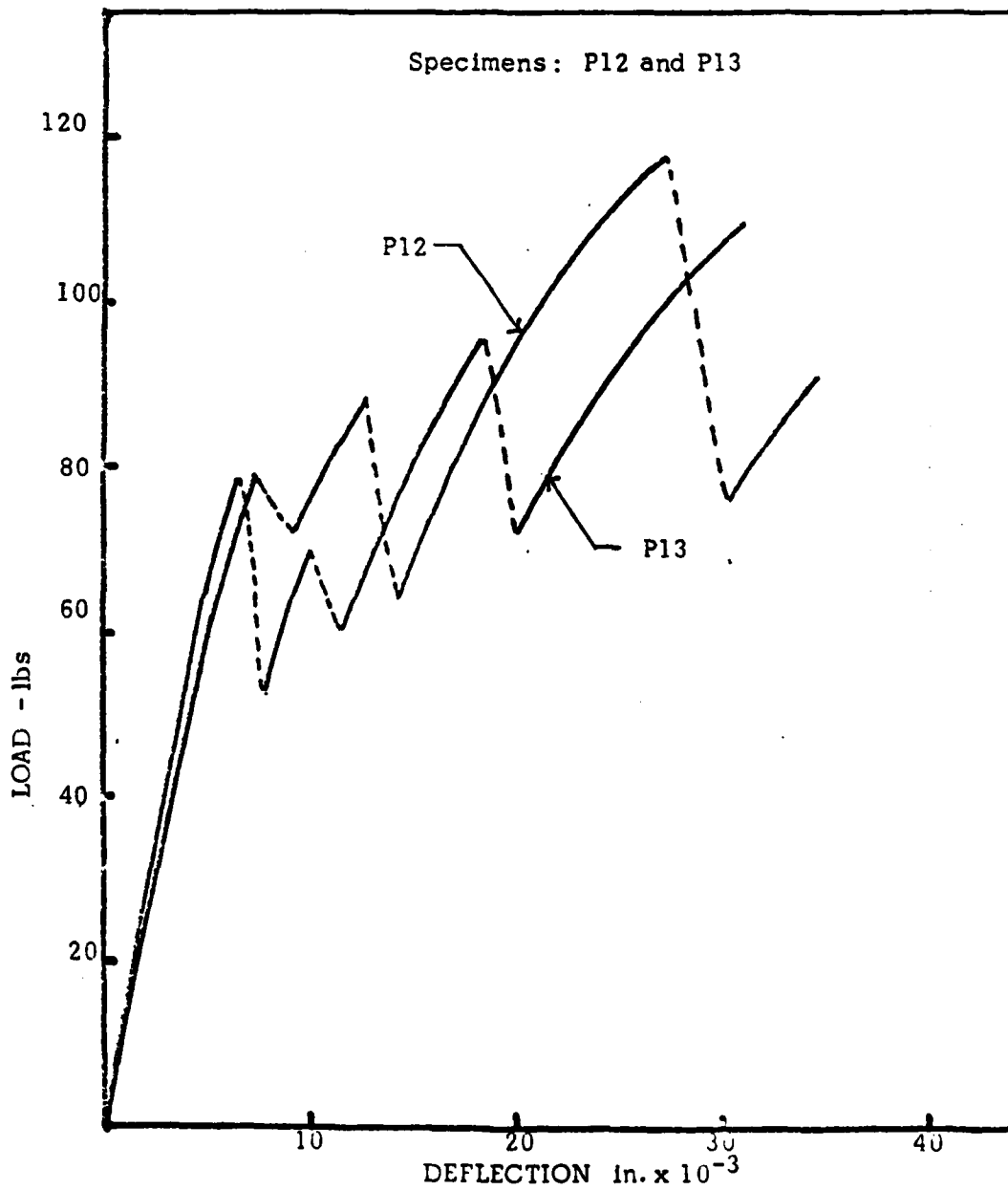


FIG. 3 Typical Load-Deflection Diagrams

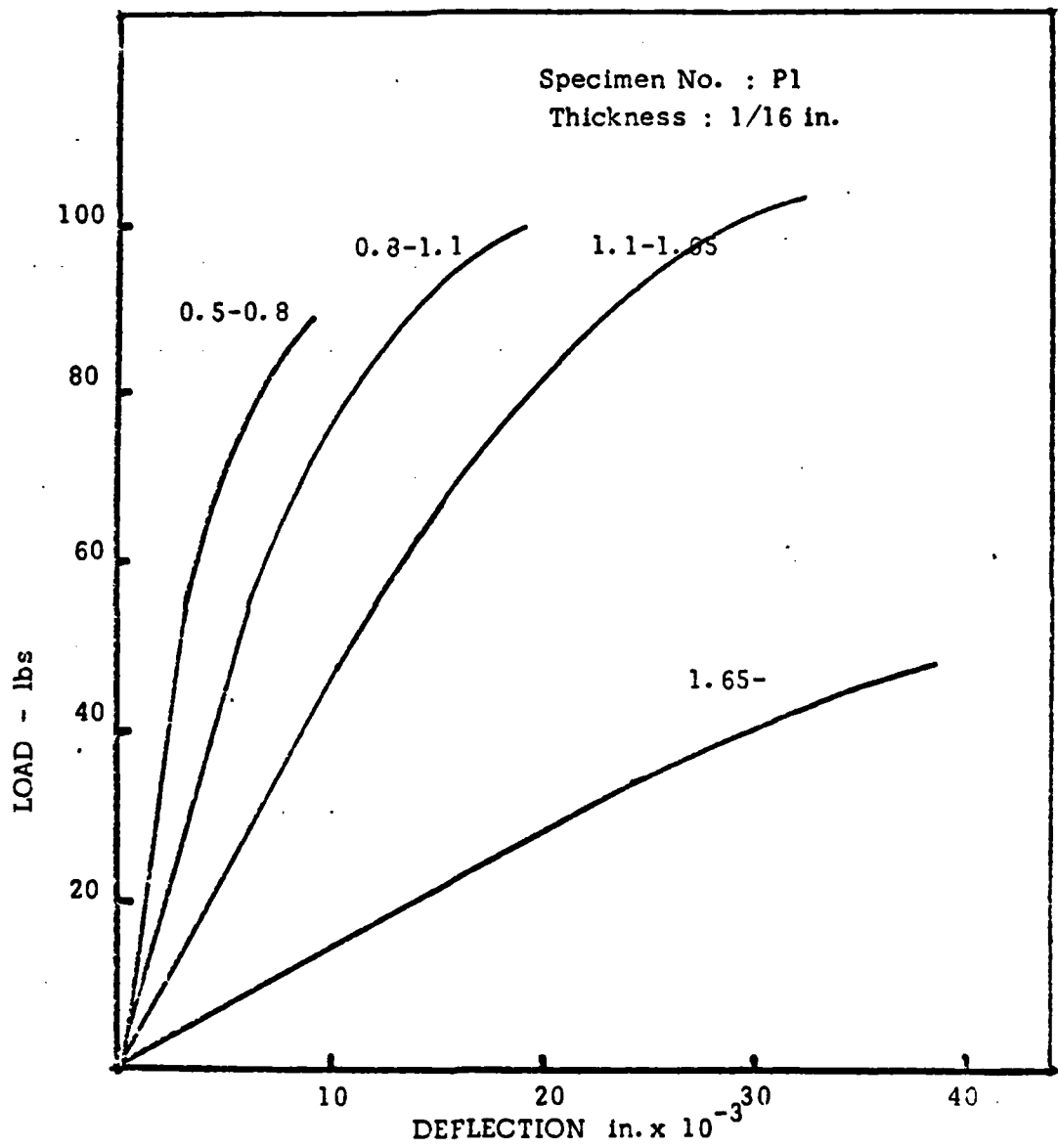


FIG. 4 Typical Load-Deflection -Crack Diameter Diagram

SETEC DO 80-057
September, 1980

Appendix 4.6

**Bibliographic Overview of Composite Materials
with Special Focus upon Recent Publications
on Fracture**

**M. C. Williams
Research Associate**

**Science of Fracture Research Project
AGOSR Contract #F49620-78-C-0101**

**School of Engineering
University of Pittsburgh
Pittsburgh, PA. 15261**

TABLE OF CONTENTS*

	Page **
1.0 Background	1
1.1 Background General References	4
2.0 Fatigue Strength	5
2.1 Fatigue Strength References	9
3.0 Fracture Strength	10
3.1 Fracture Strength References	20
4.0 Fracture Mechanics	25
4.1 Fracture Mechanics References	26

* This abridged version only includes the general references.
See the basic report (SETEC DO 80-057) for detail included
in Sections 2-4.

** Page numbers refer to basic report.

**A Bibliographic Overview of Composite Materials with Special
Focus upon Recent Publication on Fracture**

1.0 Background

A retrospective search was made for survey or research articles (reports and journals) covering a broad aspect of the problem rather than a specific area. There have not been a great many. In fact much of the early material appeared as chapters in books.

In 1965 the National Materials Advisory Board (NMAB) published a "Report of the Ad Hoc Committee on Interface Problems in Fibrous Composites" (1) dealing with fiber surface, the process of composite formation, retention of properties in service, and the interface during composite failure. The objective was "to display potentially critical facets of the situation in order to identify areas in which additional research is needed . . .". A second report came from NMAB in 1965 entitled "Composites" (2). The purpose of this study was to examine research and development problems which limited the further advance of composites technology and included recommendations for research and development efforts. In 1974 the NMAB published "Metal-Matrix Composites: Status and Prospects" (3), a report of the Ad Hoc Committee on Metal-Matrix Composites. The stated goal of this study was to determine the role of metal-matrix composites particularly in DOD applications. Specific subjects covered were: the state-of-the-art; the advantages and disadvantages compared to monolithic-wrought materials and resin-matrix composites; the potential in DOD, NASA, and commercial applications; fabrication capability and the status of the data base; cost projections; previous service experience and current

impediments and requirements for expediting wider use of metal-matrix composites.

Also in 1974 an article appeared in the AIAA JOURNAL entitled "Composite Material Mechanics: Structural Mechanics" by C. W. Bert and P. H. Francis (4). The purpose of that survey was to bring together and review some of the principal contributions in structural mechanics to the field of composite materials. Emphasis was given to the macro-mechanical structural analysis of various structural elements. In the meantime, in 1972, Fracture, VII appeared with the chapter on "Fracture Mechanics of Composites" by H. T. Corten (5).

Continuing the concern for metal matrix composites applications to DOD requirements, the Institute for Defense Analyses Science and Technology Division published the proceedings of the First MMC Workshop held 9-10 July 1975, "Technological Development of Metal Matrix Composites for DOD Application Requirements" (6). The purpose of the workshop was to assess the technology of metal matrix composites for DOD application requirements and included applications, loads and environments, analyses and design and manufacturing and fabrication. Also in 1975 Illinois Institute of Technology prepared a report on "Fracture Toughness of Fiber Composite Materials" (7) for the Air Force Office of Scientific Research. Fracture toughness test methods were evaluated and fracture toughness parameters measured for random fiber composites having epoxy resin matrices.

"Fracture Mechanics of Composite Materials" by C. K. H. Dharan (8) published in the Journal of Engineering Materials and Technology in July 1978 attempted to present a survey of the field in

its current state and to demonstrate the approach taken by various investigators. "Research Priorities for Advanced Fibrous Composites" a report by K. J. Baumann and J. L. Swedlow (9) was sponsored by NASA/Lewis and recommends research priorities in advance fibrous composites for the aerospace industry. A state-of-the-art review is presented with service experience and technical literature. The bibliography is very long and very complete and precludes the need to duplicate the effort. It is also very current and probably includes the majority of the composites literature through 1979 featuring in particular the Journal of Composite Materials. The Journal of Composite Materials has been reviewed for 1980 and the relevant articles have been added in the attached bibliography.

Inasmuch as the primary immediate purpose of this effort has been to examine the fracture of composite materials, a selected bibliography of relevant citations is attached. The more general problem of adhesive fracture can of course be viewed as a fracture in composite media and for this reason six basic historical references to the bimaterial problem have been included in the collection of special fracture references. References have also been included to the related Fiber Pull-Out Problem and the Interfacial Crack Problem bibliographies prepared for the last annual report (SETEC SF 79-5, October, 1979).

1.1 Background General References

- (1) National Materials Advisory Board. "Report of the Ad Hoc Committee on Interface Problems in Fibrous Composites". MAB-214-M (1965).
- (2) National Materials Advisory Board. "Composites". MAB-215-M (1965).
- (3) National Materials Advisory Board. "Metal-Matrix Composites: Status and Prospects". NMAB 313 (December 1974).
- (4) C. W. Bert and P. H. Francis. "Composite Material Mechanics: Structural Mechanics". AIAA Journal, 12, 9 (September 1974) 1173-1186.
- (5) H. T. Corten in Fracture, VII, H. Liebowitz, Ed. . Academic Press (1972) 675.
- (6) Institute for Defense Analyses Science and Technology Division. "Technological Development of Metal-Matrix Composites for DOD Application Requirements", Paper P-114* (September 1975).
- (7) L. J. Broutman and S. K. Gaggar. "Fracture Toughness of Fiber Composite Materials". Illinois Institute of Technology. AFOSR TR-75-1393 (February 1975).
- (8) C. K. H. Dharan. "Fracture Mechanics of Composite Materials". Journal of Engineering Materials and Technology, 100 (1978) 233.
- (9) K. J. Baumann and J. L. Swedlow. "Research Priorities for Advanced Composites", Carnegie-Mellon University SM 79-15A (July 1979).

SETEC # 80-039
August 1980

Appendix 4.7

Current Status and Future Prospects of
Micromechanical Failure Theories for Fibrous Composites

S. B. Batdorf
Visiting Professor, University of Pittsburgh
School of Engineering and Applied Science
UCLA, Los Angeles, 90024

Prepared as a Contribution to the
Science of Fracture Research Project
AF Contract #F49620-78-C-0101

School of Engineering
University of Pittsburgh
Pittsburgh, PA 15261

FOREWORD

Each of the Services within the Department of Defense has established agencies having the responsibility of advancing the state of the art in those technologies having military value. Allocations of funds to specific R & D programs are made in accordance with formally adopted "requirements" with due consideration to cost-benefit ratio, technical feasibility, etc.

Before research in a given area starts, technical feasibility is often quite uncertain, but is viewed optimistically if the potential benefits are large. If after a number of years of effort rate of progress is judged to be slackening as a result of the law of diminishing returns, the priority of that field of endeavor is lowered, and the corresponding objective may even be dropped as a military requirement. In that case, even if a technical breakthrough is subsequently discovered, no funds to pursue it are available because no allocation was made in the budget. When this happens the judgment that future progress will be of limited value becomes a self-fulfilling prophecy.

A case in point may be the development of a micromechanical theory for the tensile strength of fibrous composites. During the 1960's and early 70's research of this type was extensively supported by the three services (especially the Air Force), NASA, and the Atomic Energy Commission. In spite of this a rational failure criterion analogous to Griffith crack instability theory failed to emerge. Today funding in this field is at a very low ebb. Even though a breakthrough appears to be on the horizon, it may not be pursued because it was not anticipated and therefore is not budgeted.

According to an ancient Chinese proverb "It is better to light a candle than curse the darkness". Translated, those who perceive an unsatisfactory situation have a duty to call it to the attention of others in a position to do something about it. This thought was the motivation of the following paper.

INTRODUCTION

Structural efficiency was for many years limited by an empirical law which states that the strength-to-weight ratios of all of the common structural materials tend to be roughly the same. This was also true of stiffness-to-weight ratios. A few decades ago it began to be recognized that certain fibers, such as glass, boron, kevlar, and carbon or graphite, could be prepared with many times the specific strength or specific stiffness values attainable in bulk materials. As a result, a very substantial development effort was undertaken, especially within the military services, to capitalize on these properties.

In spite of the extensive use now being made of fibrous composites there is a widespread feeling that the current applications fall far short of the ultimate potential of such materials and are not commensurate with the very large development effort carried out during the last twenty years. There are a number of factors contributing to this unfortunate situation. Among them are practical matters such as joining difficulties and reduced reliability sometimes resulting from manufacturing imperfections. But there can be little doubt that one of the most important causes is lack of confidence, due to the fact that the fundamentals of damage accumulation in fibrous composites during the loading process and the mechanics of ultimate failure are as yet poorly understood.

Since the basic purpose of high performance composites is to capitalize on the extraordinary tensile properties of the fiber employed, the first and most important task in rectifying this deficiency is to achieve an understanding of the tensile strength of unidirectionally reinforced composites. The severity of the shortcomings of presently available theory are probably known only to a few specialists in this field. Those required to make strength calculations try to compensate for a lack of basic understanding by making large empirical

corrections to the theory and using substantial safety margins.

The next section will briefly review and critique published theories for the tensile strength of unidirectionally reinforced fibrous composites. The succeeding section will outline a new theoretical approach which offers a prospect of eliminating empiricism and providing a sound basis for greatly improved design estimates of composite strength.

REVIEW OF PREVIOUS WORK

The theory for damage accumulation and fracture of a "loose bundle", or collection of independent fibers of equal length loaded in parallel, was worked out decades ago by Daniels and Coleman (1-2). The subject is by now quite well understood. Such is not the case, however, with fibrous composites. In many composites a relatively soft matrix is used to bind very strong fibers together. The matrix does not appreciably contribute directly to the tensile strength, but it contributes indirectly by transferring stress between fibers. When a fiber breaks in such a composite its load is transferred to neighboring fibers by the matrix. But the stress tends to equalize with distance from the cross section at which the break occurred, and returns to normal in a distance 0.5δ on each side of the break. This distance is variously referred to as "ineffective length" and "stress transfer length". The net effect is to localize the damage.

Many papers containing approximate theoretical solutions for the tensile strength of such a composite have been published. Harter (3) has reviewed the work of the major contributors to this field through 1976. In the present paper the treatment of prior work will be limited to a very brief discussion of a representative sample of these contributions. Suffice it to say at this point that for nearly two decades theoretical analyses have generally been based on a model which regards a composite as a chain of very short bundles which we shall refer to as "minibundles".

In 1962 Gucer and Gurland (4) proposed a model for a particulate composite consisting of many slices connected in series. Rosen (5) adapted this approach for fibrous composites. Each slice became a minibundle of fibers. The strength of each minibundle was computed by loose bundle theory, and the failure of the chain of minibundles, each having the length δ , was then estimated using weakest link theory.

Using the geometrical model of Rosen, Zweben (6) investigated the influence of load concentrations caused by fiber breaks. Zweben and Rosen (7) then discussed crack growth in 3-D unidirectional composites on the basis of the chain of minibundles model, taking into account stress concentrations in nearest fibers, and looking for a Griffith-type instability. Perhaps as a result of the attempt to estimate probabilities for all possible events, the analysis became too complicated to carry through for 3-D composites. They did, however, analyze the 2-D case (single ply tape) in some detail, working out the expected number of multiple breaks of various orders as a function of applied stress. Nevertheless, they did not succeed in establishing a theoretically based failure criterion, stating that "one can only say that the expected failure stress will be bounded by the expected stress at the first break, σ_1 , and the expected stress at which N adjacent fibers will be broken, σ_n ". As a practical matter, they proposed using the occurrence of the first multiple break as a failure criterion.

An improvement in regard to approaching physical reality is achieved by taking into account the fact that in many composites the stress gradient in the broken fiber get so high that the matrix is unable to supply the shear stress needed to establish equilibrium. This appears to have been done first by Scop and Argon (8). As a result either the matrix yields or debonding between fiber and matrix sets in. In either event, δ increases beyond the elastic transfer length and becomes a function of applied stress. A minibundle of fibers of length δ becomes weaker as δ increases due to the Weibull size effect, and failure occurs when the estimated bundle failure stress for length δ is equal to the stress required to produce that value of δ . It has been found that an empirically-based several-fold increase in δ must be assumed in order to bring theory and experiment into acceptable agreement in the case of carbon-carbon (9).

Harlow and Phoenix are placing the problem of composite damage and failure on a more rigorous mathematical foundation than has theretofore been available. Their approach is based on the chain-of-minibundles model and seeks to establish a converging sequence of upper bounds to composite strength. Some appreciation of the analytical complexity that is involved in a rigorous treatment can be obtained by noting that an investigation resulting in five papers extending over a three year period (10-14) has been required to solve the problem of a purely elastic single ply tape, using a highly simplified local load sharing rule. It is the opinion of the present writer that while this approach is much too cumbersome for application to most problems of practical interest, it is valuable as a standard to help assess the accuracy of approximate techniques capable of a wider range of application. Such a use will be made in the next section.

In spite of the fact that almost all micromechanical theories of composite tensile strength in the last decade and a half have been based on the chain-of-minibundles approach there are some serious deficiencies which are intrinsic to the chain-of-bundles model itself. One is that the use of such a model requires the analyst to use the same "ineffective" length for a multiple fiber break, regardless of order, as for a single isolated break. This assumption is particularly bad when debonding occurs, since the higher the multiplicity of the break, the higher the stress concentration factor, and therefore the lower the debonding threshold. Another deficiency is that interaction between cracks (multiple fiber breaks) is assumed to occur only if the cracks are in the same link of the chain. Thus, the chain-of-bundles model can treat only planar fracture and not the jagged breaks that are usually observed (see for instance, Fig. 1). We note in passing that the occurrence of a jagged break must mean

that such a break occurs at a lower stress than a planar break, so that an accurate theory for a planar break must be unconservative. Other deficiencies include the inability to date to develop a satisfactory failure criterion except in cases of academic interest.

MULTIPLIET THEORY OF COMPOSITE FAILURE

A new theory for damage accumulation and failure is proposed herein which rejects the chain-of-bundles model as an unnecessary intellectual impediment, and concentrates instead on the creation and growth of multiple fiber fractures. For convenience, it will be referred to here as the multipliet theory of failure. For the sake of both brevity and clarity, only a simplified version of the theory will be discussed in this section. Complications required for more accurate modelling of composite damage will be mentioned later.

Consider a composite containing N fibers each having a length L held together by a matrix. Damage resulting from loading is assumed to consist of breaks in the fibers. There will be single isolated breaks that we shall designate as singlets, pairs of breaks we will call doublets, as well as triplets, quadruplets, or in general "i-plets".

Every singlet is surrounded by n_1 nearest neighbors, each of which is subject to an overstress described by a stress concentration factor b_1 (relative to the nominal fiber stress) at the cross section in which the break is located. The overstress extends over a distance of δ_1 , but diminishes with distance from the cross section containing the break (a point neglected in most previous treatments). A doublet is considered to have n_2 nearest neighbors each subjected locally to a stress concentration factor b_2 , with the varying overstress applied over a length δ_2 . The subscript i will designate the corresponding quantities for an i -plet.

We assume in the present section that fiber failure conforms to Weibull's 2-parameter representation, i.e., the cumulative probability of failure P_f at stress σ is given by

$$P_f(\sigma) = 1 - \exp(-k\ell\sigma^m) \quad (1)$$

when the stress σ is applied uniformly over fiber length ℓ ; k and m are the Weibull parameters. If $P_f \ll 1$, this expression can be approximated by

$$P_f \approx k\ell\sigma^m \quad (2)$$

If there are N fibers each of length L , the number of singlets that will have been created by the time the stress rises to σ is given by

$$Q_1 = NP_f = NLk\sigma^m \quad (3)$$

We note that NL is the total length of fiber, so from (3) it follows that the total number of breaks depends only on the total length of fiber, and not on the dimensions of the composite per se.

The first failure occurs when $Q_1 = 1$ or $P_f = 1/N$. From (3) the corresponding stress is

$$\bar{\sigma} = \left(\frac{1}{kLN} \right)^{1/m} \quad (4)$$

The second break occurs when

$$\bar{\sigma} = \left(\frac{2}{kLN} \right)^{1/m}$$

and the i 'th when

$$\bar{\sigma} = \left(\frac{i}{kLN} \right)^{1/m} \quad (5)$$

Here $\bar{\sigma}$ is nominal stress, i.e., the uniform stress that would be present in all the fibers in the absence of breaks.

If we plot the logarithm of the number of singlets created by the time the stress reaches $\bar{\sigma}$, Q_1 , against $\log \bar{\sigma}$, it follows from (3) that we obtain a straight line of slope m , as shown schematically in Fig. 2. We now inquire into the value for Q_2 , the number of doublets that have been created. Note that the number that exist at stress $\bar{\sigma}$ is in general less than the number that have been created. The number of singlets existing, q_1 , is the number created less the number that were turned into doublets, i.e.,

$$q_1 = Q_1 - Q_2 \quad (6)$$

It is assumed here that every doublet came from a singlet, every triplet came from a doublet, etc. Thus

$$q_i = Q_i - Q_{i+1} \quad (7)$$

A singlet becomes a doublet when one of the neighboring fibers breaks in its overstressed region. Such a fiber has a probability of failure given by

$$P_f = 1 - \exp \left[-k \int_{-\delta_1/2}^{\delta_1/2} \sigma^m dx \right] = 2k \int_0^{\delta_1/2} \sigma^m dx \quad (8)$$

If we assume the stress σ varies linearly from $k_1 \bar{\sigma}$ to $\bar{\sigma}$ over the length $\delta_1/2$, we obtain

$$P_f = 2k \int_0^{\delta_1/2} \left[b_1 \bar{\sigma} - \frac{2x}{\delta_1} (b_1 - 1) \bar{\sigma} \right]^m dx \quad (9)$$

$$= k \lambda_1 (b_1 \bar{\sigma})^m \quad (10)$$

$$\text{where } \lambda_1 = \delta_1 \frac{b_1^{m+1} - 1}{b_1^m (b_1 - 1) (m+1)} \quad (11)$$

is the "effective length" of the over-stressed section of fiber for the purpose of calculating P_f . The ratio λ_1/δ_1 is shown in Fig. 3 for various values of m and b_1 . We note that

$$\lambda_1 \rightarrow \delta_1 \quad \text{when } b_1 \rightarrow 1 \quad (12)$$

$$\rightarrow \frac{\delta_1}{m+1} \quad \text{when } b_1 \gg 1 \quad (13)$$

These limiting relationships are familiar from Weibull theory. Equations (10)-(13) apply equally well when i is used as the subscript instead of 1.

Except for (8) and (9), all of the references cited assumed δ is a constant, independent of i , and is equal to a fixed λ for all b_i and all m .

The probability that a given singlet becomes a doublet is (from (10))

$$P_{1 \rightarrow 2} = k(b_1 \bar{\sigma})^m n_1 \lambda_1 \quad (14)$$

The number of doublets created in loading to stress $\bar{\sigma}$ thus becomes

$$Q_2 = Q_1 k(b_1 \bar{\sigma})^m n_1 \lambda_1 \quad (15)$$

Generalizing this result,

$$Q_{i+1} = Q_i k(b_i \bar{\sigma})^m n_i \lambda_i \quad (16)$$

We can also express Q_{i+1} in absolute terms. From (15)

$$\begin{aligned} Q_2 &= NLk\bar{\sigma}^m \cdot \frac{b_1^m n_1 \lambda_1}{NL} \\ &= (NLk)^2 \bar{\sigma}^{2m} \left(\frac{b_1^m n_1 \lambda_1}{NL} \right) \end{aligned} \quad (17)$$

Similarly

$$Q_3 = (NLk)^3 \bar{\sigma}^{3m} \left(\frac{b_1^m n_1 \lambda_1}{NL} \right) \left(\frac{b_2^m n_2 \lambda_2}{NL} \right) \quad (18)$$

and

$$Q_i = (NLk)^i \bar{\sigma}^{im} \prod_{j=1}^{i-1} \frac{b_j^m n_j \lambda_j}{(NL)^{i-1}} \quad (19)$$

From (19) we see that a plot of $\ln Q_i$ vs. $\ln \bar{\sigma}$ is a straight line of slope im . From (16), $Q_{i+1} = Q_i$ when

$$k(b_i \bar{\sigma})^m n_i \lambda_i = 1 \quad (20)$$

If we were to assume that b , n and λ are all constant, independent of i , then all Q 's would be equal when σ takes the value implied by (20). Actually b_i , n_i and λ_i all increase as i increases. Thus the value of $\bar{\sigma}$ at which $Q_{i+1} = Q_i$, namely

$$\bar{\sigma} = \frac{1}{b_i} \left(\frac{1}{n_i \lambda_i k} \right)^{1/m} \quad (21)$$

keeps decreasing as i increases. This situation is illustrated schematically in Fig. 2.

Now since each multiplet comes into being by fracture of a fiber adjacent to a multiplet of the next lower order, $Q_{i+1} \leq Q_i$. Consequently the portion of the Q_{i+1} line extending beyond its intersection with Q_i has no physical meaning, and is therefore omitted. The envelope of the lines is drawn in heavily, because it has a special significance. Over the stress range within which an i -plet lies on the envelope, it is unstable. That is, as soon as it is created it will immediately become an $(i+1)$ -plet, which will immediately become an $(i+2)$ -plet, etc., resulting in fracture of the composite. The failure stress is the lowest stress at which any unstable i -plet is present. This is the stress at which the envelope curve (or more precisely, broken line), intersects the horizontal line $Q = 1$, or $\ln Q = 0$. We note in passing that only those portions of a Q -line to the left of this intersection have any physical significance; clearly higher stresses than the fracture stress cannot be applied to the composite.

The envelope plays a role somewhat analogous to that played by the failure line in a conventional Weibull plot. In such a plot $y = \ln \ln P_s^{-1}$ is plotted against $x = \ln \sigma$. The abscissas are thus identical. The ordinates are closely related since for sufficiently small P_f ,

$$\ln \ln P_s^{-1} = \ln[-\ln(1-P_f)] \approx \ln P_f \quad (22)$$

If the survival probability of a volume V_1 of a material is given by the Weibull expression

$$P_s = \exp[-kV_1\sigma^m] \quad (23)$$

Then the Weibull plot becomes a straight line of slope m as shown in Fig. 4. The line for volume V_2 is another line of slope m . The vertical separation of the two lines is $\ln(V_2/V_1)$. The mean fracture stress is given approximately by the intersection of the fracture line with the line corresponding to $P_s = 0.5$, i.e., $\ln \ln P_2^{-1} = -0.37$. The change in fracture stress due to the size effect can be found by observing how the intersection point changes as the fracture line is shifted vertically a distance appropriate to the volume change.

In the case of the composite, it follows from (19) that $Q_1 \propto NL$. Since for fixed fiber ratio, $NL \propto V$, the line for each multiplet in Fig. 2 (and therefore also the envelope) moves up or down a distance $\ln(V_2/V_1)$ when the volume is changed from V_1 to V_2 . The effect on the fracture stress is found by seeing how the intersection of the envelope with the line $\ln Q = 0$ changes with such a vertical shift.

Another way of showing the size effect is to plot $\ln \bar{\sigma}_f$ vs. $\ln V_1$ where $\bar{\sigma}_f$ is the mean fracture stress. The result for a Weibull material (i.e., one obeying (23)) is a straight line of uniform slope $(-1/m)$, as shown in Fig. 5a. In the case of the composite, according to the present theory such a plot leads to a broken line. Each line segment corresponds to a line segment of the envelope shown in Fig. 2 and has slope $(-1/m)$. The result is shown schematically in Fig. 5b. This finding differs sharply from those for most previously published theories. For instance, Fig. 6a taken from Zweben (7)

shows that such a plot leads to straight lines for all the theories he considered. Fig. 6b, taken from McKee and Sines, shows a bilinear relation for such a plot. Since their theory predicted a 6" cable (5×10^7 volume elements) would fail by instability of a septuplet, the present theory would predict at least 6 line segments to the right of the abscissa 10^8 in Fig. 5b. The flattening out of the curve for large composites predicted by the present theory may be very important; if confirmed by additional research, it means that very large composite structures can be substantially stronger than has heretofore been realized.

In many cases we seek not the mean fracture stress of the composite but the stress corresponding to some prescribed low probability of failure. This is the probability that an unstable crack is present at the stress under consideration. To find the stress at which $P_f = 0.01$, for example, all that is needed is to read off the stress at which the ordinate of the envelope is $Q = 0.01$, or $\ln Q = \ln 0.01 = -4.61$.

The preceding discussion points out a number of similarities between the failure envelope for composites and the failureline of a simple Weibull material. There are also important differences. It is not uncommon to hear numerical values cited for the Weibull modulus m of a composite. This implies that the failure envelope is a straight line, which, as we have shown, is not so. One can identify an effective modulus for calculating the change in strength in going from one size to another. But strictly speaking, the two sizes have to be specified. One cannot even speak of a modulus over a range of sizes, since as we shall find in the next section, a more accurate analysis gives a smooth curve instead of a broken line for the failure envelope. The effective modulus is thus the slope of the chord extending between the two points on the failure envelope that correspond to

the two sizes under consideration. In view of this any discussion of the Weibull modulus of a composite should be carefully qualified.

MATHEMATICAL CONSIDERATIONS

It will be obvious to critical readers that the engaging simplicity of the theory outlined in the previous section is largely a result of the numerous mathematical approximations employed. Most obvious perhaps, is the use of Eq. (2). Others include use of Q_i instead of $Q_i - Q_{i+1}$ for the number of i -plets actually present, neglect of the fact that the estimated probability of fracture of an overstressed fiber element should really take into account the fact that it survived some lower stress, neglect of edge effects, etc. An accurate estimate of the errors involved in such approximations in cases of practical interest would involve the prohibitively difficult task of finding an exact solution. A rough idea of the errors involved can be obtained, however, by using the theory outlined to solve a 2-D problem treated exactly (or nearly exactly) by Harlow and Phoenix.

To do this we assume with them that the probability of failure of a fiber of length δ is given by

$$P_f(\delta) = 1 - \exp(-(\sigma/\sigma_\delta)^m) \quad (24)$$

or using our approximation

$$P_f(\delta) = \left(\frac{\sigma}{\sigma_\delta}\right)^m \quad (25)$$

We adopt their local load-sharing rule for a single ply tape, which leads to

$$\begin{aligned} b_1 &= 1.5 & b_3 &= 2.5 \\ b_2 &= 2.0 & b_4 &= 3.0 \end{aligned}$$

With them we assume that $n_i = 2$, and that $\lambda = \delta = \text{constant}$. Using Eq. (25) for the probability $P_1(\delta)$ that any arbitrarily chosen fiber segment of length δ is fractured, together with Eq. (16) rewritten in the form

$$P_{i+1}(\delta) = P_i(\delta) 2 b_i^m \left(\frac{\sigma}{\sigma_\delta}\right)^{m1} \quad (26)$$

for the number of (i+1)-plets divided by the total number of elements NL/δ , we obtain in no more than two or three minutes the table below.

	$\ln(\sigma/\sigma_\delta) = -2$	$\ln(\sigma/\sigma_\delta) = -1$
$\ln P_1$	-10	-5
$\ln P_2$	-17.28	-7.28
$\ln P_3$	-23.12	-8.12
$\ln P_4$	-27.85	-7.85
$\ln P_5$	-31.66	-6.66

The data in this Table are displayed graphically in Fig. 7. These results are to be compared with those given by Harlow and Phoenix for the same problem, Fig. 8. In making the comparison due account must be taken of differences in notation: $\sigma = x$; $m = \rho$; $P = W$.

The most conspicuous difference between the two figures is that Harlow and Phoenix's failure envelope is a smooth curve instead of a broken line. Obviously it should be a smooth curve. This follows immediately from the fact that when Eq. (1) is used for P_f , Q_i approaches Q_{i-1} asymptotically instead of crossing it. But perhaps the most important point to note is that for a given ordinate the abscissas differ by less than 0.05, which means the failure stresses obtained by the two methods will generally differ by only a few percent. This is considerably less than the usual experimental scatter and also considerably less than the uncertainties that must be taken into account in most practical problems. These uncertainties include the stress at which debonding commences, the length that is debonded for each

multiplet as a function of stress level, the friction between fiber and matrix, etc. One of the primary virtues of the present approach is that it provides an analytical framework for taking all such effects into account as soon as they are known, without encountering the obstacle of mathematical intractability. For instance, if debonding occurs, b_1 , δ_1 , and b_2 all become functions of the applied stress σ , and the $\ln Q_1$ vs $\ln \sigma$ plots become curves instead of straight lines. If the functional relations $b_1(\sigma)$ and $\lambda_1(\sigma)$ are known, however, the Q_1 curves can be constructed in only a few minutes each, and their envelope becomes the failure envelope for the problem under consideration.

RELATION TO GRIFFITH AND WEIBULL CONCEPTS

In this theory there are two levels of defect. In the first level are pre-existing fiber defects as in Weibull theory and rupturing of individual fibers is governed by the weakest link concept. The i -plets discussed in the previous sections constitute the second level of defect. Although some singlets may pre-exist as a result of manufacturing (and their presence could be readily incorporated into the theory) the prime emphasis here is on the multiplet structure resulting from a series of fiber ruptures as the load increases. Thus the ultimate failure is a second-level-defect phenomenon, in which the "cracks" or multiplets are not pre-existing but are caused by the application of stress.

It is the multiplet model which relates to Griffith's crack instability concept. The analogy consists in fact that an i -plet becomes unstable at the stress at which the Q_i curve intersect the Q_{i+1} curve. There are also significant differences, however. For instance, Griffith like Weibull, thought of the cracks as pre-existing, whereas here they are a result of load application. More important, in his theory all cracks of a given size have the same strength. In the present theory there is a range of strengths for a multiplet of any given rank. If only one is present, the strength is the expected strength of the weakest of the n_i fiber segments of length λ_i surrounding the multiplet. If M are present, the strength of the weakest of the multiplets is determined by the strength of the weakest of the Mn_i surrounding fiber segments.

CONCLUDING DISCUSSION

The theory proposed herein is believed to combine the best features of the various preceding treatments, and in so doing has many similarities to them. There are, however, some unique features. These include: a better definition of "crack instability" as the concept pertains to composites; a quantitative representation of the defect structure of a composite at any given stress level, which can be used to establish the stress-strain relation; and a recognition of the difference between the elastic transfer lengths and the "effective length" λ in the context of weakest link theory. Perhaps even more significant, it can incorporate important effects that cannot be treated in the conventional chain-of-minibundles approach, such as the variation of stress transfer length with multiplet order, the interaction between multiplets in different minibundles, etc. As a result, the present approach is believed to model physical reality more closely than its predecessors. In addition, it provides a methodology which allows the various complications discussed to be incorporated and their effects analyzed in an orderly fashion.

To apply the new approach to practical situations, however, several advances in our understanding are required. We need to know the local elastic stress distribution in the fibers in the neighborhood of each multiplet order that is likely to occur. The stress at which matrix yielding or debonding begins needs to be known, as well as the changing influence of these factors on stress distribution as the stress continues to increase. These matters require an understanding of the inelastic behavior of the matrix, the frictional shear stress between fiber and matrix in the debonded region, the inception and growth of cracks in the matrix, etc. The investigation of such questions appears to be the next logical step in achieving a useful and accurate model for cumulative damage and ultimate failure of fibrous composites in tension.

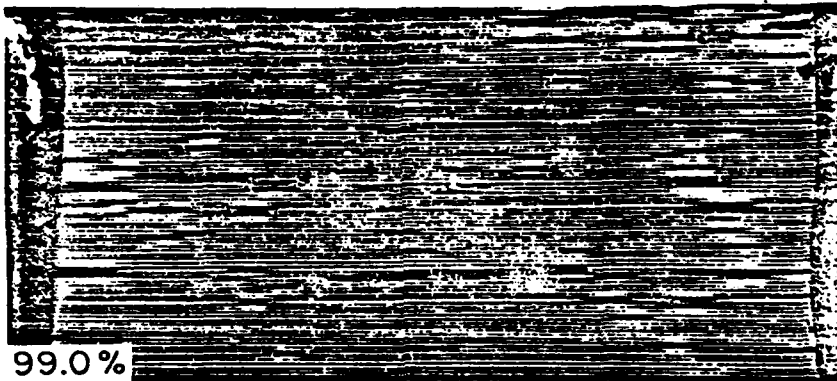
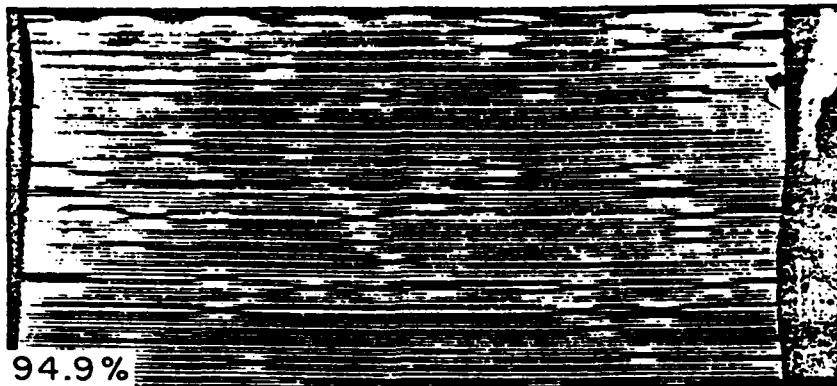


Figure 1. Jagged Fracture of Glass - Epoxy Composite (after Rosen).

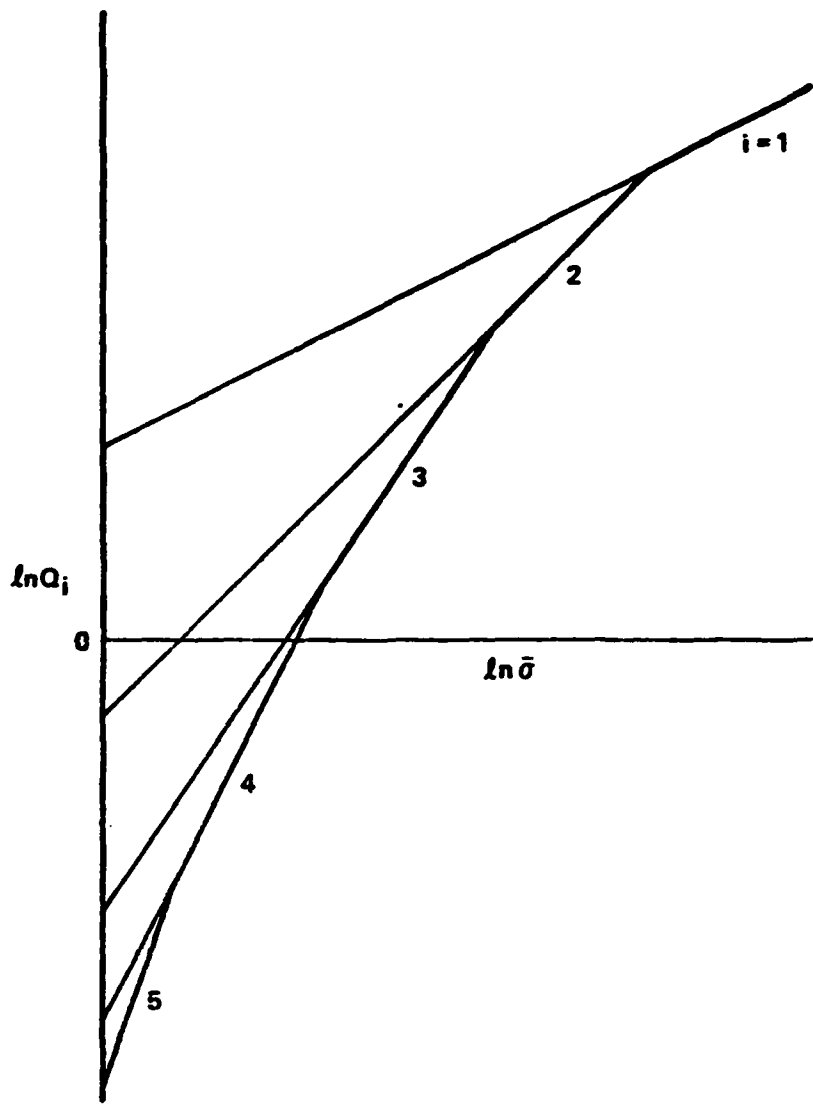


Fig. 2 - Number of Multiplets vs.
Applied Stress (Schematic)

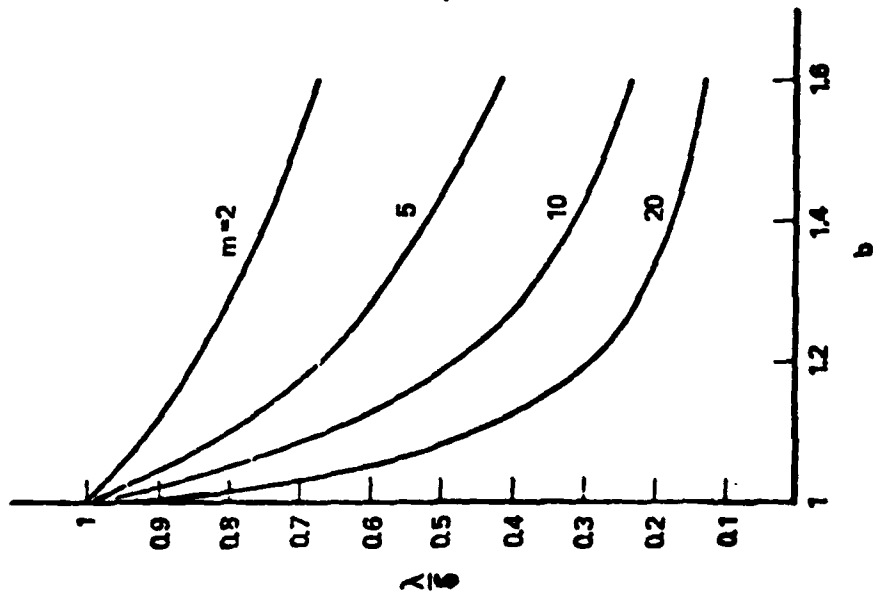


Fig. 3 - λ/δ Ratio vs. Stress

Concentration Factor

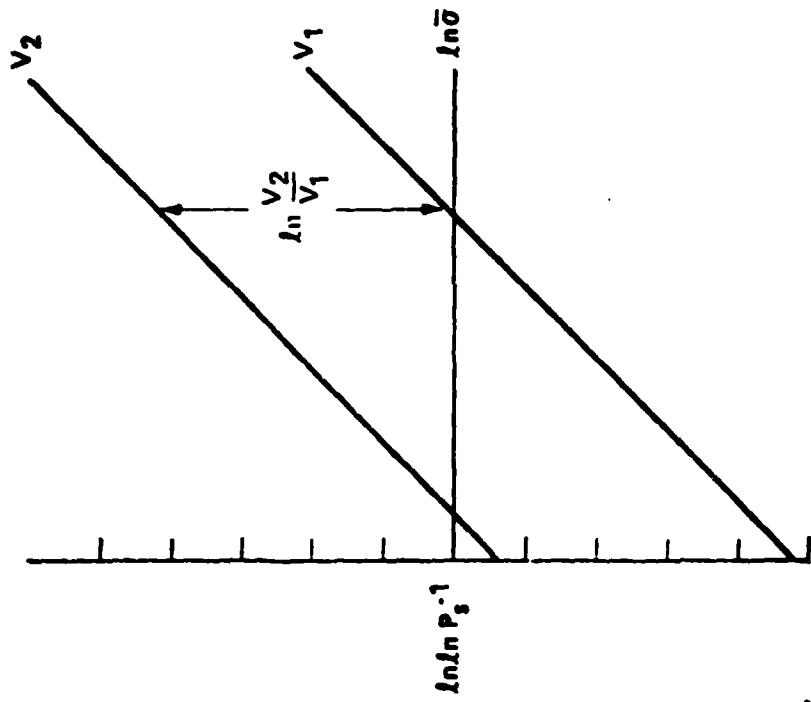
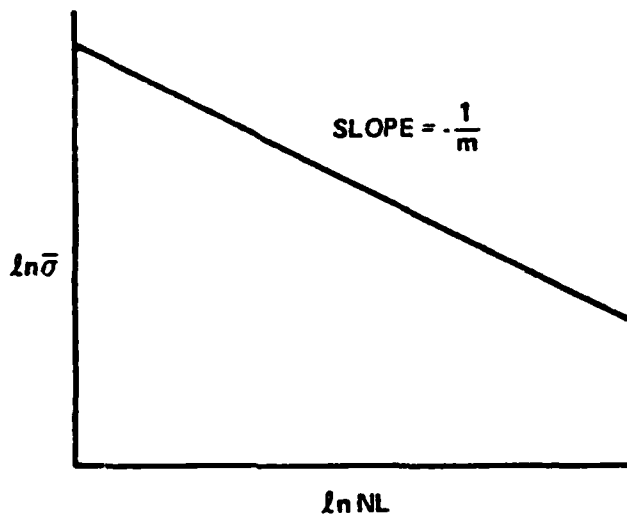
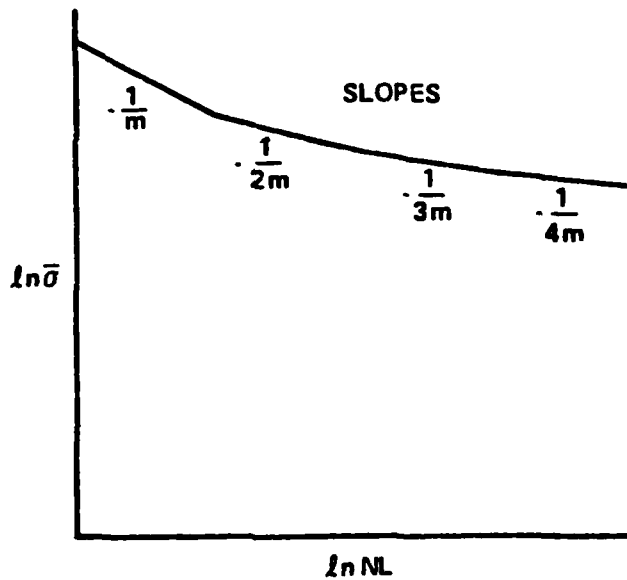


Fig. 4 - Weibull Size Effect

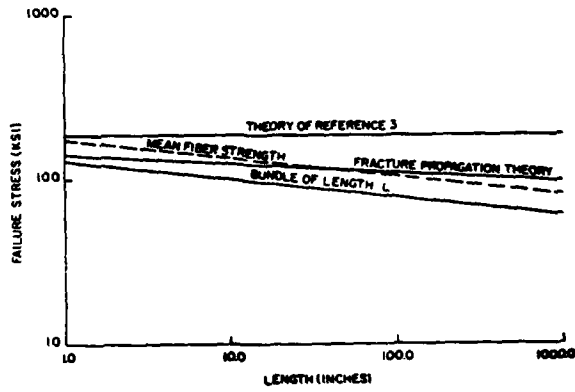


(a) Weibull material



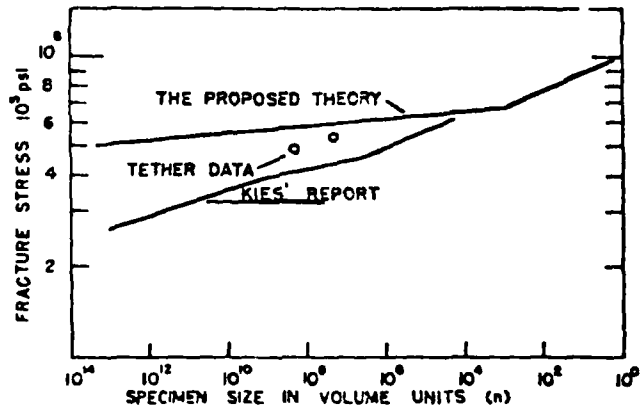
(b) Fibrous composite

Fig. 5 - Strength-Size Relations (Schematic)



Variation of failure stresses with length

(a)



(b)

Fig. 6 - Zweben (a) and McKee and Sines
(b) Predictions of Composite Size-Strength Relation

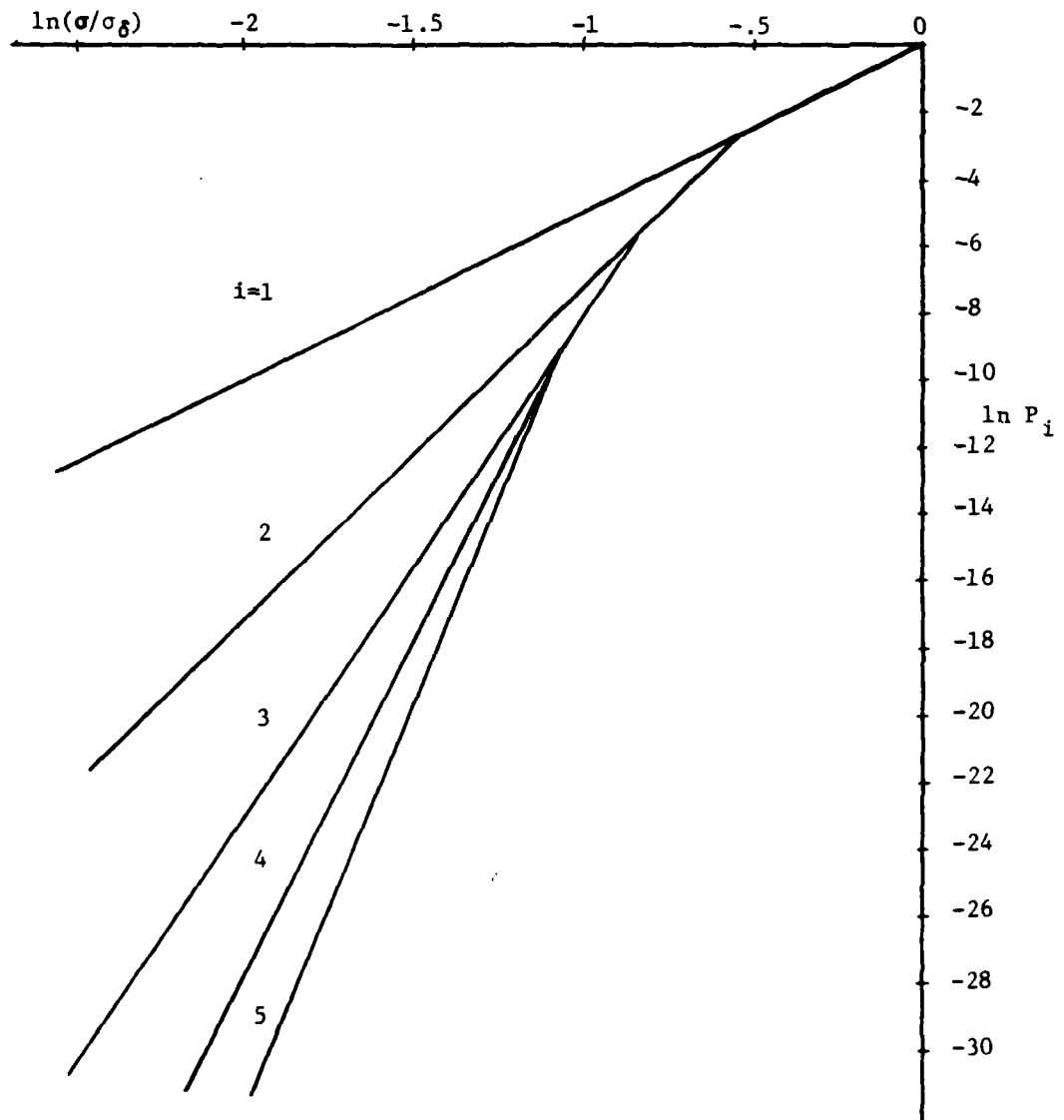


Fig. 7 - Idealized Single Ply Tape Problem
Solved by Method of Present Paper

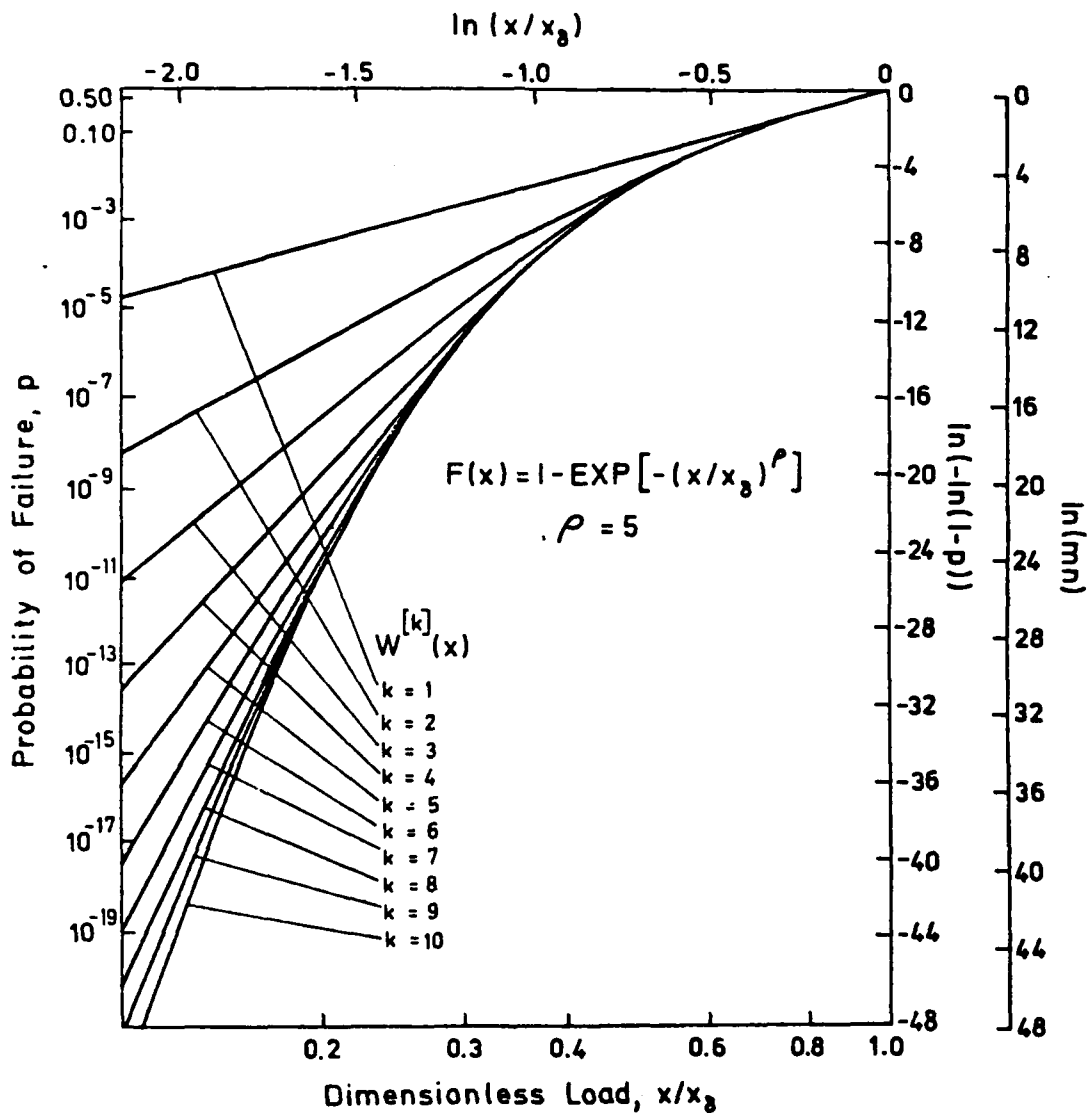


Fig. 8 - Convergence of the characteristic distribution function $W^{[k]}(x)$ to its limit $W(x)$ as k increases. Fiber elements have a Weibull strength distribution. (Taken From Harlow and Phoenix)

REFERENCES

- (1) H.E. Daniels, "The Statistical Theory of the Strength of Bundles of Threads," Proc. Roy. Soc., A., Vol. 183, No. 995 (1945), pp. 405-435.
- (2) B.D. Coleman, "On the Strength of Classical Fibers and Fiber Bundles," J. Mech. and Phys. of Solids, Vol. 7, No. 1 (1959), pp. 66-70.
- (3) H. Leon Harter, "A Survey of the Literature on the Size Effect on Material Strength," Technical Report AFFDL-TR-77-11 Air Force Flight Dynamics Lab, WPAFB, April 1977.
- (4) D.E. Gucer and J. Gurland, "Comparison of the Statistics of Two Fracture Modes," J. Mech. Phys. Solids, Vol. 10 (1962), p. 365.
- (5) B.W. Rosen, "Tensile Failure of Fibrous Composites," AIAA J., Vol. 2 (1964), p. 1965.
- (6) C. Zweben, "Tensile Failure of Fiber Composite," AIAA J., Vol. 6 (12) (1968), pp. 2325-2331.
- (7) C. Zweben and B.W. Rosen, "A Statistical Theory of Composite Strength with Application to Composite Materials," J. Mech. Phys. Solids, Vol. 18, pp. 189-206.
- (8) P.M. Scop and A.S. Argon, "Statistical Theory of Strength for Laminated Composites," J. Compos. Matls., Vol. 1 (1967), p. 92
- (9) S.W. Chatterjee, P.V. McLaughlin, Jr. and D.L. Lowe, "An Investigation of the Tensile and Shear Strengths of 3-D Carbon - Carbon Composites," AIAA/ASME Structures, Structural Dynamics & Materials Conference Proceedings, 1976.
- (10) D.G. Harlow and S.L. Phoenix, J. Compos. Matls., 12 (1978) 195-214.
- (11) D.G. Harlow and S.L. Phoenix, J. Compos. Matls., 12 (1978) 314-334.
- (12) D.G. Harlow and S.L. Phoenix, Intl. J. Fracture 15 (1979) 321-336.
- (13) D.G. Harlow and S.L. Phoenix, "Probability Distributions for the Strength of Composite Materials I: Two-Level Bounds" (submitted).
- (14) D.G. Harlow and S.L. Phoenix, "Probability Distributions for the Strength of Composite Materials II: A Convergent Sequence of Tight Bounds," to be published in Int. J. Fract.

Appendix 4.8

The Correlation of Viscoelastic Behavior
with Fracture Properties

Dr. Donald J. Plazek
Professor

Science of Fracture Research Project
AFOSR Contract #F49620-78-C-0101

School of Engineering
University of Pittsburgh
Pittsburgh, PA 15261

The Correlation of Viscoelastic Behavior with

Fracture Properties

Co-Principal Investigator

Donald J. Plazek

The viscoelastic behavior of elastomeric and epoxy network polymers with known molecular structural variations is being determined for correlation with the fracture and static mechanical response. The preparation along with static and fracture testing is being carried out by the Akron University team of investigators.

Following the establishment of the crosslinking procedures for the polybutadiene, PB, and styrene-butadiene, SBR, elastomers at the Polymer Science Institute of Akron University, initial samples designated PB-1 and 2 and SBR-1 were provided to us at the University of Pittsburgh for the characterization of their viscoelastic behavior. The study of the physical properties of these elastomers was started early this summer (1980) both in Akron and in Pittsburgh. To date the studies of the viscoelastic behavior have been solely that of torsional creep. The shear creep compliance curves at temperatures between about -50° and 40°C have been determined on the three materials PB-1 and 2 and SBR-1. PB-2 has a crosslink concentration that is about 1/2 of that of PB-1. The indicated equilibrium compliance of the polybutadiene with the larger concentration of elastic chains, the PB-1, is indeed lower by a factor of 0.72. If the concentration of chains between crosslinks were truly twice as great and if there were no or relatively few effective entanglements a factor of 1/2 in the compliance would be expected. A comparison of the reduced creep compliance curves which have been determined are shown in Figure 1 where it can be seen that the difference in the curves increases with the passage of time. The entanglement compliance plateaus are clearly visible because of the characteristic low molecular weight per entangled chain unit, M_e , for polybutadiene, ~ 2000 .¹ The M_e for natural rubber, 1,4 cis, polyisoprene is 5800 ¹ and at comparable crosslinking levels no separate entanglement plateau can usually be distinguished. Using $2.8 \times 10^{-8} \text{ cm}^2/\text{dyne}$ for the plateau compliance seen in Figure 1 a molecular weight between junction points of about 640 is indicated. This low number clearly indicates that both crosslinks and entanglements are involved in determining the number of active network chains. The data displayed in the figures shown here have been reduced to represent the response over an enhanced time scale range at a reference temperature of 0°C . Time-temperature reduction procedures were utilized in the data analysis.

The PB-2 data are shown at the experimentally expected response times for 0°C , but it was necessary to shift the PB-1 data by 1.05 decades of time to shorten times of response to achieve the superposition seen at the short time end of the reduced time scale. The slower response of the more highly crosslinked PB-1 network suggests that the glass temperature, T_g , for

the PB-1 elastomer is higher than that of the PB-2. A difference in T_g in this direction is expected from the difference in crosslinking level, but this has not been confirmed at present due to unexpected behavior observed in linear dilatometry measurements of the polybutadiene sample.

Since most of the specimens are being cemented into the testing instruments with a cyanoacrylate adhesive, absolute compliance levels are being checked by making measurements on cylinders with different dimensions to insure that the end conditions of the specimens are not causing appreciable errors.

Figure 2 shows the retardation spectra $L(\ln\tau)$ which have been obtained from the reduced compliance curves. Two maxima are observed reflecting the presence of two groups of viscoelastic mechanisms which contribute to the two plateau compliance levels seen in Figure 1. The curve characterizing the response of the looser network PB-2 shows larger values in the terminal response region reflecting its higher compliance. Utilizing these spectra the dynamic mechanical properties of these two samples have been calculated and are presented in Figure 3. Although it can be seen that the loss tangent, $\tan \delta$, of the looser network is higher at low frequencies, it is clear that this is so only because the storage modulus, G' , is lower since the loss moduli are virtually identical once the shift in time scale of a decade is accounted for. This result is somewhat surprising and constitutes a prediction that the fracture behavior of these materials should be nearly the same.

Creep measurements are also partially completed on a series of three Viton elastomers whose crosslinking densities are 0.127, 0.251 and 0.471. This series of elastomers provides a contrasting molecular structure since they are copolymers of vinylidene fluoride and hexafluoropropylene. The measurements to date on these fluorinated elastomers definitely show more pronounced long time losses as the level of crosslinking decreases. This is in accord with earlier findings on natural rubber.²

Two creep apparatuses are currently being used for the measurements discussed above. A third one is being modified so that some of the measurements on the polybutadiene and the styrene-butadiene elastomers can be carried out at temperatures near their T_g 's. A low temperature liquid thermostat is being constructed which should make measurements possible down below -80°C , if necessary.

References

- 1) J. D. Ferry, "Viscoelastic Properties of Polymers", 2nd ed.,
Wiley, New York, NY 1970, p. 406.
- 2) D. J. Plazek, J. Polym. Sci., A-2, 4, 745 (1966).

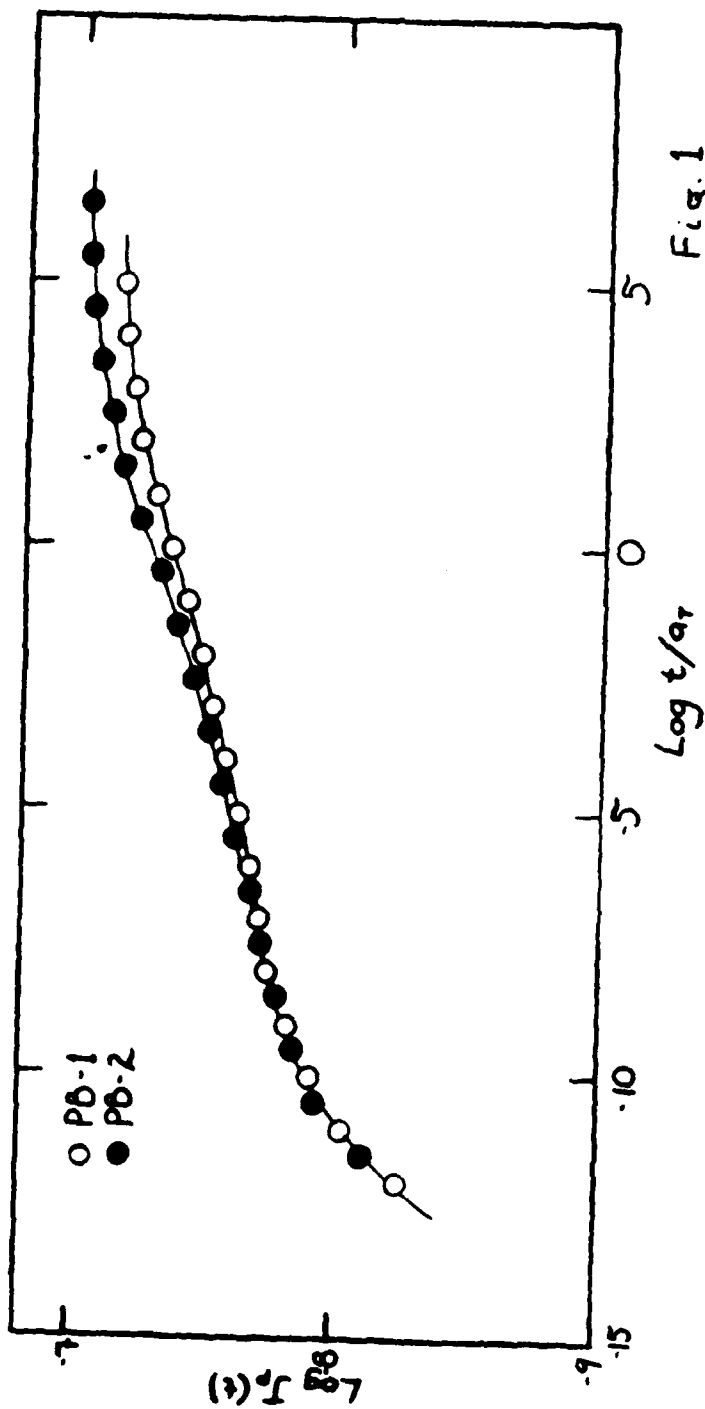


Fig. 1

Logarithm of the reduced shear creep compliance, $J_p(t)$, plotted versus the logarithm of the reduced time scale, t/a_T for two polybutadiene elastomers, PB-1 and PB-2. Reference Temperature, $T_0 = 0^\circ\text{C}$.

DR 1520

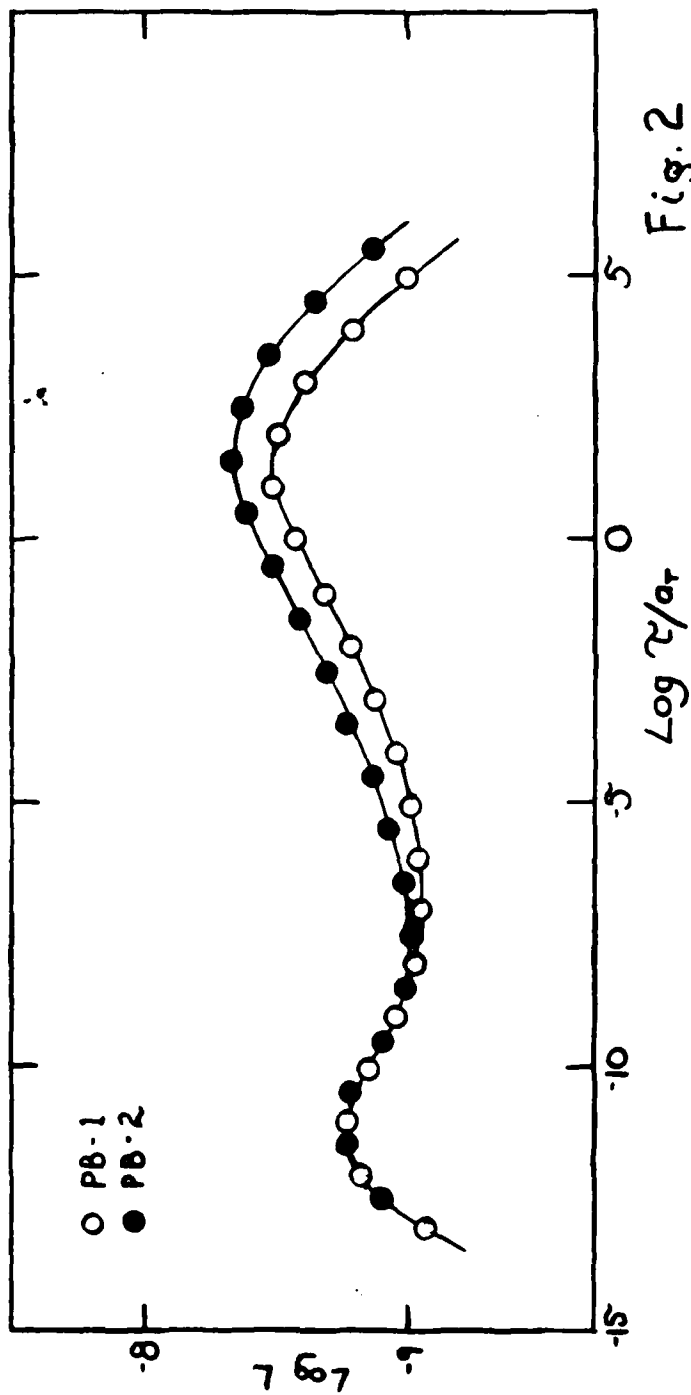


Fig. 2

Double logarithmic plot of the retardation spectra of the two polybutadiene elastomers against the reduced retardation times. $T_0 = 0^\circ\text{C}$.

160

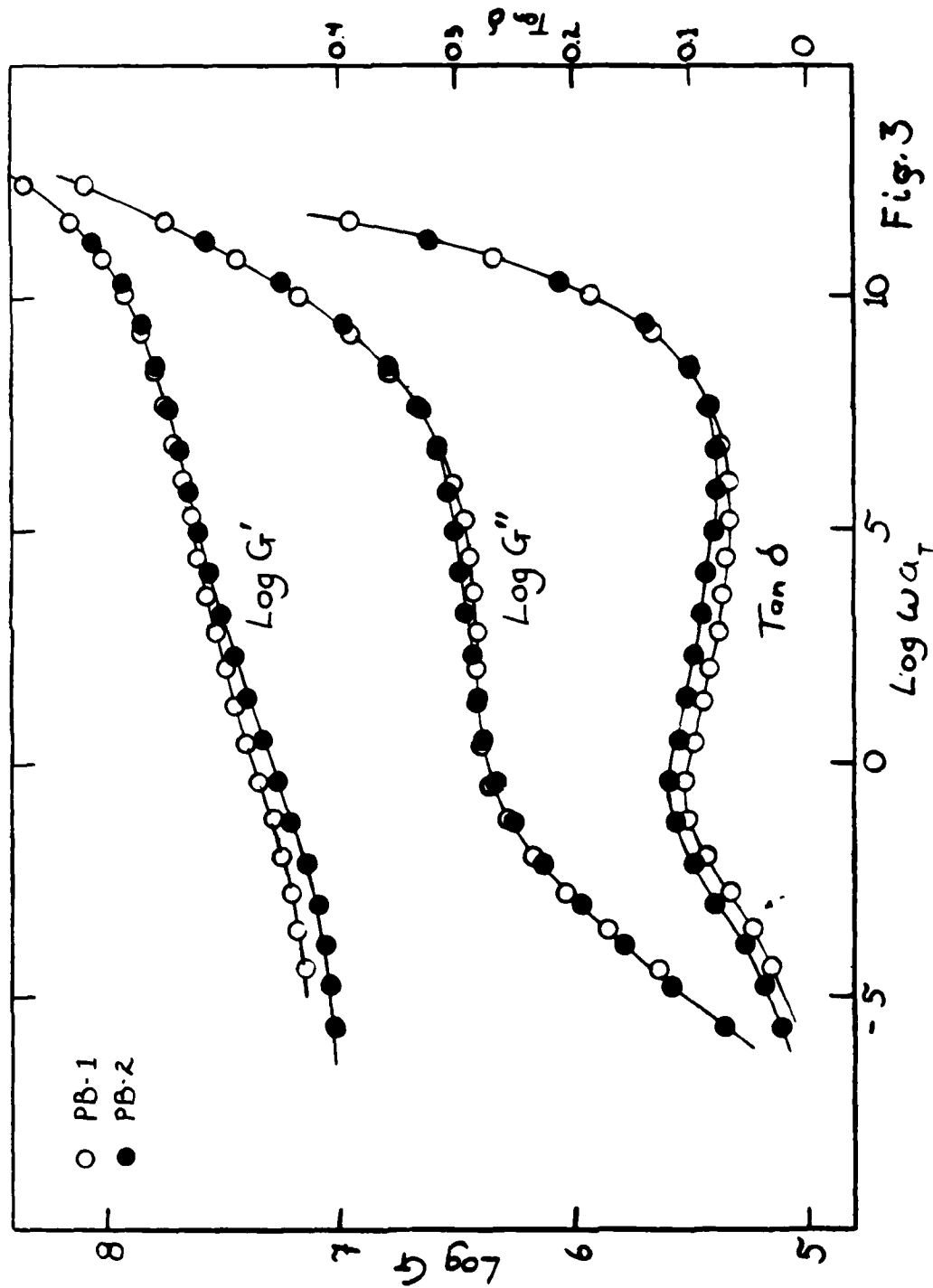


Fig. 3

Storage, G' , and loss, G'' , moduli of the polybutadienes plotted logarithmically as functions of the reduced angular frequency scale along with linear values of the loss tangent, $\text{Tan } \delta$. $T_0 = 0^\circ\text{C}$

Appendix 4.9

Feasibility of Melt Fracture Set-Up

Dr. Jan T. Lindt
Associate Professor

Science of Fracture Research Project
AFOSR Contract #F49620-78-C-0101

School of Engineering
University of Pittsburgh
Pittsburgh, PA 15261

FEASIBILITY DEMONSTRATION OF MELT FRACTURE SET-UP

J. T. Lindt and Y.-S. Wang

Review of Objectives

1. To design an apparatus for studies of melt fracture
2. To generate flow conditions under which melt fracture occurs
3. To identify and measure the characteristic variables
4. Interpretation of data

Summary of Progress

The above objectives have been set for a period of one year. During the 7-month period covered by this communication an experimental set-up has been developed and flow regimes associated with melt fracture have been generated. The first part of the experimental program has centered on the nature of pressure fluctuation associated with melt fracture of polyethylene. In general, the pressure fluctuations show a fairly regular periodicity. To analyze the nature of the pressure fluctuations, a faster recording system is required.

Description of the Experimental Set-up

To generate a flow regime associated with melt fracture, an apparatus has been designed and subsequently built as shown in Fig. 1. The experimental set-up can be divided into three parts fulfilling the following functions:

1. Generation of homogeneous melt,
2. Expelling the melt at a steady rate,
3. Generation of melt fracture.

The melt is generated in a plasticating 1" NRM extruder.

The hydraulic system to discharge the melt through the test cell consists of two cylinders mounted back to back. The right cylinder serves as a reservoir of melt while the left one contains hydraulic oil and is to drive the expelling unit. Both cylinders have a 3 1/4" bore and 12" stroke (manufactured by Tomkins-Johnson Company). The pressure required is generated by a hand pump (model 160-6, Templeton Kenley and Company) connected to an oil accumulator (R4-20-5Co, Hydrodyne Industries).

The test cell designed to generate and observe melt fracture is shown in Fig. 2. It consists of two identical profiled aluminum plates that bound the flow. The distance between the plates h_g is adjustable (so far $h_g = 2\text{mm}$ has been used). The side plates fitting the vertical slots have been made of stress-free glass for optical measurements of stress; a "heavy-duty" set of aluminum plates has also been made to be used during the developmental stages of the project, or in measurements dedicated to hydrodynamic pressure determinations.

The instrumentation includes Dynisco pressure transducers (model PT 420/411), and Omega iron-constantan thermocouples; the outputs were measured using Houston Instruments two-channel recorders (model BS 239-5I). Locations of the sensors are shown in Fig. 2.

Experiments with LDPE

During the developmental stage a low density polyethylene was used. Although most of our effort during this initial period was devoted to designing and developing the experimental set-up, a number of tests have been run. Melt fracture has been observed at a stress level 10^5 N/m^2 in agreement with some older data.⁽¹⁾ A set of data illustrating our experimental conditions is shown in Table 1.

Table 1
EXAMPLE OF FLOW MEASUREMENTS (ARCO LDPE)

<u>FLOW RATE</u> <u>[g/min]</u>	<u>MELT TEMPERATURE</u> <u>[°C]</u>	<u>PRESSURE GRADIENT</u> <u>PSI/cm</u>	<u>SHEAR STRESS</u> <u>N/m²</u>	<u>REMARKS</u>
18.5	141	88	6.1×10^4	Shark Skin
23	141	106	7.3×10^4	"-
30.5	141	111	7.6×10^4	"-
39	141	120	8.4×10^4	Melt Fracture
46	141	114	7.8×10^4	
49	141	111	7.6×10^4	

The appearance of "shark skin" on the surface of extrudate, and the gross distortions of it, were accompanied by pressure fluctuations in the test cell. Although they seemed to show a fairly regular amplitude and periodicity, some additional signal conditioning and faster recording capabilities are required for a successful analysis of the nature of the pressure fluctuations which are believed to play an important role in the propagation of flow instabilities under consideration.

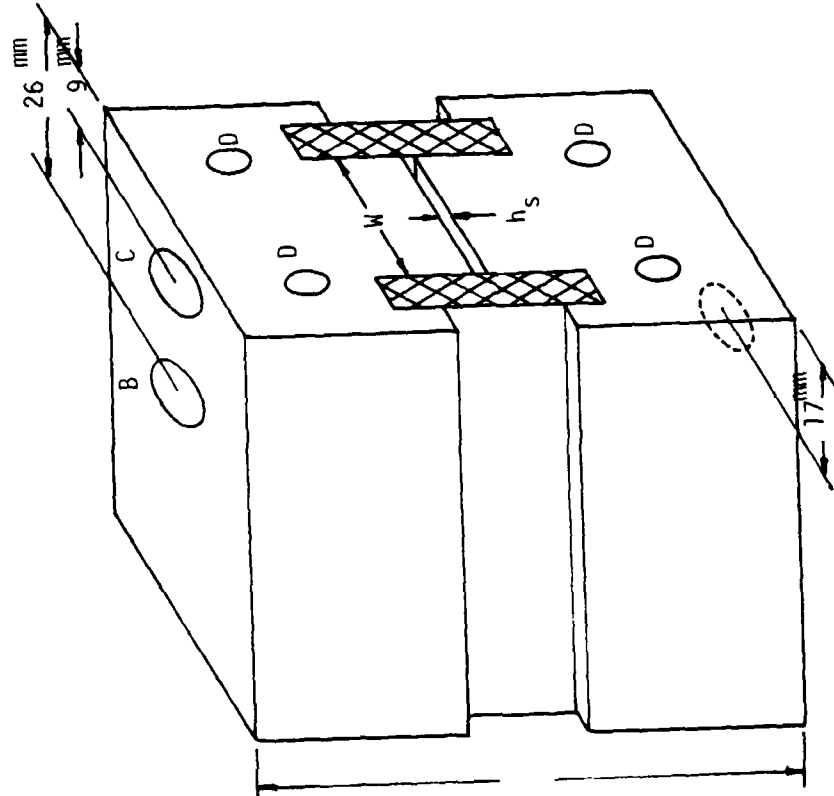
Recommendations for Future Research

In view of the premature termination of this project after eight months devoted to demanding development of the experimental set-up, the following suggestions are made for a possible follow-up in the future:

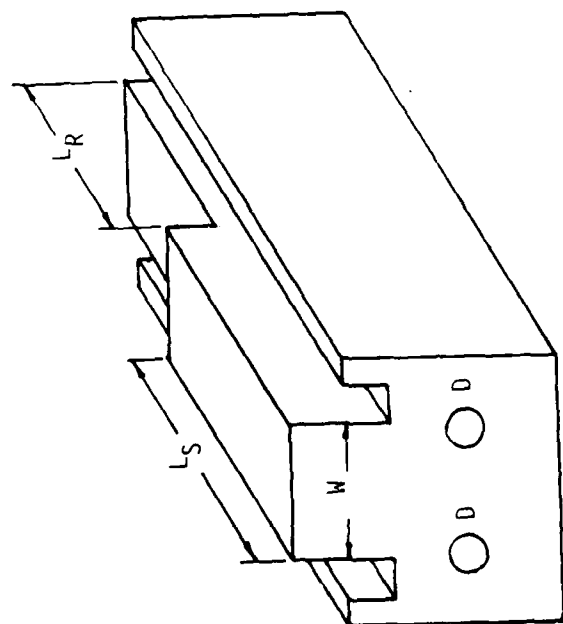
1. To analyze the frequency and amplitude of the pressure fluctuations as functions of the stress/flow rate level, of the shape of the inlet regions (c.f. Fig. 2), and of the molecular parameters of the given polymer.
2. To perform a theoretical analysis of the oscillatory flow involved.

Reference

- (1) J. Vlachopoulos and T. W. Chan, *Journal of Applied Polymer Science*, 21, 1177 (1977).



A- pressure Transducer
 B- plug
 C - thermocouple
 D - heating element



$h_R = 82 \text{ mm}$ $L_R = 25 \text{ mm}$
 $h_S = 2 \text{ mm}$ $L_S = 35 \text{ mm}$
 $W = 20 \text{ mm}$

Figure 2 - Test Cell

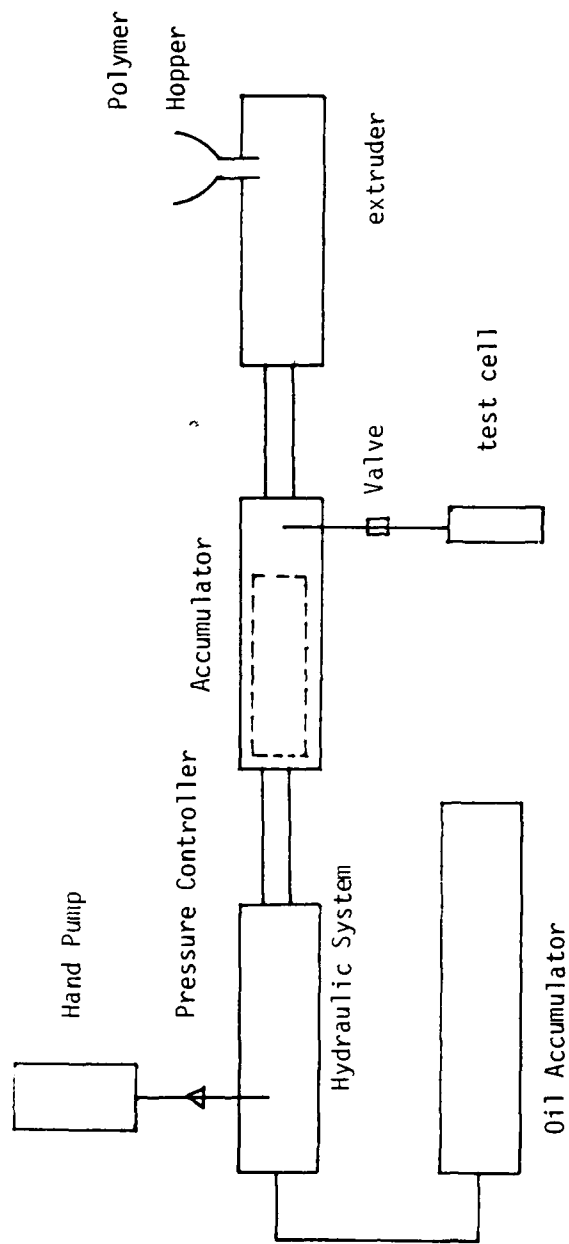


Fig. - 1 EXPERIMENTAL SET-UP

SETEC # 80-051
October 1980

Appendix 4.10

Fracture In Fully Plastic Bodies

Dr. Howard A. Kuhn
Professor

Science of Fracture Research Project
AFOSR Contract #F49620-78-C-0101

School of Engineering
University of Pittsburgh
Pittsburgh, PA 15261

FRACTURE IN FULLY PLASTIC BODIES

Introduction

Fracture during hot working processes is an increasingly important problem because of the use of highly alloyed high temperature materials in modern defense and industrial systems. Ductile fracture during cold working processes is well-known to consist of void initiation at inclusions followed by growth and coalescence along planes of maximum shear. In hot working processes, fracture mechanisms are complicated by dynamic structural changes at high temperature and such mechanisms are yet to be elucidated.

In a previous report, a test system was described for the evaluation of fracture at hot working at controlled temperatures and strain rates. The system can perform upset compression and bend tests at temperatures up to 1200°C and strain rates up to 20 sec⁻¹. In addition, a quenching apparatus has been devised which permits locking in of the hot worked metallographic structure for determination of mechanisms of high temperature fracture.

Since fracture in complex alloy systems is complicated by the large number of phases present, it is useful to start by examining a simple, single-phase material and then increasing the complicity of the alloy and fracture mechanisms. For this purpose, a 35 Co, 35 Ni, 20 Cr, 10 Mo alloy was chosen because at temperatures above 900°C, it is single phase fcc. The alloy is also vacuum cast so it has a negligible amount of inclusions to complicate the fracture process. Finally, the alloy also has a very low stacking fault energy (25 erg/cm²) so that it readily undergoes dynamic recrystallization.

The cobalt-nickel alloy, known as MP35, was tested in bending and frictionless compression at temperatures from 1010° to 1205°C, and at strain rates from 0.01 to 10 sec⁻¹. Bend tests were performed to various increments of

deformation to permit tracking of the fracture mechanisms and homogeneous compression tests were performed to monitor the dynamic recrystallization and flow stress behavior of the material.

Fracture testing

Qualitatively, the fracture behaviour of MP35 alloy in plane strain bending can be represented in a matrix of temperature and strain rate, Fig. 1. The total bending strain is 0.6 in each test. At a given temperature, the effect of strain rate in arresting fracture can be seen immediately along each row. The effect of temperature at constant strain rate can be assessed from the vertical columns. Note that two regions are nearly free of surface cracking: one at the low temperature, high strain rate corner and the other at the high strain rate, high temperature corner on Fig. 1.

Flow Stress Measurements

The flow stress as a function of strain, strain rate and temperature was measured by performing constant strain rate, isothermal, homogeneous compression tests on cylinders. Combinations of strain rates and temperatures similar to those used for the bend tests were selected. Flow stress curves for the strain rates of 0.05, 1 and 10 sec⁻¹ are presented in Fig. 2, 3, and 4.

The peak followed by a drop in flow stress indicates that the MP35 exhibits extensive dynamic recrystallization over the range of temperatures and strain rates investigated. The concurrent very limited capacity for dynamic recovery is also apparent. This behaviour is consistent with its low value of the stacking fault energy. That is to say, the alloy first work hardens very rapidly with very little dynamic recovery taking place. When the critical strain for dynamic recrystallization is achieved, it undergoes the characteristic softening until the steady state is reached and the flow stress remains constant.

Metallographic Results

Optical metallography of sections of the bend specimen was adopted as the main tool to characterize the structure. In general, sections parallel to the plane of flow at mid-breadth of the specimen were examined, both unetched and etched. Figure 5 is a typical section of a well developed crack, unetched. The 90° change in direction of the cracks is typical of well developed cracks, following lines approximately at 45° with the free surface. Figure 6 shows etched sections of specimens bent at 1175°C, and at strain rates of 0.01, 0.1, 1 and 10 sec⁻¹. This figure should be examined in conjunction with Fig. 7, which shows the pertinent flow stress data at 1175°C as a function of strain rate. In this plot, the maximum strain achieved in bending (0.6) has been indicated by the vertical dashed line.

Two things are apparent. First, the amount of cracking diminished strikingly as the strain rate increases, as observed previously in Fig. 1. Second, the structure of the matrix also changes with strain rate, in a manner that is consistent with the flow stress data for this temperature. Both specimens deformed at 0.01 and 0.1 show the equiaxed fine grains characteristic of the dynamic recrystallized steady state. It can be readily seen from the flow stress data that the maximum bending strain lies well beyond the onset of the steady state for these strain rates. On the other hand, for the strain rate of 10 sec⁻¹, the maximum bending strain lies before the onset of the steady state, and indeed, a partially recrystallized structure can be observed. For a strain rate of 1 sec⁻¹, an almost fully recrystallized structure can be observed, again consistent with the position of the maximum bending strain with respect to the onset of the steady state.

Mechanics of Plane Strain Bending

It will be noted that plasticity theory establishes that, for the case of plane strain bending, the maximum shear stress develops along lines that start at 45° to the free surface of the specimen, Fig. 8. It can also be established that along these lines the shear strain rate can reach very high values. In other words, plasticity theory allows the possibility of localization of the deformation along certain lines. In the case of plane strain bending, these lines are at 45° to the free surface. Moreover, along these same lines, the shear stresses are maximum.

During bending, the convex surface undergoes tensile stress and strain, and the magnitude of these quantities diminishes toward the mid-plane of the test specimen. On the concave side, the stresses become compressive. In addition, a notch is placed on the concave side to increase the tensile strains achievable on the convex surface.

Microscopic Response and Fracture

From a microscopic point of view, as the bending of the plane strain specimen proceeds at constant temperature and strain rate, the critical strain for dynamic recrystallization will be achieved in the zone of maximum strain being considered. The strain is maximum at the point in the free surface opposite to the punch, and diminishes both outward along this surface and inward along the radial direction. As the critical strain is reached within this zone the new, small, equiaxed dynamically recrystallized grains begin to form along the existing boundaries of the hot worked grains. Grains outside this zone remain hot worked to the strain reached at any particular point. A polished and etched section of a specimen fast quenched at this stage is shown in Fig. 9. Note also that, by chance, some of the old grain boundaries just covered by the new grains will be lying at approximately 45° to the free surface, or along the lines of maximum shear stress.

Consider also a hot worked grain boundary at 45° to the free surface. Just before the new grains nucleate, the level of the maximum shear stress along this boundary is given by the peak in Fig. 7. As the new grains nucleate and cover the boundary, they can only support a level of stress given by the steady state region in Fig. 7. Such an imbalance of the stresses or, in other words, this localized loss of load carrying capacity, is expected to lead to the localization of plastic flow along the slip lines.

Thus, the mechanism of fracture in this particular alloy can be characterized in Fig. 10. Shear stresses during bending are superimposed on regions of localized dynamic recrystallization along prior grain boundaries. The softer, recrystallized grains permit localization of shear, with subsequent generation of voids and cracks.

Initiation of fracture

In order to determine the nature of fracture initiation leading to gross cracking along dynamically recrystallized grains, a series of specimens were bent to strains of 0.2, 0.35, 0.45, 0.55, and 0.60 respectively at a temperature of 1110°C and strain rate of 0.05. The specimen bent to a strain of 0.2 just before the peak strain of 0.25, and fast quenched provided the most useful information. Figure 11 shows that indeed very little dynamic recrystallization has taken place along prior grain boundaries. Also, only a few tiny starting microcracks (long arrow) can be found. More important, considerable subsurface damage in the form of microvoids along grain boundaries (short arrows) can be observed. Higher magnification views of these voids (Fig. 12) showed that they formed only at these grain boundaries just covered by the soft layer of dynamic recrystallized grains. Very few if any of these voids were found along neighboring grain boundaries along hot worked grains at which dynamic recrystallization had not taken place.

No cavities were found at the original boundaries between hot worked grains. Instead extensive cavity formation was found at those grain boundaries at which dynamic recrystallization took place. This is interpreted on the basis of the argument advanced before: The high stresses developed by deforming the hot worked grains are sufficient to promote extensive sliding when the old boundaries are replaced by the soft layer of recrystallized grains.

A final comment on the role of inclusions follows. Although the volume fraction of inclusions is very low, some square shaped inclusions were found, Fig. 13, both along grain boundaries and within the grains. In both cases they lead to microvoid formation at rather low strains (less than 0.2, from the specimen bent to a maximum strain of 0.2 at 1110°C/0.05 sec⁻¹). The inclusions appear to be very hard, since their shape is not altered by deformation. A single one

along a recrystallized grain boundary was found cracked, Fig. 14. This is taken as indicative of a high stress concentration induced by the sliding, as argued before.

Conclusion

A mechanism for the first stage of the fracture process, void nucleation has been described. This occurs by grain boundary sliding induced by dynamic recrystallization. Inclusions play a very minor role due to their negligible volume fraction. The voids at this stage are truly microscopic and their presence does not give a complete explanation of the macroscopic crack observed and their features.

By chance, at certain points in the specimen and at about 45° to the surface, a layer of soft recrystallized grains containing voids will develop. Superimposing on this layer the maximum stress acting along the slip lines (Fig. 10), one obtains a configuration that leads to the localization of the plastic flow along these directions.

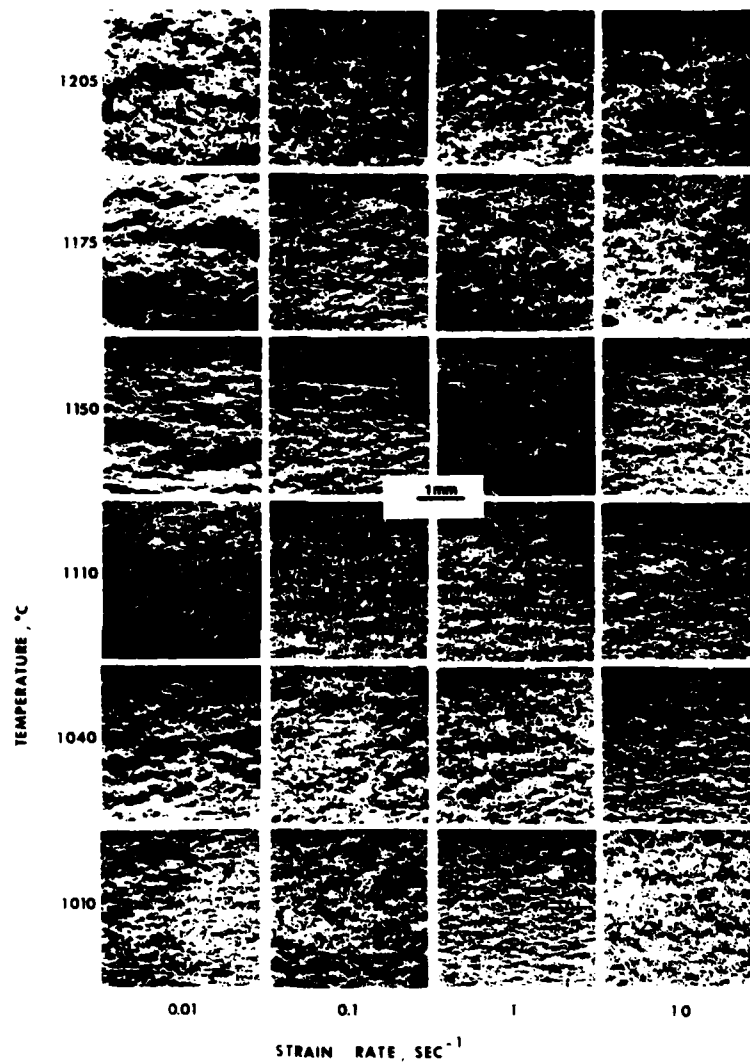


Figure 1. Fracture behavior in plane strain bending of MP35N as a function of (constant) strain rate and temperature. All specimens were bent to a maximum strain of 0.6

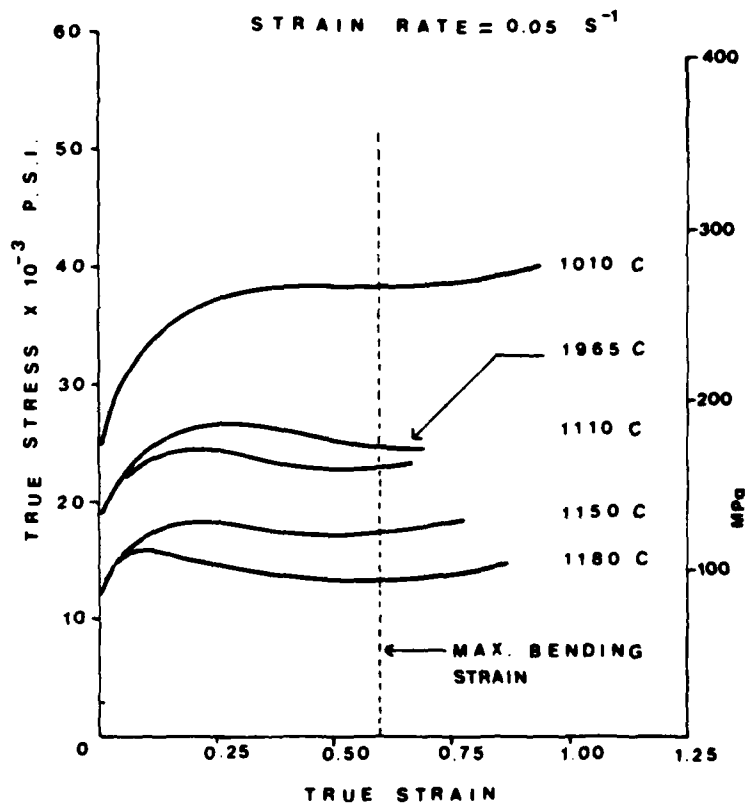


Figure 2. Flow stress of MP35N as a function of temperature at constant strain rate of 0.05 sec^{-1} .

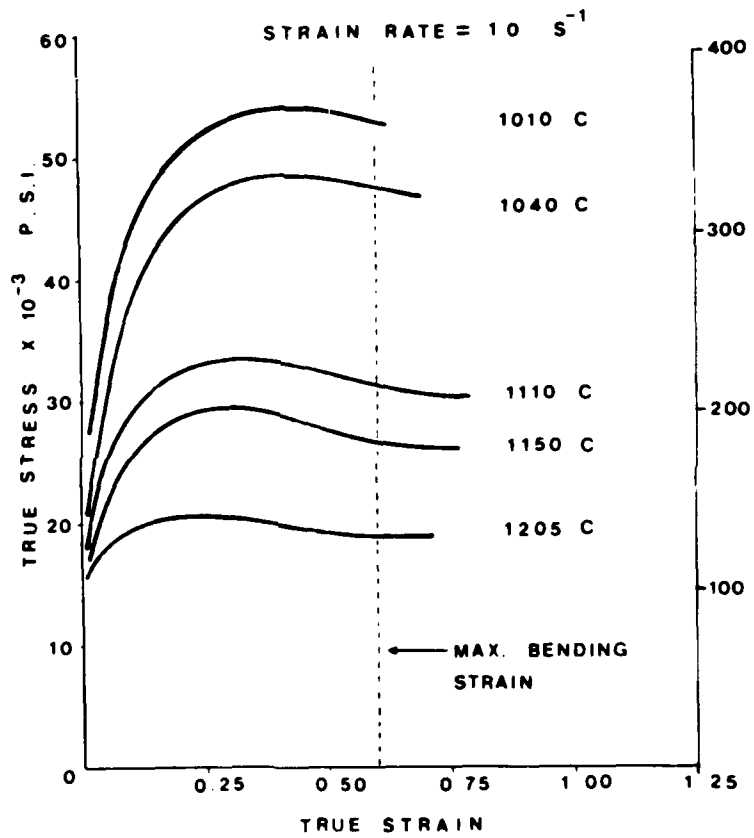


Figure 3. Flow stress of MP35N as a function of temperature at constant strain rate of 1 sec.^{-1}

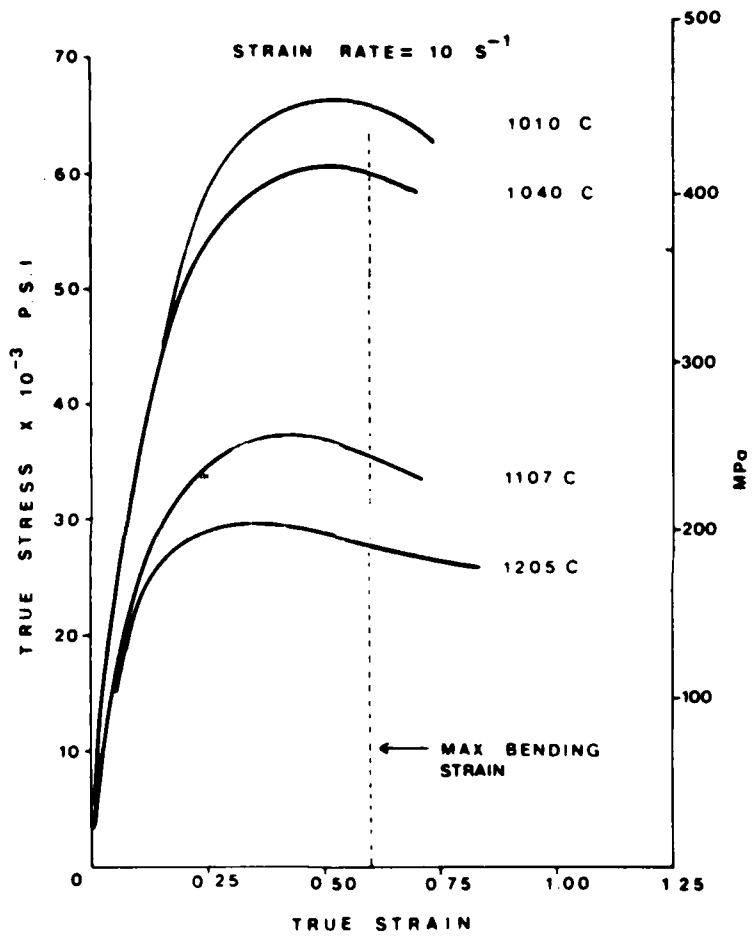


Figure 4. Flow stress of MP35N as a function of temperature at constant strain rate of 10 sec.^{-1}

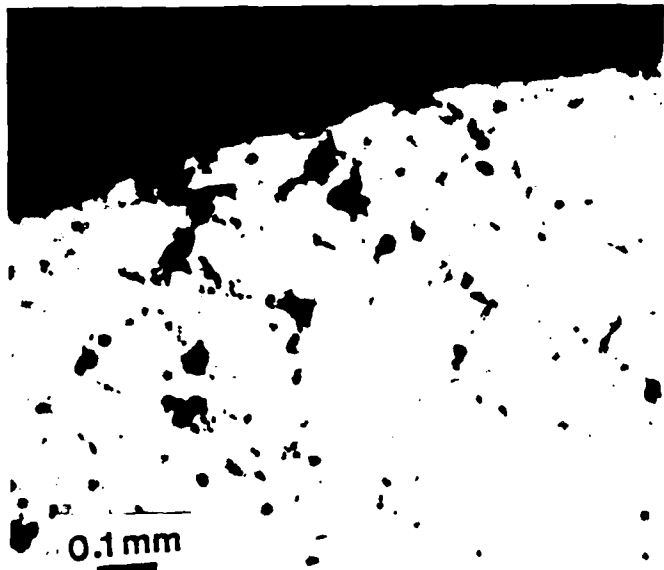


Figure 5. Typical section of a well developed crack, unetched

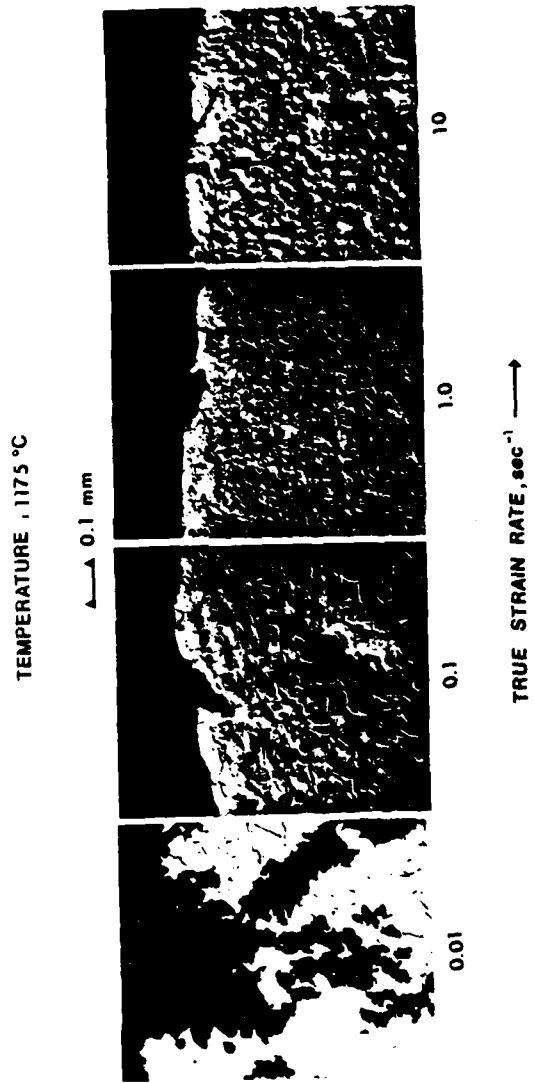


Figure 6. Etched sections of specimens bent at 1175°C as function of strain rate, for the same total maximum strain of 0.6

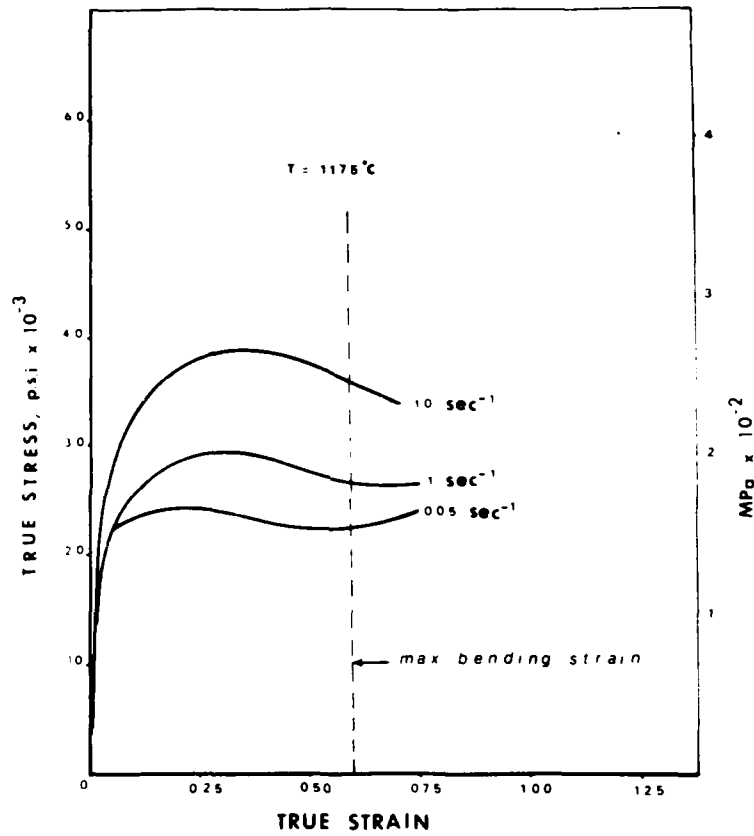


Figure 7. Flow stress of MP35N at 1175°C, as a function of strain rate

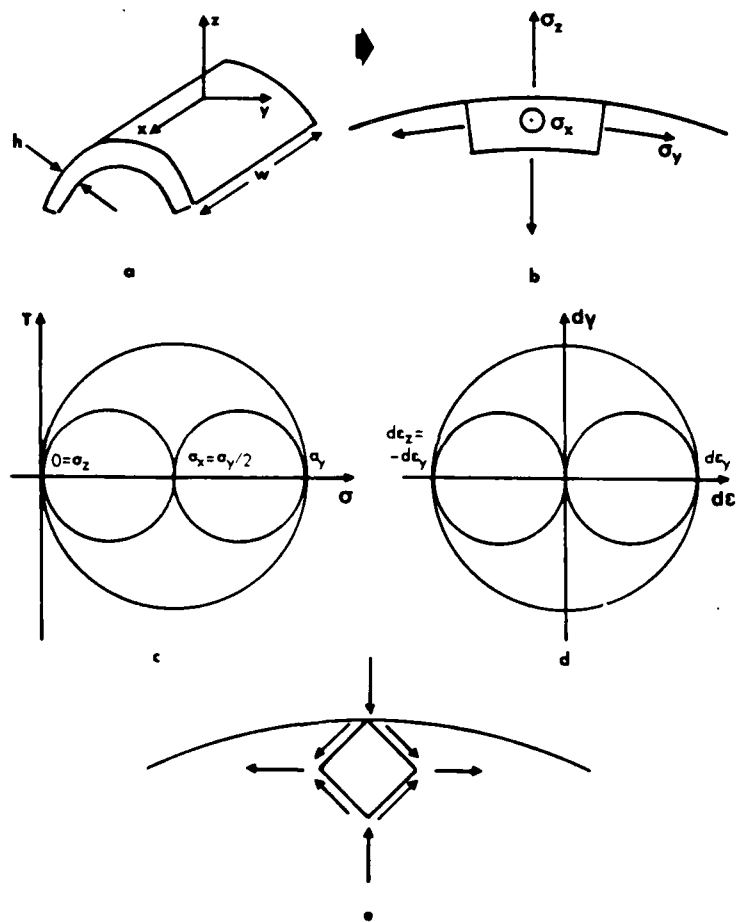


Figure 8. Elementary mechanics of plane strain bending.
 a: specimen ($w/h = 8$) and principal axes, b: definition of stresses, c: state of stress near surface, d: Mohr's diagram for plastic strains, e: illustration of stresses and strains at surface of specimen, valid for deviatoric stresses and total or deviatoric strains

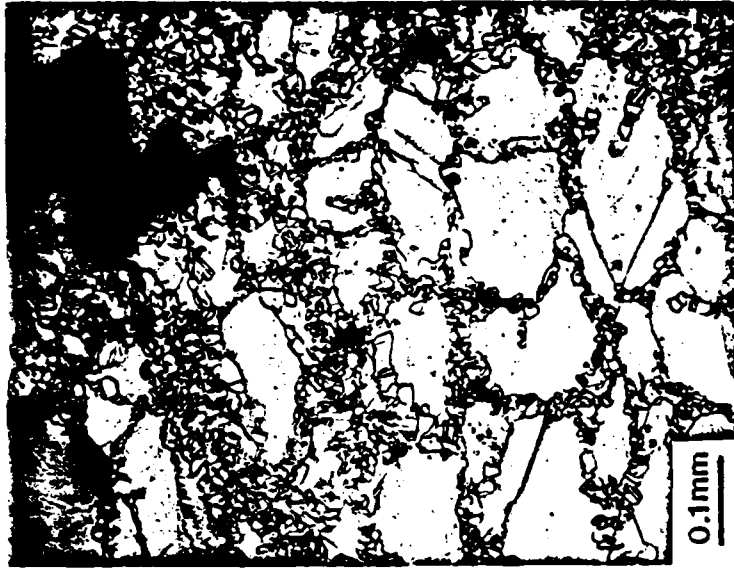


Figure 9. Polished and etched sections of bend test specimens showing dynamic recrystallization along prior grain boundaries and propagation of cracks along these regions.

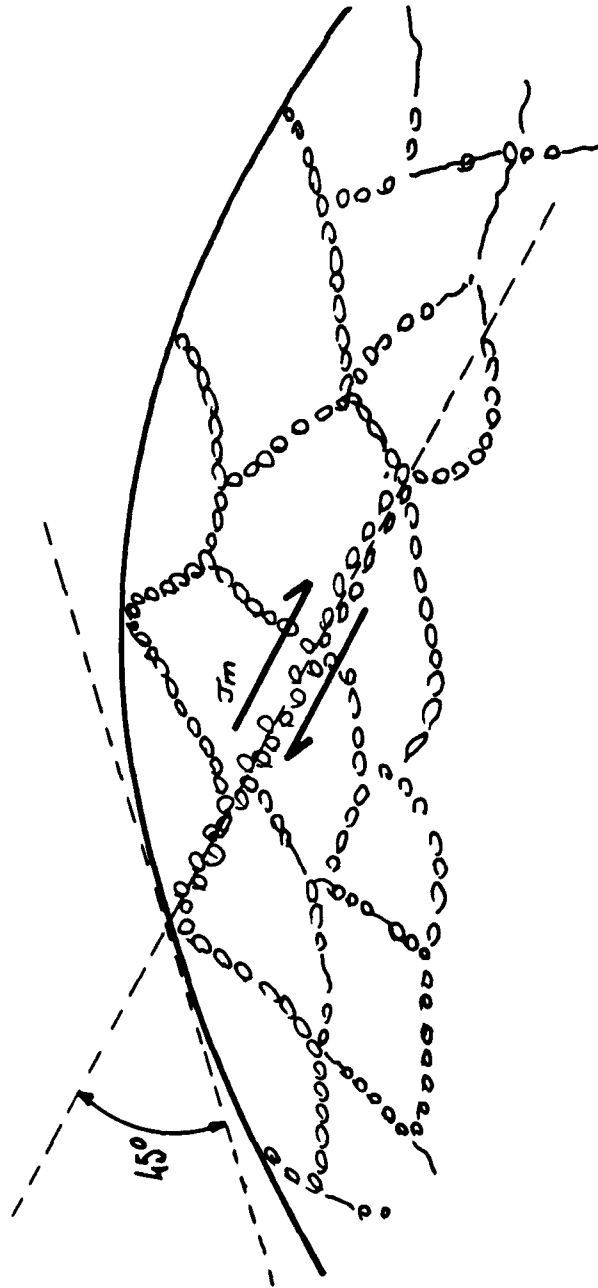


Figure 10. Schematic of section of bending specimen just after the critical strain for dynamic recrystallization is reached at the zone of maximum strain.



Figure 11. Plane strain bending specimen of MP35N bent to a strain of 0.2 just before the peak strain of 0.25 ($1110^{\circ}\text{C}/0.05 \text{ sec.}^{-1}$)



Figure 12a. Detail of void nucleation in MP35N. Same specimen as in Figure 11.

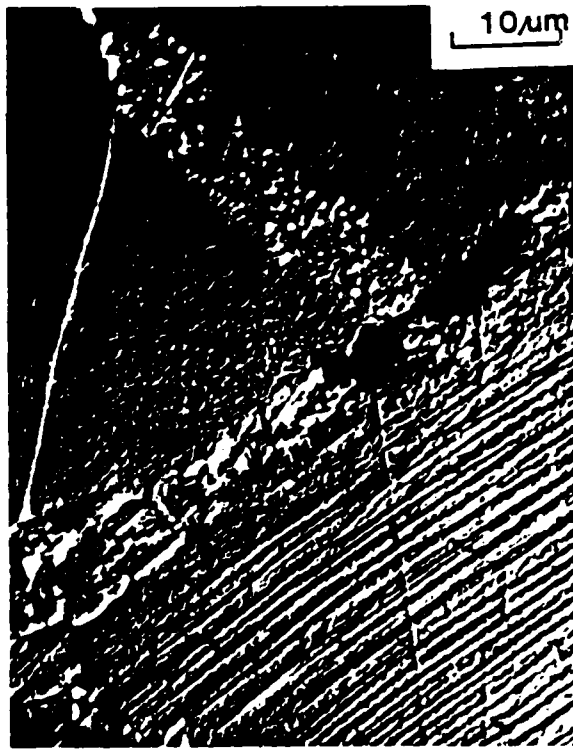


Figure 13a. Detail from Figure 11 (arrow)



Figure 109. Inclusions and void nucleation in MP35N
(1110°C/0.05 sec.⁻¹)

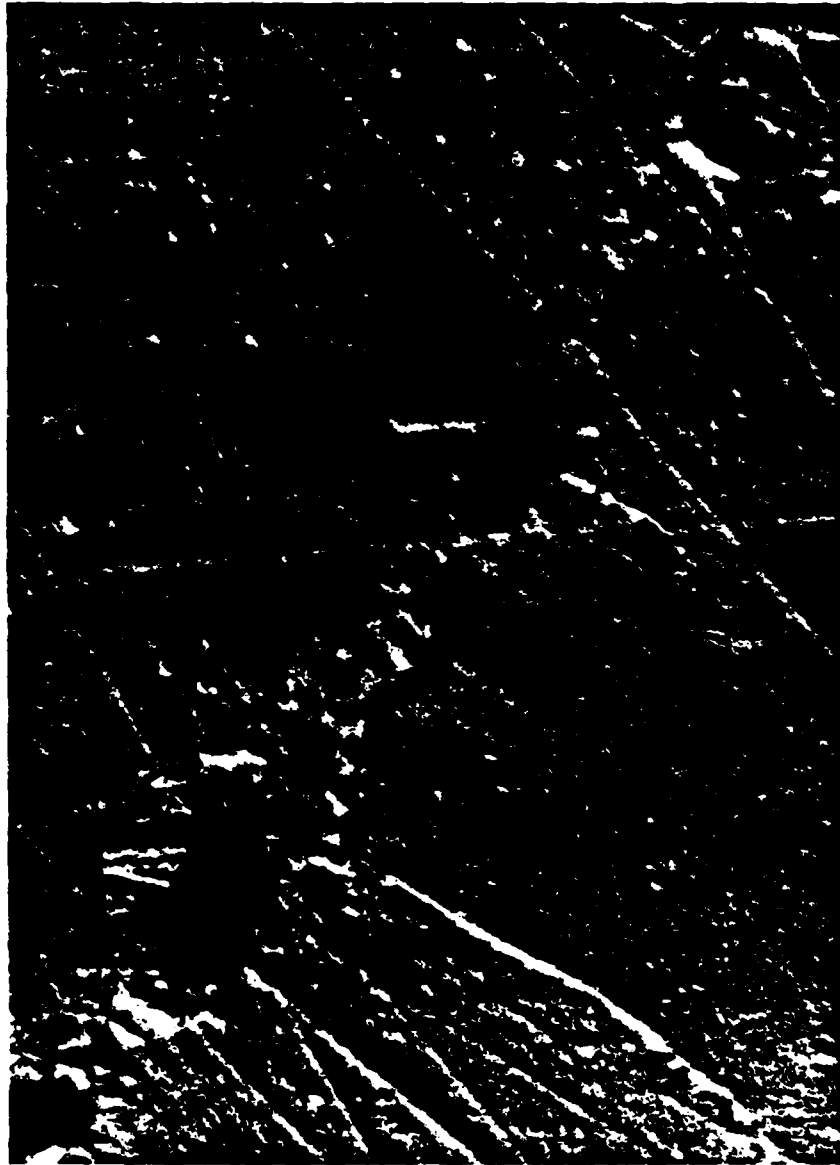


Figure 13b. Inclusion and void nucleation along grain boundary.

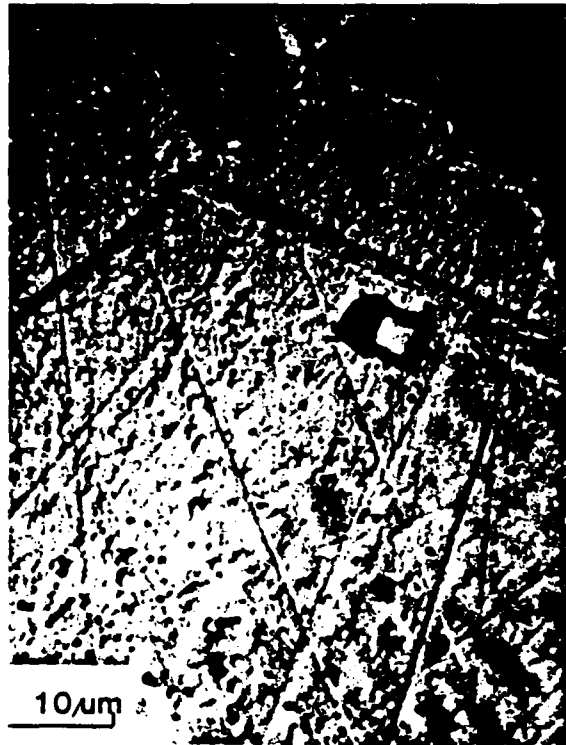


Figure 13c. Inclusions and void nucleation in MP35N
(1110°C/0.05 sec.⁻¹)



Figure 14. Cracked inclusions along recrystallized grain boundary

Appendix 4.11

Evaluation of Nonoxide Silicon Based Ceramics

Dr. Richard L. Porver
Assistant Professor

Science of Fracture Research Project
AFOSR Contract #F 49620-78-C-0101

School of Engineering
University of Pittsburgh
Pittsburgh, PA 15261

STATUS OF RESEARCH

Introduction

It is well known that processing substantially alters the thermal behavior of ceramic materials. Reduction in particle size increases the driving force leading to densification while increasing the specific surface area which leads to increased reactivity with the environment or other phases present. A well known example is the addition of fine quartz to a porcelain body. The same is true for the nonoxide ceramics such as SiC, which have a tendency to react with the environment resulting in tenacious oxide layers even at low temperature. This reaction is extremely difficult to avoid and even more difficult to reverse. Consequently attempts to sinter silicon carbide by reducing the particle size to the submicron level have had only moderate success due to the substantial increase in oxide contamination. Partial sintering results from the isolation of oxide islands within the paths for mass transport. The obvious solution is to introduce a new phase that will react with the oxide to yield a liquid phase at high temperature and increase the sinterability. Unfortunately, the reactions that occur are reversible and lead to a decrease in high temperature creep resistance. By careful choice of the phase(s) added, Carborundum is able to sinter α -SiC to high density while maintaining desirable mechanical properties.

One solution to the problem of utilizing very fine powders that are contaminated with oxide is to reduce the oxide thus exposing a clean, highly active surface of SiC. Our approach, which to the best of our knowledge has not been attempted, has been to expose the contaminated powder to a low temperature plasma (glow discharge) followed by sintering at higher temperatures.

Research Objectives

The objective of this research is to study the influence of the preparation of simple shape products of nonoxide silicon based ceramics on the reproducibility of the final product using fracture mechanics as the major indicator. Efforts are being directed towards consistency of the samples and not towards optimization of the properties. Powders considered in this project include Carborundum's alpha-Silicon Carbide Premix, Lonza Chemical's 1200 mesh black, 1200 mesh green, and UF Carbogran, and Aremco's alpha-Silicon Carbide. Transverse rupture specimens will be cut from larger disks prepared in a traditional dry press/sinter cycle or pressed directly to size. Uniformity is insured by cutting specimens from the larger specimens.

Processing variables to be considered in this work include:

Powder characteristics;

particle size and distribution,
crystallographic modifications of the powders,
particle morphology,
particle surface topography,

Compaction variables;

ultimate applied pressure,
initial (green) density,
binders/lubricants,
delaminations,

Sintering variables;

heating rate,
soak time at temperature,
surface activation using low temperature plasma,
plasma variables (initiation temperature, duration,
type of gas).

The Carborundum premix powder is to be used as a control since it can be sintered to high density yielding excellent mechanical properties. It will be used as received to allow a better comparison of the other powders before and after processing changes.

Status of Research

Characteristics of the Lonza and Carborundum powders were quantitatively determined early in this reporting period. Particle size and distribution were determined by direct measurement using SEM of dispersed powders and is given in Table II of the attached paper. At least 95% of each powder is less than $5\mu\text{m}$ as compared with the Carborundum powder having >98% less than $1\mu\text{m}$. The Carborundum powder is spray dried and as such has excellent flow properties and good compaction characteristics.

Determination of the crystallographic polytype makeup of silicon carbide is complicated due to several overlapping x-ray diffraction lines for the major phases. However, computer analyses at the x-ray intensities allows a semi-quantitative determination of the major polytypes; i.e. α = SiC (15R 6H, 4H) and β -SiC (3C). The results for the Lonza powders are given in Table I, attached paper; the Carborundum powder is 11% 15R, 86% 6H, 1.5% 4H, and 1.5% 3C. This powder is advertised as pure α - SiC but does contain the β - SiC polytype. The Lonza powders have a similar crystallographic makeup which allows for comparisons between all powders as a function of processing.

During the previous reporting period work centered on designing and building an induction vacuum furnace capable of 2100C (Fig. 1). Simple disks (13mm x 5mm) were pressed to 58% density and utilized to isolate problems with the heating schedule, compaction problems, and SEM analysis. Disks were prepared by first adding 3-4% PVA to the powder as a binder/lubricant and pressed uniaxially at 100,000 psi.

During this reporting period experimentation with different levels of binder and proper aging prior to pressing has resulted in disks 13mm and 31mm in diameter being compacted to 60% density using 70-75,000 psi. Delaminations during pressing have been eliminated. Higher initial densities are not desired for two reasons; delaminations during firing, and any enhancement resulting from processing changes are easier to detect with medium to low densities.

The most significant processing variable considered to date is the removal of particle surface contamination by exposure to a low temperature plasma during the sintering. Details are presented in the attached paper.

Current efforts are directed towards a maximization of the plasma activation leading to higher final densities.

It has been demonstrated that the plasma variables are more influential than the powder characteristics, including prior mechanical treatment. Each powder has been pressed to 60% density and exposed to a plasma for 30 min. at temperatures from 800-1700C. Morphological changes, as observed using the SEM, begin at 1585-1600C in as little time as 3 min. Activation on an atomic scale presumably occurs at a lower temperature. Using the SEM only the onset of diffusion resulting from such activation is detected.

Larger disks (31mm x 5mm) have been pressed and sintered using the Brew High Temperature furnace. This allows sintering at 2200C in inert atmospheres or vacuum. Considerable changes are being made to the furnace to allow for the sintering of larger disks (51mm) necessary for preparation of transverse rupture specimens. Disks of Carborundum powder have been sintered to 92% density at 2150C in argon. These will serve as the control for comparisons with the powders activated in the plasma followed by sintering to the same temperature.

The Lonza powders are now being reduced in size using an air-jet-mill grinder to a level comparable with the Carborundum powder. This will minimize grain size effects during fracture testing.

PLASMA ACTIVATED SINTERING OF SiC

Richard L. Porter

Department of Metallurgical and Materials Engineering
University of Pittsburgh, Pittsburgh, PA 15261

I. INTRODUCTION

Sintering of ceramic materials in a glow discharge has been demonstrated to be a viable consolidation process.¹⁻⁴ Rapid sintering rates have been reported in addition to the development of favorable microstructural features.^{1,4} More importantly, a glow discharge plasma may enhance normal sintering by activation of powder surfaces.

The driving force for sintering is directly dependent on the surface energy of the constituent powder. Factors that alter surface energy generally affect the sinterability of the powder. In any powder array the excess surface energy can be lowered by faceting, change in shape, or by the formation of necks between adjacent particles. For an isolated particle, or one isolated by a second phase such as an oxide layer, the surface energy can be further changed by the presence of the oxide or second phase. Non-oxide ceramics such as SiC and Si_3N_4 are difficult to sinter due to a high degree of covalency and the presence of tenacious oxide layers that are thermodynamically stable in an oxygen containing environment.^{5,6} The use of submicron powders increases powder activity but also increases the tendency towards low temperature surface oxidation. Addition of sintering aids to SiC contaminated with oxides layers has been successful in sintering to high densities, most probably due to formation of intergranular liquid phases. It is desired to sinter SiC to

Presented at the 82nd Annual Meeting, The American Ceramic Society, Chicago, IL., April 27, 1980; Basic Science Division, Paper 27-13-80.

high densities without additives since residual phases may affect the high temperature mechanical properties.

Rapid sintering rates of oxide ceramics have been achieved using plasmas.²⁻⁴ In some oxides, partial melting of the surface may lead to a modified liquid phase sintering condition. However, it appears the major cause of enhanced sintering is the rapid attainment of temperatures sufficiently high such that diffusive mass transport mechanisms leading to densification overwhelms those leading to surface changes only. Alternatively, a plasma could be utilized to break up oxide surface layers or segregated contaminants creating a highly active surface. The sintering process is then reduced to that for a pure system having active surface diffusive mechanisms. Plasma activation can be used in combination with conventional heating allowing for better temperature control than sintering in a plasma alone.

The surface condition of any powder is of major importance in the sintering process. Total removal of oxide layers from SiC must be accomplished if the initial stage of sintering is to lead continuously to final densification. It has been demonstrated by Heath and Evans,⁷ Porter,⁸ and Hara and Akechi⁹ that oxide layers or irregular surfaces can create inhomogeneous necks during the very initial stage of sintering. These inhomogenities may be oxide islands or pores which effectively block diffusive mechanisms leading to densification. Addition of sintering aids such as B₄C or C to SiC contaminated with oxide¹⁰ layers may result in binary or ternary liquid phases at the neck surfaces rather than within the neck, and therefore enhanced sintering behavior.

This paper will describe the sintering of pure α -SiC powders activated by a plasma during the early stages of densification.

II. EXPERIMENTAL PROCEDURE

Three grades of commercial SiC were investigated; denoted as 1200 mesh black*, 1200 mesh green*, and ultra-fine*. X-ray diffraction (XRD) of the as-received powders indicated predominantly α -SiC with 6H the major polytype (Table I). The particle size distribution of dispersed powders is given in Table II. A substantial fraction of each is submicron with the ultra-fine containing the highest fraction of fines and exhibiting the best compaction characteristics.

Powder compacts were prepared by first adding 2-3% polyvinyl-alcohol as a binder and aged for four days prior to pressing. Compacts 1.25 cm D X 0.64 cm were pressed uniaxially at 800 MPa yielding a green density of 58-60% of theoretical.

The plasma activated sintering (PAS) apparatus is shown schematically in Fig. 1. A graphite susceptor serves as sample support and heat source with a W-W26Re thermocouple passing through the susceptor base. Alumina wool⁺, held in place by 0.005" Mo foil, serves to insulate the fused quartz furnace tube. Both end plates are aluminum and the bottom plate is water cooled.

With a pellet in place, the unit was evacuated to 5 μ m and held overnight. Heating slowly to 500-600C accomplished binder burnout followed by a more rapid temperature increase (40-50C/min.) to 1000C. A glow discharge was initiated by bleeding in Ar which when coupled with the field, ignited the plasma. Following a 5-6 min. hold at 1000C with discharge, the Ar was turned off and the temperature raised rapidly to the sintering temperature, 1850-1950C. Total elapsed time was 50 min. from room temperature.

*Lonza Chemical Company, Fair Lawn, NJ

+Saffil, ICI Americas, Wilmington, DE

At the sintering temperature a second discharge was initiated lasting up to 10 min. Following the hold at the sintering temperature, power was turned off and the entire assembly allowed to cool under vacuum. Due to the intense radiation at the sintering temperature, it was difficult to observe the glow discharge directly. However, an induced potential is present across the top plate and grounded graphite susceptor and monitoring of this potential allows for detection of the discharge.

Macroshrinkage was determined from height and diameter measurements of the pellets and microshrinkage from SEM observations of fractured surfaces.

III. RESULTS

The microstructure of the black 1200 mesh SiC sintered at 1900C without and with plasma activation is shown in Fig. 2(a) and 2(b) respectively. Without the plasma the particles have retained the as-received angular morphology. Although macroshrinkage (determined as change in pellet dimensions) was 0.2%, little if any microshrinkage occurred as evidenced by the lack of necks between particles. In contrast, when sintered with the discharge the morphology is altered substantially. The sharp, angular particles have become rounded and smooth and, more importantly, substantial neck growth has occurred. Measured macroshrinkage has increased from 0.2 to 1.0% and local x/a ratios are in the range 0.2 to 0.5.

Increasing the sintering time without plasma activation resulted in crystallographic faceting as shown in Fig. 3 for 1200 mesh black SiC. The faceting reduces the surface free energy and therefore the available driving force for densification and no microshrinkage is observed. It is apparent from Fig. 3 that the hexagonal polytypes are the predominant phases present at 1900C.

When the same material is sintered for longer periods of time in addition to using the plasma as described above, the faceting is suppressed and, as expected, significant microshrinkage occurs between the smooth, rounded particles (Fig. 4).

The 1200 mesh green SiC sintered with and without plasma activation exhibits microstructural features similar to that of the black SiC. Some degree of crystallographic faceting has occurred and necks have formed without the plasma activation (Fig. 5(a)). The 1200 mesh green is a finer material having 60% of particles less than 1.0 μm diameter and therefore would be expected to sinter more than the coarser black material. When sintered with plasma activation, (Fig. 5(b)), the morphology was altered as it was with the 1200 mesh black. Substantial neck growth occurred with high local x/a ratios (>0.4) and several areas where smaller particles have coalesced with the larger particles. Although the microshrinkage is high in localized areas, little macroshrinkage occurred as would be expected at 1900C.

The microstructure of the ultra-fine SiC sintered at 1900C for 30 min. without a plasma activation period exhibits faceting similar to that in the 1200 mesh black, Fig. 3, but to a lesser extent, Fig. 6(a). With the plasma activation, surface alteration occurred, Fig. 6(b), with substantial neck growth and areas of high microshrinkage.

X-ray diffraction analyses of all the materials sintered with and without plasma activation indicated mainly α -SiC polytypes, i.e., 15R, 6H, and 4H. This is consistent with published data indicating that the cubic β -SiC, 3C, becomes unstable at $T \geq 1900\text{C}$.

IV. DISCUSSION

Exposure to a glow discharge during sintering significantly altered the crystallographic makeup as compared to the material sintered without the discharge. XRD of the material sintered without the discharge indicated an

increase in the 15R and 6H polytype and a decrease in the 4H and 3C. When sintered with the discharge, the 15R decreased to less than that in Table I, 3C further decreased to 0%, while the 4H and 6H increased to a greater level than in Table I. Phase transformations in SiC are not well understood and many depend strongly on impurities and the atmosphere. In this work, the presence of a glow discharge would primarily affect the surface indicating that the polytype transformations are dependent on surface activity and structure.

Silicon carbide, like other non-oxide ceramics, is thermodynamically unstable in an oxygen containing environment with surface contamination by tenacious oxide layers the most common result.^{5,6} Total removal of such films and layers is difficult but necessary if normal sintering is to proceed leading to densification. In this work, the as-received SiC powders were sintered without a glow discharge with no attempt made to clean the surfaces or destroy the oxide contamination. Very little shrinkage occurred even on a microscopic level with the exception of the 1200 mech green SiC (nominally purer than the black SiC). This is consistent with observations by others that SiC is difficult to sinter without sintering aids.

Crystallographic faceting is observed in the sintered powders indicating significant surface or vapor transport mechanisms. It also suggests an incubation time for faceting greater than 3 minutes at 1900C. As the contaminated powder compacts are heated in vacuum, the surface energy will have a tendency to lower via faceting or sintering, i.e. reduction in surface free energy. Simultaneously, the oxide layers experience a greater tendency towards volatilization with increasing temperature. Without the glow discharge, the volatilization will be delayed allowing the faceting to proceed, hence reducing the surface energy

and lowering the available driving force for densification. Even partial volatilization of the oxide films could disrupt normal sintering by creating islands of oxides within small necks created by surface transport. Blockage of the transport paths leading to shrinkage would allow further lowering of surface energy via faceting.

When exposed to a glow discharge at a temperature lower than the sintering temperature, it is believed that the surfaces are effectively cleaned by the impinging ions, which would allow volatilization of the oxide layers. The particle surfaces would be left in a highly active state with a considerable defect density. Adjacent particles could then lower their surface energy by surface transport phenomena leading to neck formation. Surface transport is obviously high as verified by the rounding of the particles. The resulting necks, although not sufficient to cause densification, do provide homogeneous regions for bulk diffusive mechanisms, volume or grain-boundary diffusion, which lead to densification.

V. CONCLUSIONS

Plasma activated sintering (PAS) has been shown to provide apparently clean, active surfaces in SiC powder compacts. These active surfaces have a higher tendency towards surface energy reduction via diffusive sintering, leading to densification, than powders sintered without a glow discharge.

Although experiments have been conducted only with low density compacts to eliminate plasma permeability problems, it is expected that higher green densities could be used.

ACKNOWLEDGEMENTS:

The author thanks J. R. Blachere for many useful discussions and Mr. E. Hewitt for experimental assistance in designing and operating the induction furnace.

REFERENCES

1. D. L. Johnson and R. A. Rizzo, "Plasma Sintering of β "-Alumina, Am. Ceram. Soc. Bull., 59 [4], 467-68, 472 (1980).
2. G. Thomas, J. Freim, and W. Martinsen, "Rapid Sintering of UO_2 in a Glow Discharge," Trans. Am. Nucl. Soc., 17, 177 (1973).
3. C. E. G. Bennett, N. A. McKinnon, and L. S. Williams, "Sintering in Gas Discharges," Nature (London), 217, 1287-88 (1968).
4. G. Thomas and J. Freim, "Parametric Investigation of the Glow Discharge Technique for Sintering UO_2 ," Trans. Am. Nucl. Soc., 21, 182-83 (1975).
5. A. J. Moulson, "Reaction-bonded silicon nitride; its formation and properties," J. Mat. Sci. 14, 1017-51 (1979).
6. A. L. Stuijts, "Basic and Practical Aspects in Sintering Nitrogen Ceramics," in Nitrogen Ceramics, F. L. Riley, ed., Noordhoff-Leyden, 331-50 (1977).
7. P. J. Heath and P. E. Evans, "Sintering, fracture, and oxide films", J. Mat. Sci., 9, 1955-60 (1974).
8. R. L. Porter, "The Effects of Surface Topography During the Initial Stage of Sintering," in Sintering Processes, Vol. 13, Materials Sci. Res., Kuczynski, ed., Plenum, 129-34 (1980).
9. Z. Hara and K. Akechi, "Structure of Sintering Necks in Silver Powder Compacts," *ibid.*, 121-27.
10. P. T. Shaffer, "The SiC Phase in the system SiC-B₄C-C," Mat. Res. Bul, 4 [3], 213-19 (1969).
11. J. M. Bind, "Phase Transformations During Hot-Pressing of Cubic SiC," *ibid.*, 13, 91-96 (1978).

TABLE II. PARTICLE SIZE DISTRIBUTION

Size Range	1200 Mesh (Black)	1200 Mesh (Green)	Ultra-fine 1-3 μm
>1 μm	22%	59%	65%
1-5	65	36	34
5-10	10	4	>1
10-15	2	>1	>1
>15	>1	>1	>1

TABLE I. X-RAY DIFFRACTION ANALYSIS OF SiC POWDERS*

SiC Polytype	1200 Mesh (Black)	1200 Mesh (Green)	Ultra-fine 1-3 μm
<u>α-SiC</u>			
15R	10 w/o	5 w/o	13 w/o
6H	71	81	74
4H	10	5	11
<u>β-SiC</u>			
3C	9	9	\sim 2

*Lonza Chemical Co., Fairlawn, NJ

- Fig. 1 Schematic of plasma activated sintering apparatus.
- Fig. 2 Microstructure of 1200 mesh black SiC sintered in vacuum for 3 min. at 1900C; (A) without plasma activation, and (B) with plasma activation for 6 min. at 1000C and 3 min. at 1900C.
- Fig. 3 Microstructure of 1200 mesh black SiC sintered in vacuum for 9 min. at 1900C without plasma. Note the prevalence of hexagonal morphology.
- Fig. 4 Microstructure of 1200 mesh black SiC sintered in vacuum for 30 min. at 1900C with plasma activation. Faceted surfaces are not present and significant morphological alteration has occurred.
- Fig. 5 Microstructure of 1200 mesh green SiC sintered in vacuum; (A) for 6 min. at 1895C without plasma activation, and, (B) for 10 min. at 1900C with plasma activation.
- Fig. 6 Microstructure of ultra-fine SiC sintered in vacuum for 30 min. at 1900C; (A) without plasma activation, and, (B) with plasma activation.

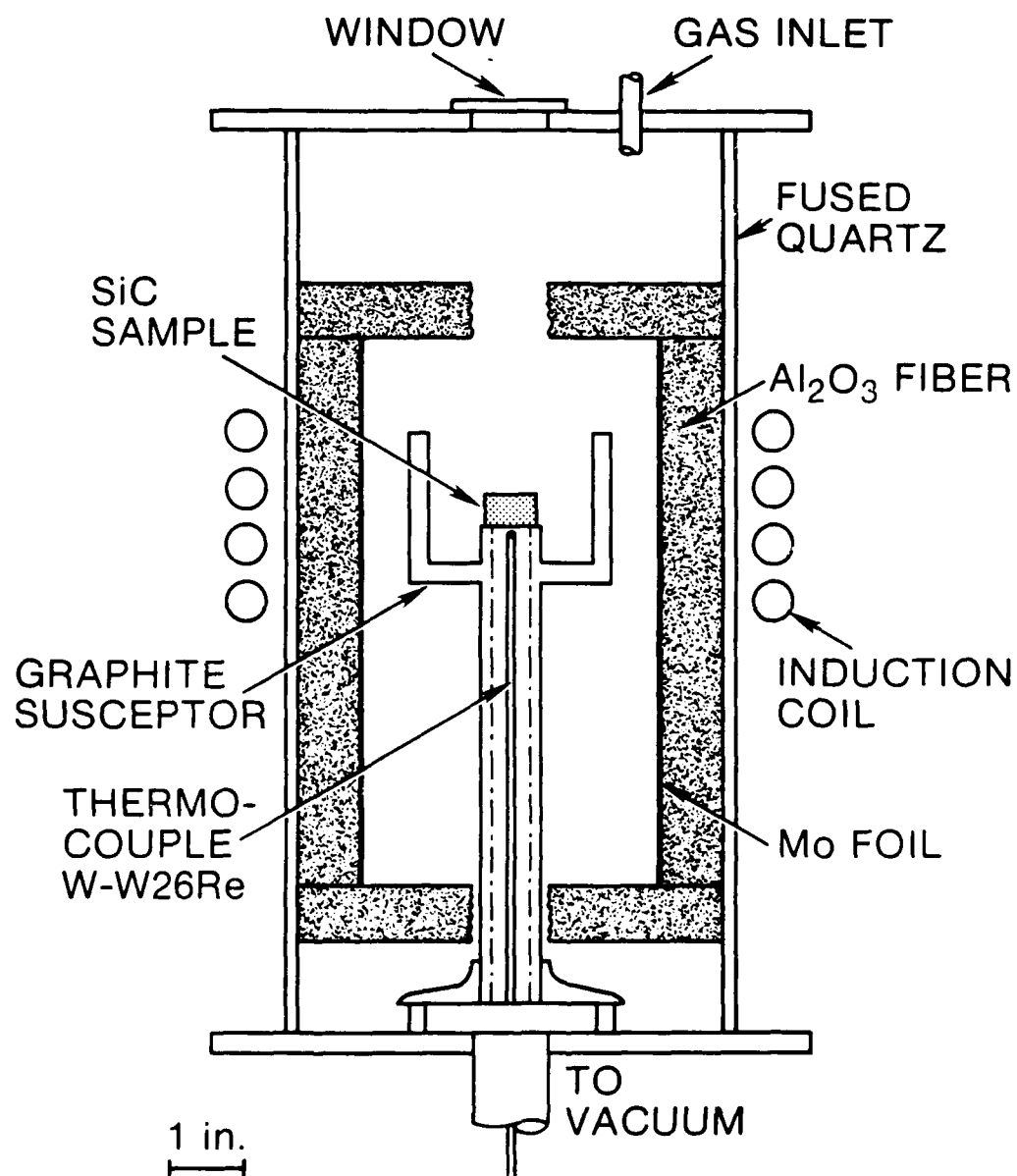


FIG. 1 Plasma Sintering Apparatus

AD-A093 417

PITTSBURGH UNIV PA SCHOOL OF ENGINEERING
SCIENCE OF FRACTURE.(U)
OCT 80 M L WILLIAMS, C C YATES
SETEC-SF-80-048

F/6 20/11

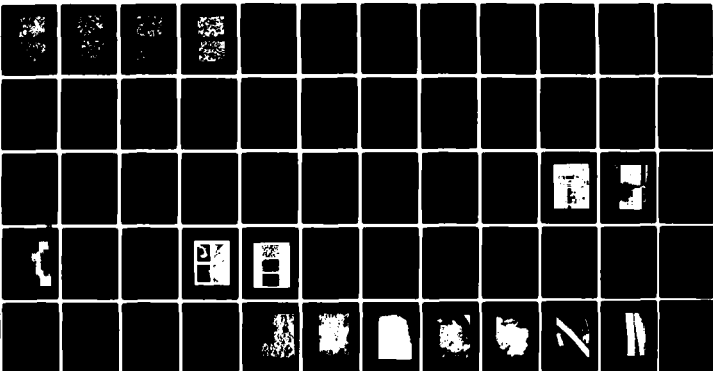
UNCLASSIFIED

AFOSR-TR-80-1322

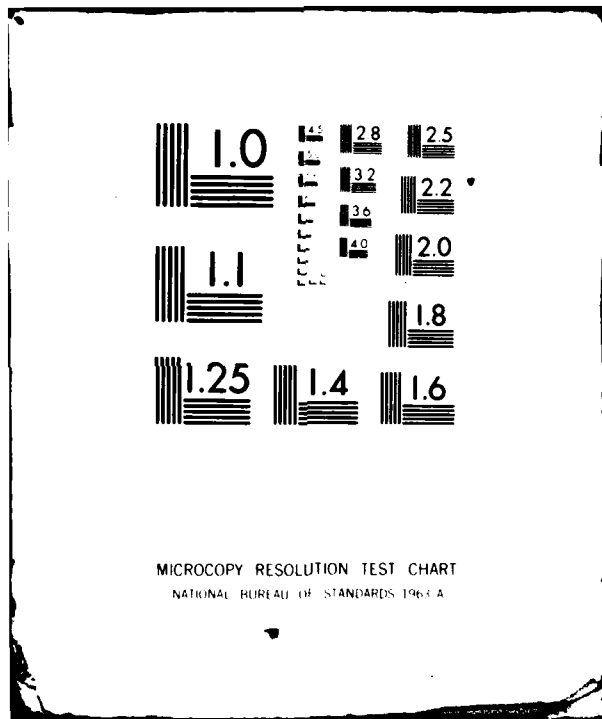
F49620-78-C-0101
NL

3-3

20-11



END
DATE
FILMED
2-81
DTIC



MICROCOPY RESOLUTION TEST CHART
NATIONAL BUREAU OF STANDARDS 1963 A

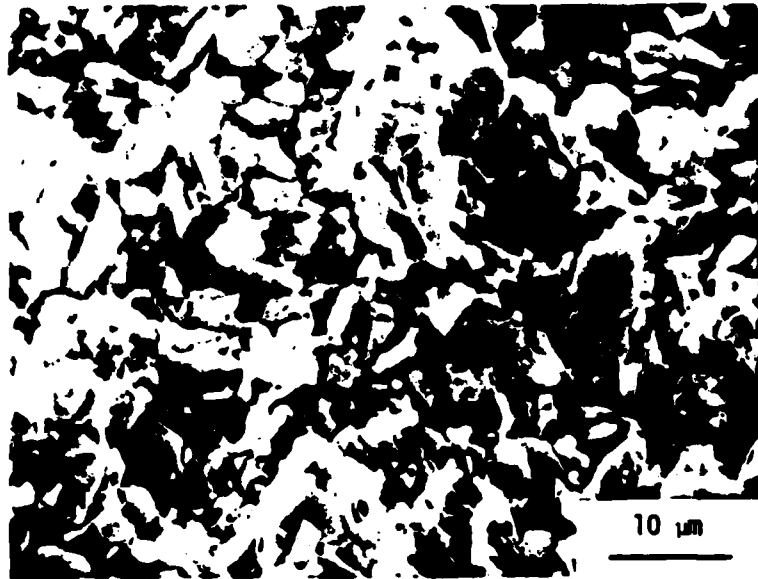


FIG. 2 (A) SiC (1200 Mesh Black) SINTERED 3 MIN. AT 1900C WITHOUT GLOW DISCHARGE

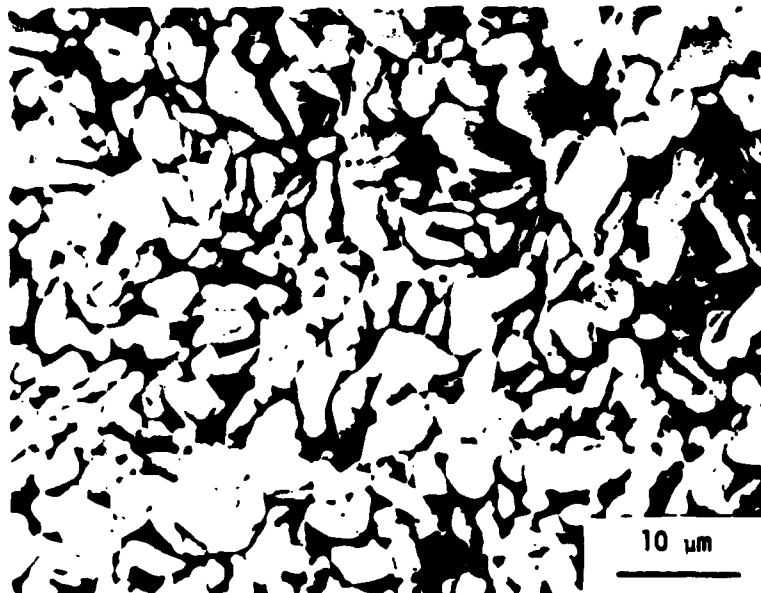


FIG. 2 (B) SiC SINTERED 3 MIN. AT 1900C WITH Ar GLOW DISCHARGE

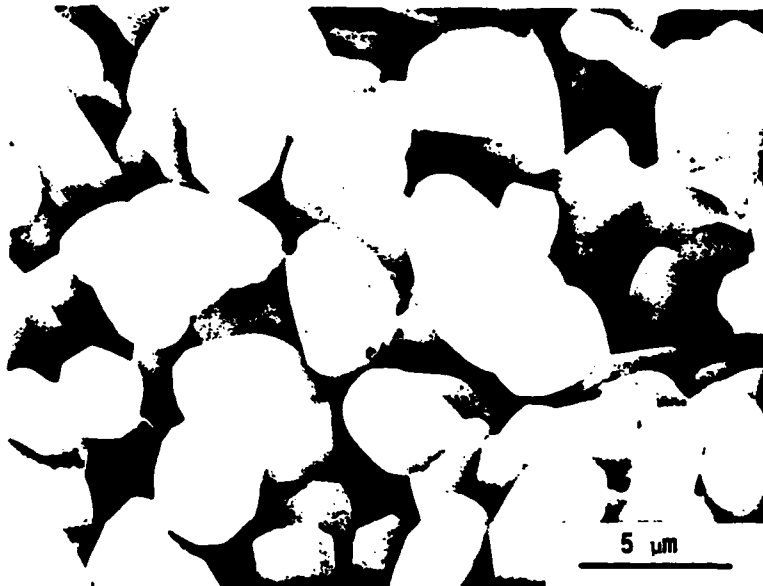


FIG. 3 SiC (1200 Mesh Black) SINTERED 9 MIN. AT 1900C
WITHOUT GLOW DISCHARGE

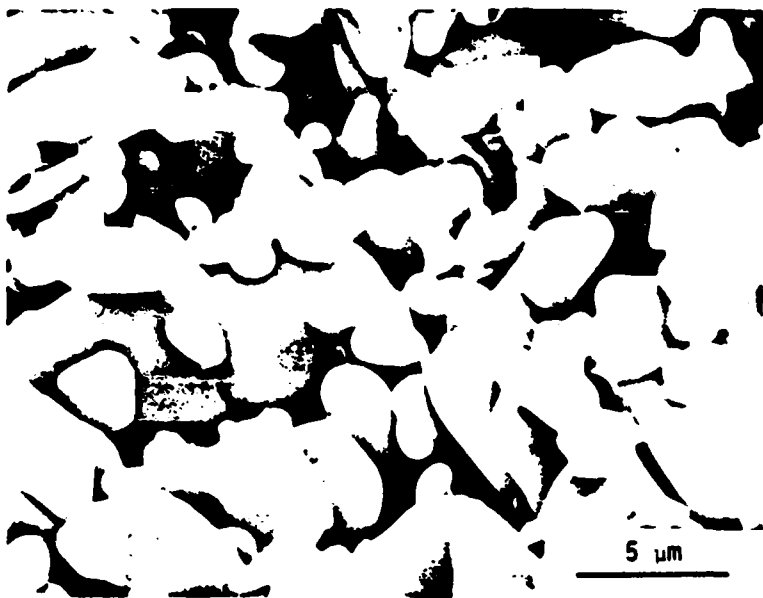


FIG. 4 SiC SINTERED 30 MIN. AT 1900C WITH Ar GLOW DISCHARGE



FIG. 5(A) SiC (1200 Mesh Green) SINTERED 6 MIN. AT 1895C WITHOUT GLOW DISCHARGE

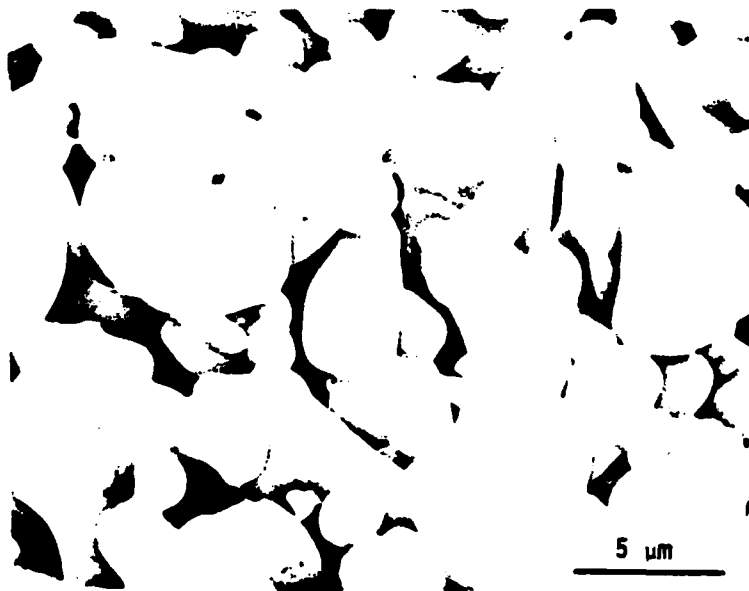


FIG. 5(B) SiC SINTERED 10 MIN. AT 1900C WITH Ar GLOW DISCHARGE

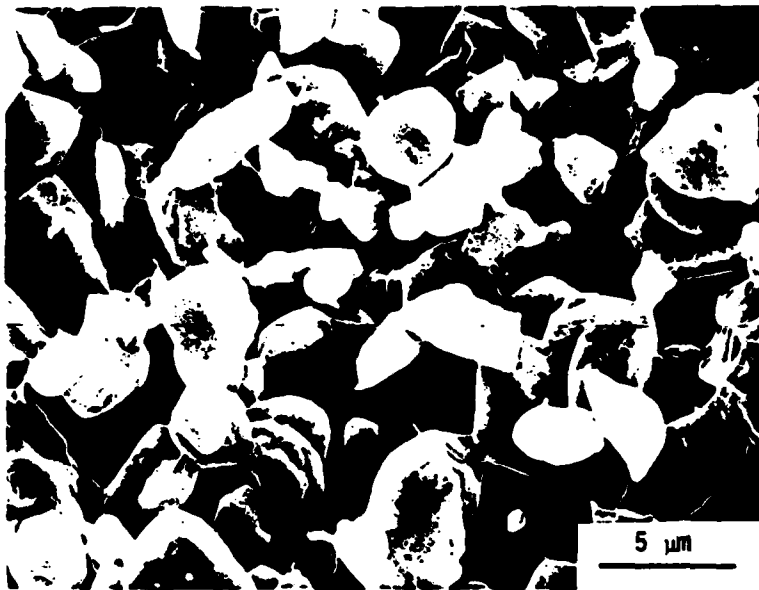


FIG. 6(A) SiC (Ultra-fine) SINTERED 30 MIN. AT 1900C
WITHOUT GLOW DISCHARGE



FIG. 6(B) SiC SINTERED 30 MIN. AT 1900C WITH Ar GLOW DISCHARGE

Appendices 5.0

Subcontracts

- 5.1 A Fundamental Study of the Relationships of Polymer Structure and Time-Dependent Fracture.

Institute of Polymer Science
University of Akron

- 5.2 Numerical Studies of Crack Problems in Finite Elasticity.

University of Texas

APPENDIX 5.1

THE UNIVERSITY OF AKRON
INSTITUTE OF POLYMER SCIENCE

Annual Report to
The University of Pittsburgh
1 August 1979-31 July 1980

STRUCTURE-PROPERTY RELATIONSHIPS
FOR TIME-DEPENDENT FRACTURE OF POLYMERS

F. N. Kelley
P. Dreyfuss
B. Swetlin
L. Su

TABLE OF CONTENTS

	Page
I. EPOXY NETWORKS.	1
Introduction.	1
Network Characterization.	3
Time-Dependent Fracture Characterization.	5
Mechanical Loss Characterization.	6
Fatigue Crack Propagation	7
II. MODEL INHOMOGENEOUS GLASSY NETWORKS	8
Materials	9
Procedure	9
III. RUBBERY NETWORKS.	15
Characterization.	16
Fracture Studies.	20
Discussion.	21
IV. THERMAL EXPANSION MEASUREMENTS.	22
Apparatus	22
Results	23
Discussion.	24
REFERENCES	26

Page *

Original page numbers for subcontract report retained to permit reference to it as a separate report.

TABLES

	Page
1. Modification of Resins	12
2. Molding Experiments.	13
3. Characterization of Networks for Fracture Studies. .	17
4. Characterization of Samples TB ₁ , TB ₂ , TS ₁ and PB ₁ . .	18

ABSTRACT

Rubbery and glassy network polymers have been prepared and characterized by various physical and chemical methods. Fracture studies have been undertaken on these polymers using a range of loading rates and temperatures. Initial efforts to describe local inhomogeneities in cured epoxy resins by electron microscopy have been reasonably successful. The feasibility of model inhomogeneous glassy network polymers with precisely controlled structure has been established, with the intent of comparing the fracture behavior of these materials with analogous epoxy structures. Also, a series of end-linked polybutadienes and poly(butadiene-styrene) copolymer networks have been prepared and characterized. These polymers provide known variations in cross-link density and backbone flexibility. Viscoelastic properties of some of the rubbery polymers have been determined at both the University of Akron and the University of Pittsburgh in dynamic and creep experiments. Correlation of mechanical loss with the time dependent fracture energy in each material system is underway.

I. EPOXY NETWORKS

Introduction

The objective of this research is the quantitative correlation of possible microphase heterogeneity with time-dependent behavior, including fracture. This investigation has followed several paths, all of which are linked by a unifying concept; a relationship exists between microstructural variables, mechanical loss characteristics, and time-dependent fracture energy. Most of the effort has been spent developing the diverse techniques and analyses required for a successful completion of this project.

Network Synthesis

Variations in reactant stoichiometry and process history are expected to produce measurable variations in structural heterogeneity. Considerable latitude in thermal processing variation is possible using systems with low initial viscosities and long gel times.

Since fracture and fatigue properties are particularly sensitive to specimen defects, the production of void-free castings has been a high priority objective. It has been found that the degree of care required to produce defect-free samples is determined mostly by the reactant system's viscosity.

Aliphatic amine cured systems, such as triethylene tetramine/Epon 828, gel in a relatively short period of time at room temperature. These systems have viscosities greater than 50 poise

at room temperature. In addition, the viscosity increases as the reaction proceeds to the gel point. Entrapped air produced during reactant mixing must be removed under vacuum. After debulking, simply pouring the mixture into a mold appears to produce void-free castings. However, inspection of these castings with a polarized light microscope reveals that a large number of voids are present which cannot be detected with the unaided eye. It has been found that these defects can be eliminated by mold filling under vacuum. This extra care would be unnecessary if the viscosity could be lowered by increasing the reaction temperature; however, the pot life is considered to be too short even at room temperature. These same systems can be handled quite easily without any special precautions (at room temperature) if the mixture contains a non-reactive diluent such as dimethyl sulfoxide. Void-free pre-swollen castings have been prepared by pouring the diluted reaction mix into molds, without the need of any vacuum.

In contrast, the aromatic amine cured systems, such as methylene dianiline/Epon 828, have long pot-life at elevated temperatures and are therefore particularly easy to work with. No special precautions are required to produce void-free specimens with these low viscosity mixtures. With the above combination, for example, the reactants are mixed at 60°C and poured directly into preheated molds. Air entrapped during the pouring step quickly dissipates.

Two closed mold configurations have been used. One has permitted the casting, in vacuum, of flat plates of dimensions

4" x 6" x 1/4" using the vertical position shown in Figure 1. The second mold, shown in Figure 2, allows the casting of four compact tension specimens at one time. Both molds are teflon coated. In addition, the white posts seen in Figure 2 are produced from teflon rod.

Network Characterization

The average molecular weight between crosslink points, M_c , is typically evaluated in elastomers via stress-strain data plotted in a Mooney-Rivlin fashion.¹ Since epoxy resins have high glass transition temperatures, and this method requires data obtained in the "rubbery" regime, network degradation is of some concern. A significant achievement has been the preparation of epoxy networks in the presence of a high boiling diluent, resulting in a pre-swollen material with T_g near room temperature. A typical Mooney-Rivlin plot of an epoxy network synthesized in the presence of dimethyl sulfoxide is seen in Figure 3.

The Mooney-Rivlin equation is based on the rubber elasticity theory for networks composed of statistically distributed and freely rotating Gaussian chains. In the example shown in Figure 3, the M_c value of ~ 615 g/mole, corresponds to two monomer segments of DGEBA between crosslinks, or less than 30 main chain atoms between junction points. Over 40% of the monomer molecular weight resides in the bulky benzene rings, which reduce network chain flexibility and rotation.

Rubber elasticity theory cannot be expected to apply to such a tight network composed of short strands with low flexibility. Yet, the M_c shown in this example is not too far removed from the theoretically determined M_c of ~ 380 g/mole.

T_g is being measured via DSC and dilatometry. A typical dilatometric curve is seen in Figure 4 for a network synthesized in the presence of dimethyl formamide.

Structural Heterogeneity Characterization

Several investigators have shown that a characteristic nodular morphology can be seen on carbon/platinum self-shadowed replicas of epoxy network fracture surfaces and solvent etched surfaces. The nodules are thought to be intrinsic structural features as their size was found to vary with reactant stoichiometry. It has been proposed that the nodules are sites of high crosslink density embedded in a matrix of lower crosslink density material. Koutsky and Mijovic² have shown a correlation between nodule size, extent of plastic deformation, and fracture energy; thus there is reason to explore this relationship further.

The technique of self-shadowed surface replication has been advanced to a high degree, as is evidenced by micrographs shown later as Plates 1-7.

Work is in progress examining the rate sensitivity of nodular size obtained from etched fracture surfaces.

It is not clear at this time whether nodules are intrinsic structural features or a result of the technique used to obtain

micrographs of them. For example, Mijovic⁴ prepared samples of aliphatic amine cured epoxies varying in stoichiometry on the epoxy excess side, and subsequently determined their fracture energies and resulting morphologies at one temperature and cross-head speed. Networks formed with different stoichiometric reactant ratios will have different crosslink densities and glass transition temperatures, and therefore different rate sensitivities and abilities to deform under applied loads. Herein lies one as yet unexplored possibility for a nodule size-fracture energy relationship.

We intend to examine the fracture surface morphology of networks differing in their chemical constitution and/or thermal processing history via the replication technique. Measurable structure variations will be correlated with time-dependent mechanical properties.

Time-Dependent Fracture Characterization

Fracture energy is being examined over a wide temperature range using single edge notched rectangular tensile specimens. The fracture behavior is being examined within the framework of Andrews' generalized fracture theory,³ wherein the cohesive fracture energy, T , per unit area of fracture surface is given by

$$T = kcW_{0,c} \quad (1)$$

where k is a parameter dependent on specimen dimensions, strain level, and crack orientation, c is the crack length, and $W_{0,c}$ is the critical input strain energy density. A linear relation is predicted between $W_{0,c}$ and c^{-1} . A plot of this relation for the

1/1 Epon 828/MDA specimen, whose fracture topography is seen in the enclosed micrographs, is shown in Figure 5. The slope of the best fit line yields a value for T of 345 J/m^2 .

The behavior of this material at different test temperatures and the same composition, but of different thermal history, is currently under investigation.

Fracture specimens have been prepared by casting in an open mold using a teflon-coated plate and an o-ring dam of about 6" diameter. Samples are cut from the sheets obtained and edge notches inserted at temperatures above the sample T_g , using the sliding fixture shown in Figure 6.

Mechanical Loss Characterization

Attempts to characterize loss modulus and $\tan \delta$ via the Rheometrics Mechanical Spectrometer using an eccentric rotating cantilever beam (ERCB) experiment have been unsuccessful. We are unable to measure the low forces associated with the loss modulus in this low energy dissipating material. We are looking into the possibility of a torsional mode in conjunction with an instrument available through the Lord Corporation. A master curve of the storage modulus of a 1/1 Epon 828/MDA sample obtained via the ERCB mode is shown in Figure 8.

To facilitate data reduction in this program a computer routine has been written which shifts any viscoelastic function via the WLF transform. Figures 7 and 8 were obtained using this program.

Fatigue Crack Propagation

Compact tension specimens are being stockpiled and testing should be started within the month.

We intend to examine the sensitivity of fatigue behavior toward epoxy network thermal processing variations.

II. MODEL INHOMOGENEOUS GLASSY NETWORKS

A method of dispersing preformed cross-linked particles of known size and spherical shape (gel balls) in a polymer matrix, and of molding the resulting mixture has been found. Particles may be purchased or produced from emulsion polymerized latex using, for example, about 1% divinyl benzene copolymerized with styrene. This discovery makes possible a study of the properties of model systems containing nodular structures (ca. 10-200 nm diameter) like those believed to be present in epoxy resins. For example, the effect of "gel balls" of known size and content on physical properties of rigid polymers can be determined. The morphology of systems known to contain these particles can be examined. Techniques believed to make the dispersed gelled particles visible can be established. These studies should lead to added understanding of the epoxy resins themselves.

The experimental procedures have been evolved through considerable trial-and-error experimentation. Simply mixing the gelled particles with linear polymer was unsuccessful. Molded disks were inhomogeneous and not well-fused. Absorbed monomer containing initiator in the particles was polymerized before molding. This led to molded disks that appeared to be well-fused both to the eye and when examined through a polarizing film. The modified particles could be mixed with pure polymer and the mixture could then be molded to give disks with variable gel particle content. Some pre-polymerization of the monomer is desirable. Molding in the presence of absorbed monomer was an

improvement over simple mixing of the particles with polymer. However, control of variables such as particle concentration, molecular weight of polymer, and distribution of particles in the polymer matrix was comparatively poor. Details of experiments in which the particles were either Styragel or Merrifield resin and the polymer matrix was polystyrene while the monomer was styrene follow.

Materials:

Polystyrene: Dow Chemical's Styron 678 - 26 Clear.

Merrifield Peptide Resin: Pierce No. 24610, 1% crosslinked - chloromethylated styrene-divinylbenzene resin, chloromethylation level - 1-2 meq./g resin, <44-75 microns.

Styragel Type 500 Å: Part No. 27126, Column Packing material, Batch 1632, 37-75 microns.

Styrene: Eastman 1454, Lot No. J6A.

Procedure:

The polystyrene was dissolved in benzene and reprecipitated from methanol. After washing with methanol it was dried and degassed in a vacuum oven at room temperature. The resins were washed with hexane and petroleum ether and dried and degassed along with the polystyrene. After drying the polystyrene and resins were kept under nitrogen until used. The styrene was distilled under nitrogen before use. B.P. - 36°C/8mm. Purified AIBN (azo-bis-isobutyronitrile) obtained from C.-C. Kuo was used as received.

Modifications of the resin surfaces were carried out under nitrogen in screw cap vials with teflon liners. All manipulations were done in a glove bag filled with nitrogen. The mixtures in each vial are listed in Table 1. A vortex stirrer was used to mix thoroughly. When the styrene monomer was polymerized before molding, the vials were heated in an oven at 125°C for 2.5 hours and kept at room temperature for three days before use.

Molding was done in a one-inch compression mold using about three grams of sample. Two Pasadena presses, one at 160°C, and the other with the platens filled with continuously circulating cold water, were used for molding. The materials to be molded were first premolded between teflon coated aluminum foil at a pressure of 5 for 30 sec. (All pressures are on a 5-inch ram.) A typical molding cycle consisted of 10 minute preheat of the mold, adding of appropriate pieces of the premolded material, pressure up to indicated 10 for 10 seconds and release three times to minimize bubble formation, molding at 160°C for two minutes at a pressure indication of 5, rapid transfer to the cold press, and cooling at the same pressure for eight minutes. The modified resins were free flowing powders and could be used without premolding. The results of the molding experiments are summarized in Table 2.

Electronmicrographs (Figure 9) of thin sections of the molded specimens prepared from the samples in which the styrene was polymerized in situ indicated that the gelled particles of both the Styragel and Merrifield Resins are clearly distinguishable

from the polystyrene matrix. The micrographs shown in Figure 9 were taken by transmission electronmicroscopy. Other micrographs of the above resins and of another one, presumably with smaller particle size, were taken by scanning electronmicroscopy. The purposes of these studies were twofold:

1. to verify that the sizes of the resins were as stated by the manufacturers and to get some idea of the particle size distribution; and
2. to determine if the particles swelled significantly during polymerization.

From the photographs taken so far we are able to conclude that indeed the average size of the new resin particles, stated to be $<37\mu$, are smaller than those of the other two resins, which are stated to be in the 37-75 μ -range. The distribution of particle sizes of the Merrifield Resin appears to be lower than that of the Styragels, which are clearly not uniform.

Scanning electronmicrographs of the surfaces of fractured molded specimens are planned for the future. We are awaiting a specimen holder that will allow us to calibrate the scope and make quantitative size comparisons possible. Alternately, or in addition, a Zeiss Particle Analyzer available in our Institute will be used to study particle size and particle size distribution.

Other smaller sizes of gelled particles are being purchased and still others will be synthesized.

TABLE 1

Modification of Resins

Vial No.	Modification of Resins			Comments	
	Styragel g	Herrifield Resin g	Styrene ml ^a g		AIBN g
1	2.5	-	1 1.10	-	Styrene was quickly absorbed into the resin and the basic appearance of the resulting material did not change significantly.
2	-	2.5	1 1.10	-	The resin swelled to about three times the original volume and was somewhat lumpy.
3	2.5	-	1 1.10	0.005	Same as No. 1.
4	-	2.5	1 1.10	0.005	Same as No. 2.
5	2.5	-	2.5 2.8	0.0125	See No. 1. Kept in oven at 125°C for 2.5 hours. ^d Product was slightly yellow free flowing powder.
6	-	2.5	2.5 2.8	0.0125	Kept in oven for 2.5 hours. Product was lumpy slightly ^d yellow powder. (See No. 2)
7	-	-	2.5 2.8	0.0125	Kept in oven for 2.5 hours. 15 min - cloudy and viscous ^b 45 min - very thick but pourable; 2.5 hrs. - hard and not pourable at all.
8	-	-	2.5 2.8	-	Kept in oven for 2.5 hours. 15 min - fluid and clear 45 min - slightly viscous; 2.5 hrs - set up but still a bit soft ^c .

^aWhen AIBN was used, the volume quoted is that of a stock solution prepared from 0.6g AIBN and 12 ml styrene (i.e. 0.5% AIBN).

^bThe polymerization was judged to be well advanced by 2.5 hours and removed from the oven. It probably continued somewhat on standing. The experiment shows that the styrene was polymerizable.

^cThe rate of thermal polymerization was clearly slower than that of the free radical initiated polymerization containing AIBN.

^dThe weight of product available subsequently for molding purposes, the odor of the product, the texture of the product (harder than 1-4) all indicated that the styrene monomer had polymerized during this treatment.

TABLE 2

Molding Experiments

Disk NO	Reprecipitated Polystyrene g	Styragel g	Merrifield Resin	Vial Product Vial NO	Wt	Comments ^a
1	3	-	-	-	-	Sample was well fused and reasonably strain free.
2	1.5	1.5 ^b	-	-	-	Polystyrene was fused but the disk clearly had much dispersed unfused white powder.
3	1.5	1.5 ^c	-	-	-	Fusion was very bad. Even the polystyrene didn't fuse well.
4	1.5	+ ^d	-	1	1.5	Disk had some distinct unfused areas. Much monomer must have been lost during molding because the weight of disk was very low.
5	1.5	+ ^d	-	3	1.5	Contains AIBN More uniform disk than from No. 4 (thermal polymerization only). Less weight loss but still see white powder.
6	1.5	+ ^d	-	5	1.5	Resin contains prepolymerized polystyrene. Sample is well-fused. White areas are essentially gone. Shows that modified resin can be diluted.
7	-	+ ^d	-	5	3.0	Disk appears homogeneous and well-fused. Modified resin molds well.
8	1.5	-	+ ^d	6	1.5	Same comments as No. 6. However, with polarized light two phases can be seen. The Merrifield Resin seems less compatible with polystyrene than styragel.
9	-	-	+ ^d	6	3.0	Well fused sample. Same comments as No. 7.

(continued to next page)

Footnotes to Table 2

^a Products were examined by eye and behind a polarizing film. Nonuniformities and strain as well as poor fusion are more readily seen when a polarizing film is used.

^b The unpurified resin.

^c The purified resin.

^d † indicates that the purified resin of this type was in the vial.

III. RUBBERY NETWORKS

The objectives of this task are two-fold: to prepare a viscoelastic network polymer applicable to a variety of engineering studies, and to correlate time-dependent fracture energy with molecular structure. The networks are prepared with varying average molecular weight between cross-links (M_c), and have two different backbone structures. While the early phases of this task are examining molecular effects on fracture energy in rubbery networks, the fracture behavior of glassy network polymers such as epoxy resins are also being studied above their T_g , if such networks can be characterized quantitatively by methods indicated in section I above.

Two prepolymers from ARCO have been selected for early study. ARCO's R-45HT is a dihydroxy-terminated liquid polybutadiene of reported average molecular weight 3000. It is colorless, noncrystallizing and commercially available in large quantities. ARCO's CS-15 is a dihydroxy-terminated liquid styrene-butadiene copolymer of reported average molecular weight 3400. It is noncrystallizing, but a little hazy and available in limited quantities.

Both tetrafunctional and trifunctional curing agents were tried in preparing the networks; however, only the trifunctional isocyanate linked structures succeeded. Tetrafunctional curing agents such as 1,2,4,5-benzenetetracarboxylic anhydride and

1,4,5,8-naphthalenetetracarboxylic anhydride are both high melting materials and not soluble in the prepolymer. These drawbacks make the efficient mixing of these materials practically impossible.

The trifunctional curing system, toluene diisocyanate and 2,-ethyl-2-(hydroxymethyl)-1,3-propanediol, consists of low melting reactants. The curing reaction of the mixture is slow enough to allow time for good mixing. Chain extended networks of this type have also been prepared using 1,4-butane diol.

Several samples of these trifunctional networks have been characterized. The measurements of their fracture energies have been started, and some of the preliminary results will be given later in this report.

Characterization

Ten samples prepared by casting on a teflon plate have been characterized to be used in fracture studies. Table 3 shows the M_C , T_g and sol fraction characteristics of the replicate castings. The Mooney-Rivlin parameter, C_2 , is indicated as well. Series TB_{1X} was prepared from R45-HT; series TB_{2X} and TB_{3X} are chain-extended R45-HT. A second set of samples of similar stoichiometries was prepared and characterized using a different batch of ARCO R45-HT. These are shown in Table 4. Sample TS_1 is an isocyanate cross-linked CS-15; another sample designated as PB_1 is a high molecular weight polybutadiene cured with dicumylperoxide, to be used for comparison purposes.

The number average molecular weight between cross-links, M_C , was computed from the C_1 intercept values taken from

Props. Sample	a Mc	C ₂	b T _g °C	% Sol Fraction
TB ₁₁	3,340	2.72	-79.0	0.8
TB ₁₂	3,400	2.45	-79.6	
TB ₁₃	3,400	2.82	-78.5	
TB ₁₄	3,300	2.65		
TB ₂₁	5,200	2.55	-79.0	1.5
TB ₂₂	5,170	2.70	-79.0	
TB ₂₃	5,800	2.80		
TB ₃₁	8,300	2.0	-79.5	3.0
TB ₃₂	8,750	1.52	-79.0	
TB ₃₃	9,700	1.30		

Table 3

Characterization of Networks
for Fracture Studies

a : from Mooney-Rivlin equilibrium tensile plot

b : measured by DuPont DSC (Model 990) at 5°C/min.

Sample Props.	TB ₁	TB ₂	TS ₁	PB ₁
C ₁ x10 ⁻⁵ N/m ²	4.25	2.2	3.1	1.30
C ₂ x10 ⁻⁵ N/m ²	1.30	3.0	1.45	1.20
M _C ^a	2,750	5,250	3,700	8,300
M _C ^b	3,100	6,200	3,700	--
T _g °C ^c	-80	-80	-65	-93
ρ ^d	0.954	0.945	0.955	0.885
E ₀	32.9	32.9	26.1	14.30
ρ(C ₁ + C ₂)	33.4	33.6	27.0	15.0

Table 4

Characterization of Samples TB₁, TB₂, TS₁ and PB₁.

a : From Mooney-Rivlin plot

b : Calculated data from reported prepolymer \bar{M}_n .

c : Measured by DuPont DSC Model 990 at the speed of 10°C/min.

d : Determined by pycnometer, ASTM D297.

equilibrium stress-strain Mooney-Rivlin plots, as shown in Figure 11. Somewhat surprisingly, the M_c values calculated from this plot match very well with those of their prepolymers determined from the chemical composition (Table 4). Although the average hydroxyl functionality of the prepolymer is given as slightly greater than 2, it is well-known that the functionality distribution is rather large. The Mooney-Rivlin plots of TB₂ swelled in hexane still had a noticeable C_2 value (Figure 12) and the C_1 values are larger than those determined in unswollen samples by approximately 20%.

The true stress vs. strain plots for the more tightly linked samples show linear behavior to relatively high strains ($\lambda \sim 1.8$), as shown in Figure 13. The initial modulus of rubber-like materials should be between $6 C_1$ and $6(C_1+C_2)$.⁵ The values obtained from these samples indicate that E_0 is almost equal to $6(C_1+C_2)$ (Table 4).

Sample TB₁ is currently the best candidate for a standard viscoelastic network polymer. It can be made quite transparent by casting on Ferro type plates instead of teflon-coated plates used frequently in these studies. It is linearly viscoelastic below extensions of about 15% (Figure 14), The loss modulus appears to be independent of the prestrain up to strains of 0.4 (Figure 15) while $\tan \delta$ increases somewhat linearly with strain (Figure 16). Some preliminary fracture studies of the series TB₁₁-TB₁₄ also indicate that it is rate dependent up to 70°C.

Data accumulated thus far indicate that the trifunctional end-linked networks behavior similarly with randomly cured rubbers. However, future studies over a wider range of material variables and test conditions will be required before this conclusion may be generalized.

Fracture Studies

Samples of R45-HT have been prepared in a vertical mold, providing uniform thickness, with and without chain extender. Samples TB₁₁, TB₂₃, and TB₃₃ have been characterized to have M_c values of 3,340, 5,800 and 9,700, respectively.

Figure 17 shows the tear energy of TB₁₁ at different temperatures and crosshead rates. The WLF procedure is used to shift the data to produce a master curve using the following constants:

$$\log a_T = \frac{-31.1(T-T_g)}{78.0 + T-T_g}$$

A preliminary master curve of the tear energies of TB₁₁, TB₂₃ and TB₃₃ is shown in Figure 18. It may be seen that at the higher speeds or lower temperatures, the tear energy curves of TB₁₁, TB₂₃ and TB₃₃ separate quite a lot, while at low speed and high temperature they converge.

Discussion

The major efforts in this task during the first year have been to develop convenient methods for uniform sample preparation, refine the characterization methods for end-linked elastomers and to begin tear studies on the networks produced. A limited amount of viscoelastic data has been obtained in dynamic and stress relaxation testing. Future plans are to supply samples of each of the end-linked networks to Dr. Plazek of The University of Pittsburgh for his specific studies of the material response. Various viscoelastic quantities will be examined, in particular the mechanical loss (G'' and $\tan \delta$) correlation with the time-dependent fracture behavior of these materials. Several samples from earlier networks prepared in the course of the investigation have been tested in the torsional creep mode by Dr. Plazek. The following section on thermal expansion studies raises important questions about transitions which may be related to the relatively high concentration of urethane links in the various networks. Subsequent investigations to provide information on the relationship of structure to volume relaxation or phase-transitions are underway.

IV. Thermal Expansion Measurements

Dilatometric studies were started on the polyurethane network polymers prepared from R-45HT and CS-15. DSC measurements indicate that the glass transition temperature of these polymers ($\sim -90^{\circ}\text{C}$) is well below the freezing point of mercury (-39°C) and of most other suitable confining liquids. Therefore, a slightly modified thermal expansion apparatus previously described by M. L. Dannis^{6,7} was used for our initial studies. Since no confining liquid is required, this apparatus can be used in any desired temperature range provided a suitable cooling or heating chamber is available.

Apparatus

As shown in Figure 19, the apparatus is a simplified form of dilatometer in which the actual expansion or contraction of the sample is measured mechanically in one chosen direction or dimension. A mirror tripod rests one leg on the sample and the other two on a metal cup holding the sample. A circular aluminum plate beneath the leg on the sample prevents indentation of the sample. Movement of the sample relative to the cup tips the tripod and mirror and thus moves a spot obtained by reflecting a beam of light from the mirror onto a scale. The cells were loaned to us by M. L. Dannis, whose advice in assembling the apparatus is gratefully acknowledged.

Temperature of the sample is measured by an iron-constantan thermocouple inserted close to the midpoint of the sample and

connected to a potentiometer. The thermocouple is made of No. 40 gauge wire to eliminate false movements of the sample arising from the springiness of heavier gauge wires. An ice junction is used. Values of temperature are read from standard tables relating the observed millivolts to temperature.

For measurements below room temperature, the assembled cup containing sample and tripod is flooded with liquid nitrogen in a vacuum flask. After the excess nitrogen has boiled away, expansion of the sample on warming to room temperature is followed as a function of temperature. The rate of warming near -100°C is about $0.3^{\circ}\text{C}/\text{min}$; near 0°C it is less than $0.1^{\circ}\text{C}/\text{min}$.

For measurements above room temperature the vacuum chamber is replaced by a tubular heater, whose temperature is increased by gradually increasing the applied voltage with the aid of a Variac. The heating rate is about $0.25^{\circ}\text{C}/\text{min}$.

Results

Figure 20 shows a typical differential thermal expansion curve for a polybutadiene containing 95% 1,4-cis units. This figure is taken from data reported by M. L. Dannis⁷ and is included as an aid to interpretation of the data presented below.

Figure 21 shows some results obtained on our apparatus using samples of two well-known polymers. Firestone's Diene 35NFA is a noncrystallizing polybutadiene containing 55% 1,4-cis, 35% 1,4-trans and 10% vinyl units and was cured using 0.1%

dicumyl peroxide, Hercules Dicumyl. The data obtained with this sample shows only the expected T_g at approximately -96.5°C . The Pale Crepe sample was used as a gum rubber (uncured) and the plot obtained using it shows the glass transition temperature, some crystallization and the onset of melting.

Figure 22 shows typical results obtained using sample TB₂₄, a chain-extended polyurethane from R-45HT and 1,4-butanediol having $M_c \approx 6000$. Similar data have been obtained on three different samples of the same material and on repeated runs on the same sample. The curve shows some unexpected features. At about -90°C , the glass transition temperature expected from DSC, a contraction occurs. By analogy to the results given in Figure 20, this contraction may be associated with crystallization. The rest of the curve is consistent with such an interpretation. However, crystallization of this sample was not expected and other possible interpretations such as phase segregation or mechanical relaxation are being considered. Similar measurements with the other samples in the series are in progress. The results on the polymer prepared from the copolymer containing styrene should be especially significant but are not yet completed. This sample should not crystallize.

Discussion

It is important for our studies to establish that the transition observed at $\sim -90^{\circ}\text{C}$ is real and if it is, to determine the reason for the transition. Phenomena such as crystallization or crystallizability have very significant effects on

time-dependent fracture of elastomers. Therefore, several experiments along these lines are planned.

The polyurethanes being used in this study are of variable stiffness. The possibility of mechanical relaxation cannot be ignored. The dilatometric measurement will be repeated in a standard dilatometer using an appropriate silicone fluid as the confining liquid. If the same transition is observed, mechanical relaxation will be eliminated as a possibility.

The presence or absence of a crystalline phase will be determined. The polybutadiene microstructure of the R45-HT consists of 60% 1,4-trans, 20% 1,4-cis and 20% vinyl units. It is possible that the 1,4-trans units could crystallize at the low temperatures used in our experiments. The melting temperatures reported⁸ for 1,4-trans (99-100%) polybutadiene are 97 and 145°C for Modifications I and II, respectively. The inflection shown in Figure 22 at about 110°C is in the right temperature range for crystallized 1,4-trans units. X-ray studies are planned to determine if the sample is at all crystalline. If it is, the unit cell dimensions will be compared with those reported for 1,4-trans polybutadiene.

Other studies will be carried out as required.

References

1. Mooney, M., J. Appl. Phys., 11, 582 (1940); 19, 434 (1948); Rivlin, R. S., Trans. Roy. Soc. (London), A240, 459, 491, 509 (1948); 241, 379 (1948).
2. Mijovic, Jovan and Koutsky, J. A., Polymer, 20, 1095-1107 (Sept. 1979).
3. Andrews, E. H., J. Materials Sci. 9 (1974), 887.
4. Mijovic, Jovan, "A Correlation Between Morphology and Fracture Properties of Epoxy Resins", Ph.D. Thesis, Univ. of Wisconsin, 1978.
5. Wood, L. A., Journal of Research, Nat. Bur. Standards, 84, No. 5, 353 (1979).
6. Dannis, M.L., J. Appl. Polym. Sci., 1, 121 (1959).
7. Dannis, M.L., J. Appl. Polym. Sci., 4, 249 (1960).
8. Polymer Handbook, 2nd Edition, J. Brandrup and E. H. Immergut, Eds., John Wiley & Sons, New York, N. Y. (1975), p. V-3.

- FIGURE 1. Vacuum Mixing and Casting Apparatus for Epoxy Samples
- FIGURE 2. Four-Cavity Mold for Epoxy Compact Tension Specimen Casting
- FIGURE 3. Mooney-Rivlin Plot of 20% DMSO Pre-swollen Epoxy Sample
- FIGURE 4. Dilatometric Determination of Glass Transition Temperature of Pre-swollen DMF-Epoxy Sample
- FIGURE 5. Critical Strain Energy Density versus Reciprocal Crack Length
- FIGURE 6. Crack Insertion Tool for Fracture Specimens
- FIGURE 7. Representative Computer Plot of Dynamic Storage Modulus of Epoxy Material
- FIGURE 8. Computer Generated Storage Modulus Master Curve for Epoxy Material
- FIGURE 9. Electron Micrographs of Styragel and Merrifield Resin in Polystyrene Matrix
- Figure 10. Electron Micrographs of Commercial Gelled Resin Particles
- FIGURE 11. Mooney-Rivlin Plot of Samples TB₁, TB₂, TS₁ and PB₁
- FIGURE 12. Mooney-Rivlin Plot of Sample TB₂, TS₁ and PB₁ in Hexane.

- FIGURE 13. True Stress vs. Strain of Samples
- FIGURE 14. Stress-Relaxation Data for Sample TB₁
- FIGURE 15. Loss Modulus vs. Statis Deformation ϵ for Sample TB₁
- FIGURE 16. Tan δ vs. Statis Deformation ϵ for Sample B₁
- FIGURE 17. Temperature and Rate Effects on Tearing Energy T for Sample TB₁₁
- FIGURE 18. Master Curves of Tear Energy vs Effective Strain Rate for Samples TB₁₁, TB₂₃ and TB₃₃
- FIGURE 19. Schematic Illustrations of Thermal Expansion Apparatus
- FIGURE 20. Typical Differential Thermal Expansion Curve for His cis Polybutadiene Rubber⁷
- FIGURE 21. Thermal Expansion Curves for Diene 35NFA and Pale Crepe Obtained on the Apparatus Described in Figure 19
- FIGURE 22. Typical Thermal Expansion Curve Obtained using Sample TB₂₄ and the Apparatus Described in Figure 19.

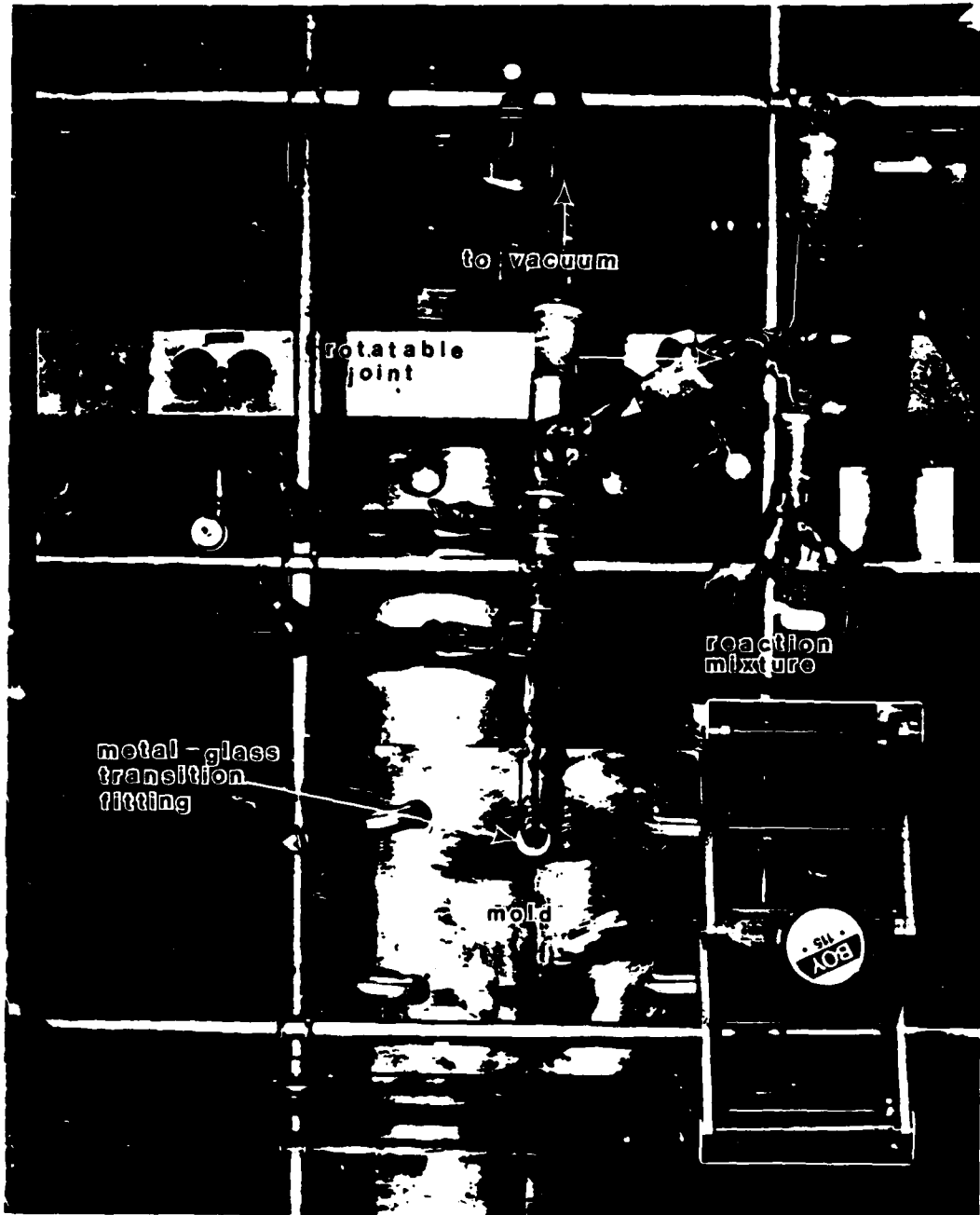
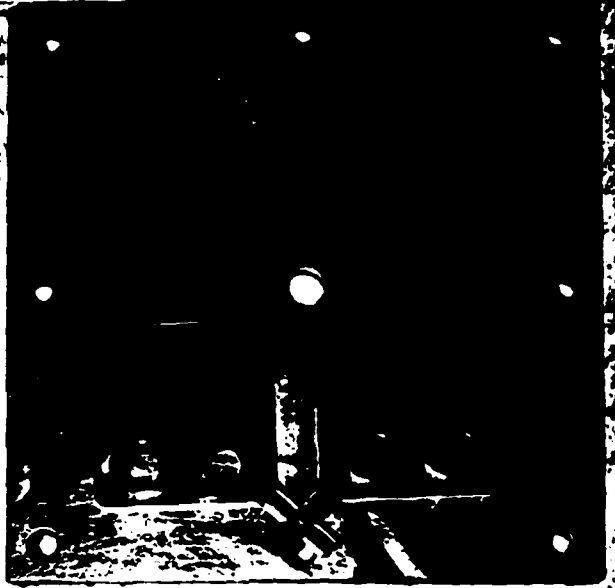
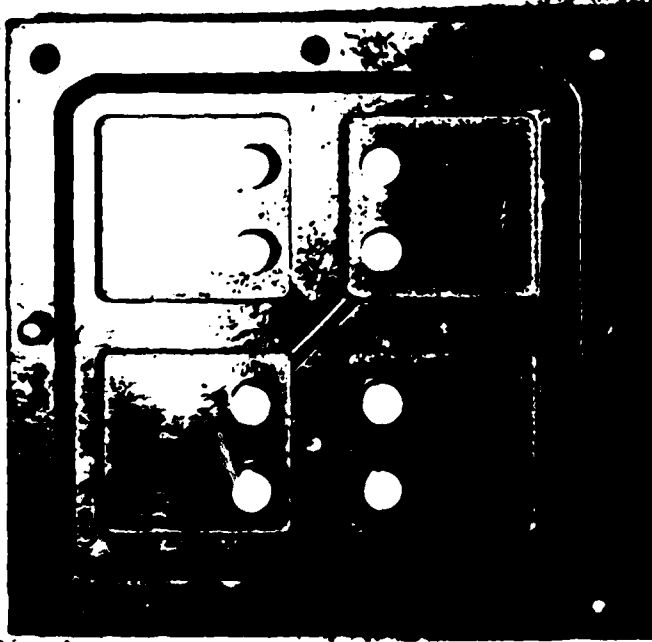


Figure 1. Vacuum Mixing and Casting Apparatus for Epoxy Samples.

compact tension sample
mold



Scholarships... Flying Lessons...
\$100 a Month Allowance.
PUT IT ALL TOGETHER
IN AIR FORCE ROTC

Figure 2. Four cavity Mold for Epoxy Compact Tension Specimen Casting.

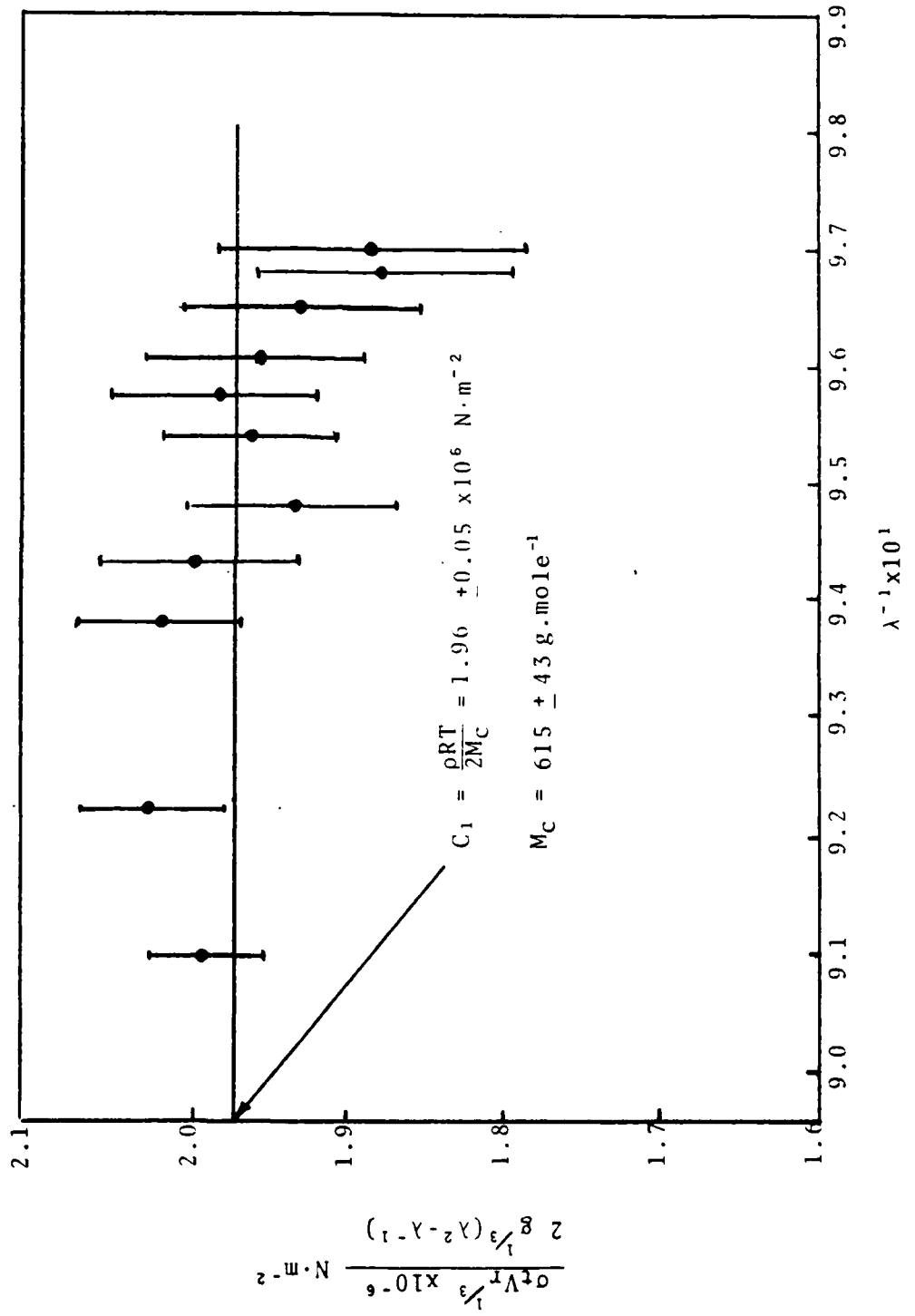


Figure 3. Mooney-Rivlin Plot of 20% DMSO Pre-swollen Epoxy Sample.

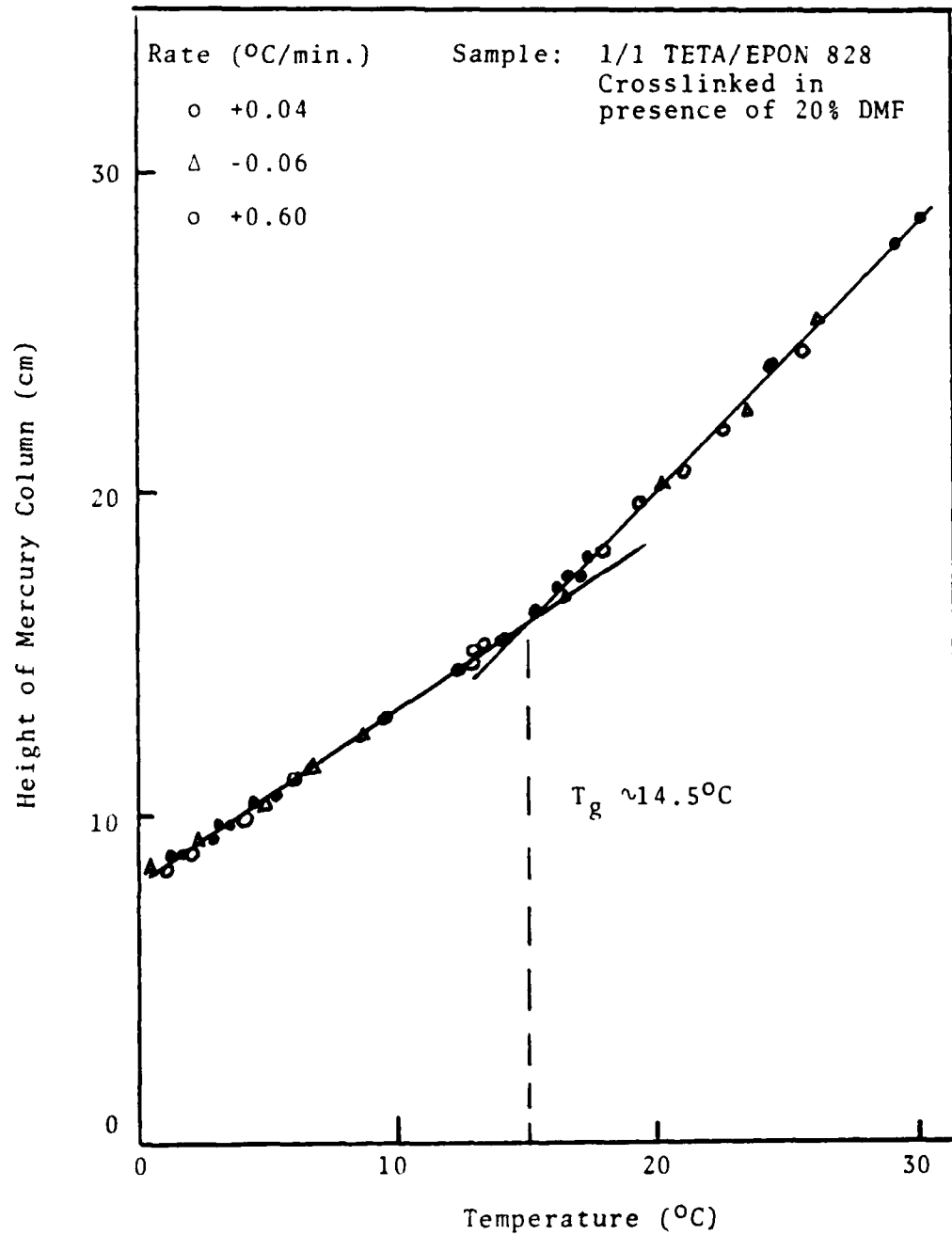
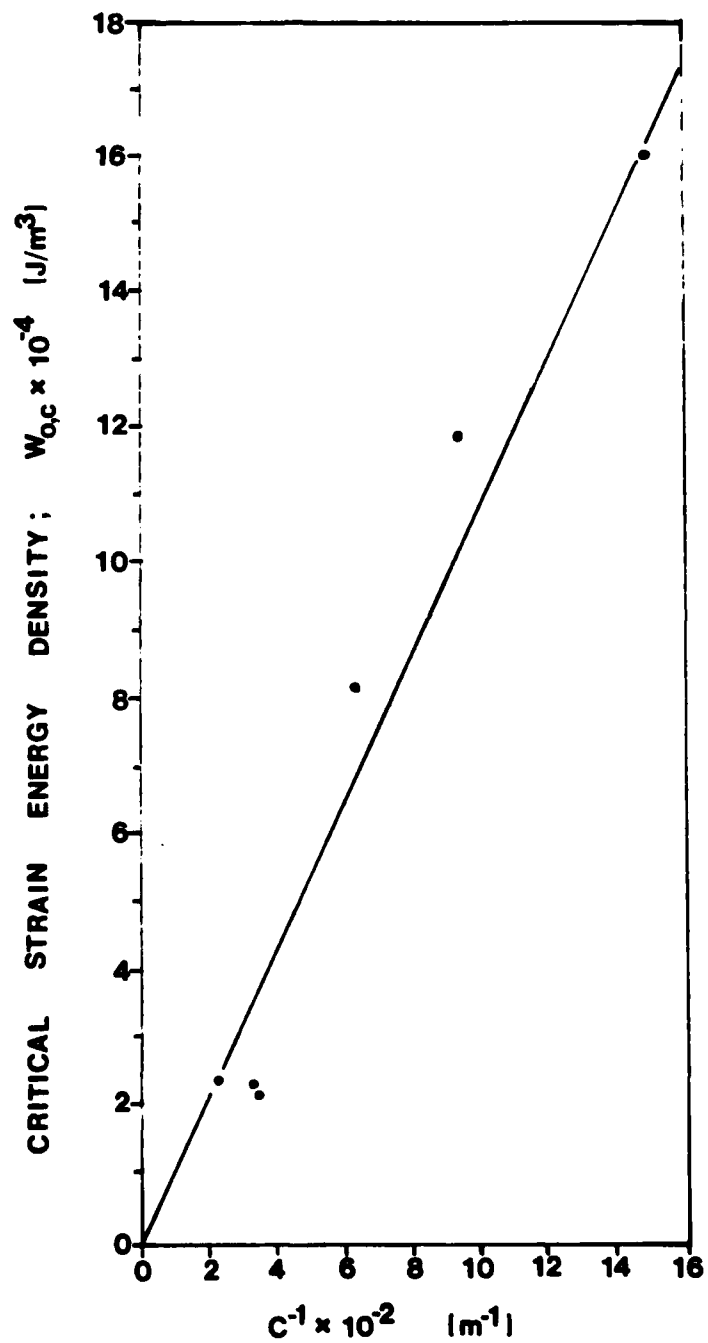


Figure 4. Dilatometric Determination of Glass Transition Temperature of Preswollen DMF-Epoxy Sample.

FIGURE 5



Critical Strain Energy Density versus Reciprocal Crack Length. Results for 1:1 MDA: Epon 828 Fractured at 25°C; crosshead speed = 0.2 in/min.

crack insertion tool

fracture
test piece

blade

slide

guide

Scholarships... Flying Lessons...
\$100 a Month Allowances.
PUT IT ALL TOGETHER
IN AIR FORCE ROTC.

Figure 6. Crack Insertion Tool for Fracture Specimens.

DYNAMIC STORAGE MODULUS

EPON 929/MIH 1/1

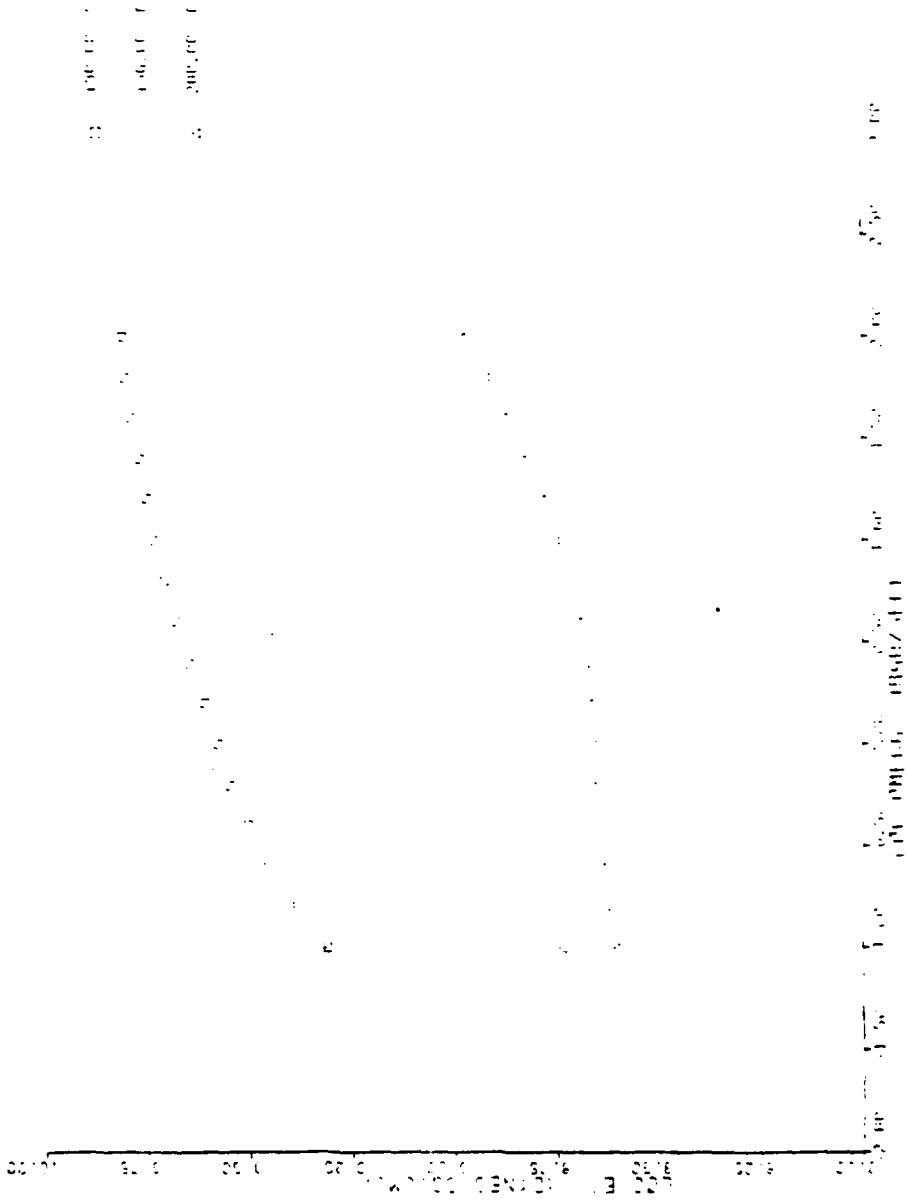


Figure 7. Representative Computer Plot of Dynamic Storage Modulus of Epoxy Material.

STORAGE MODULUS MASTER CURVE

EPOXY 845/MOH 1/1

REFERENCE TEMPERATURE : 130.00 C

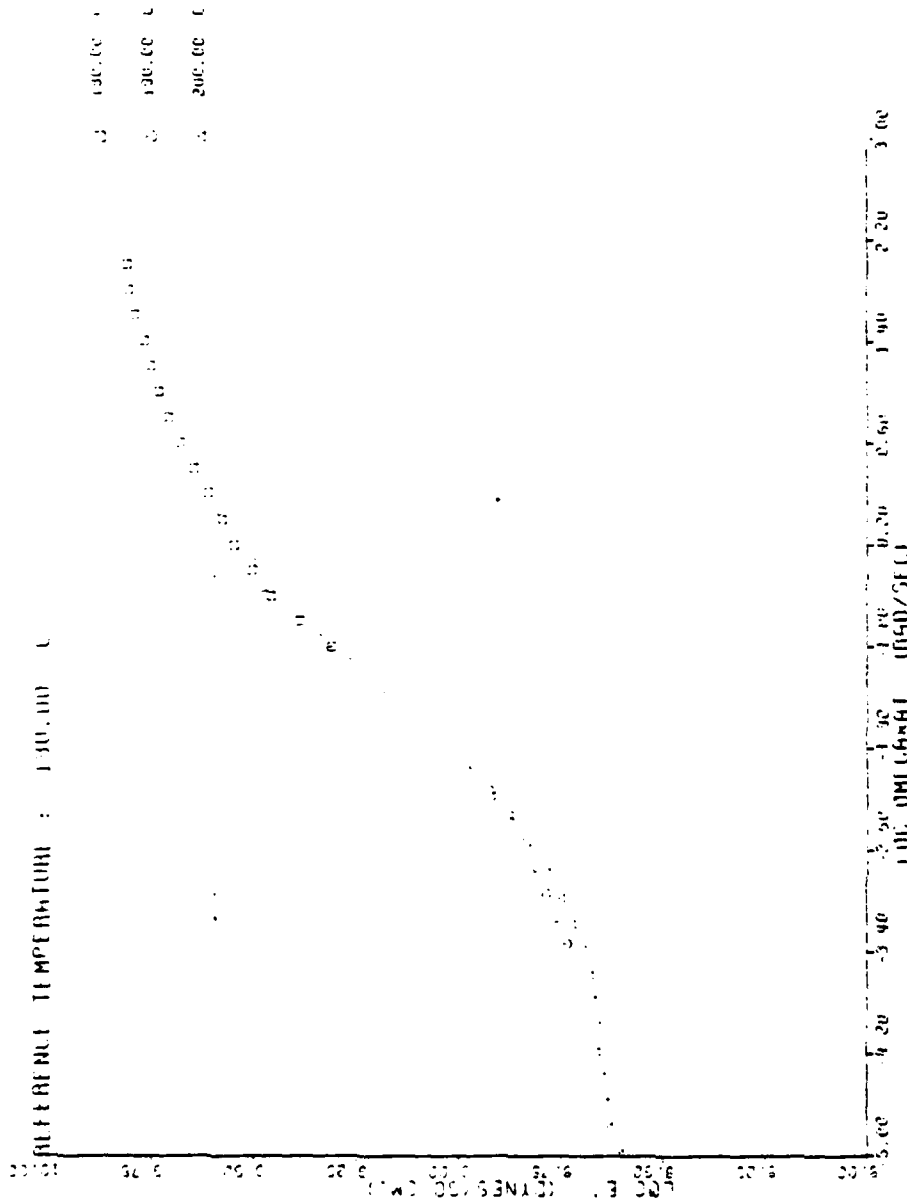


Figure 8. Computer Generated Storage Modulus Master Curve for Epoxy Material.

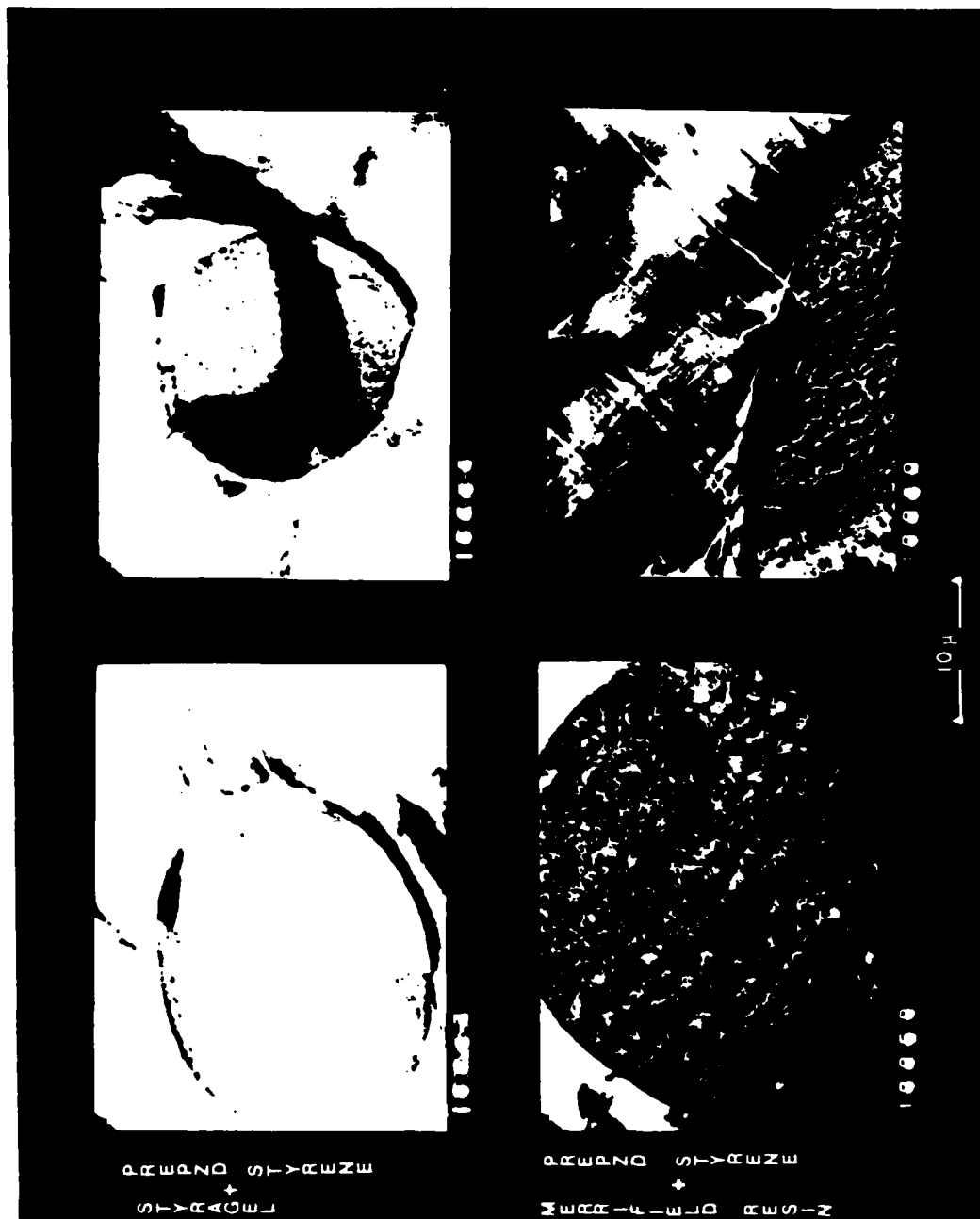


Figure 9. Electron Micrographs of Styragel and Merrifield Resin in Polystyrene Matrix.

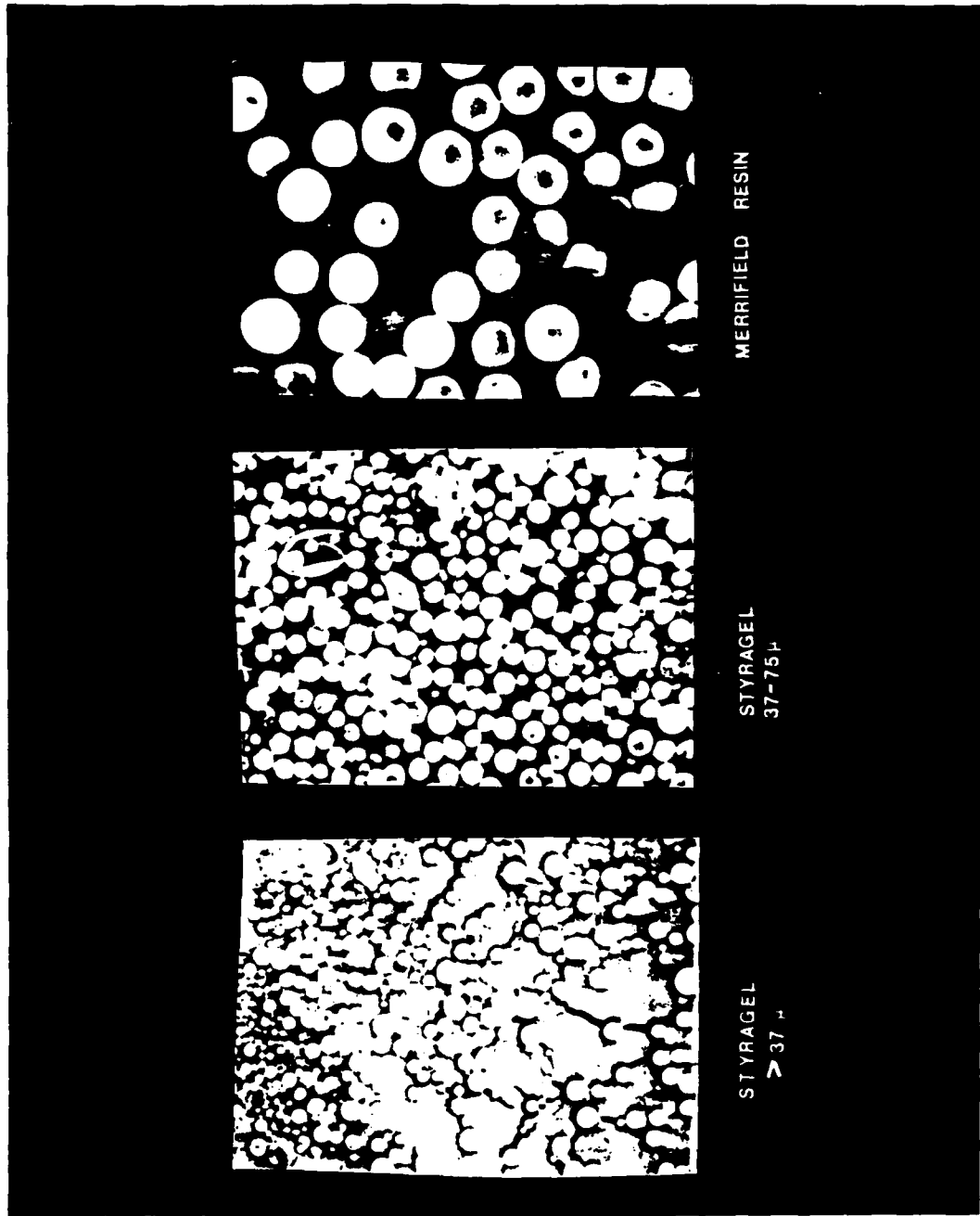


Figure 10. Electron Micrographs of Commercial Gelled Resin Particles.

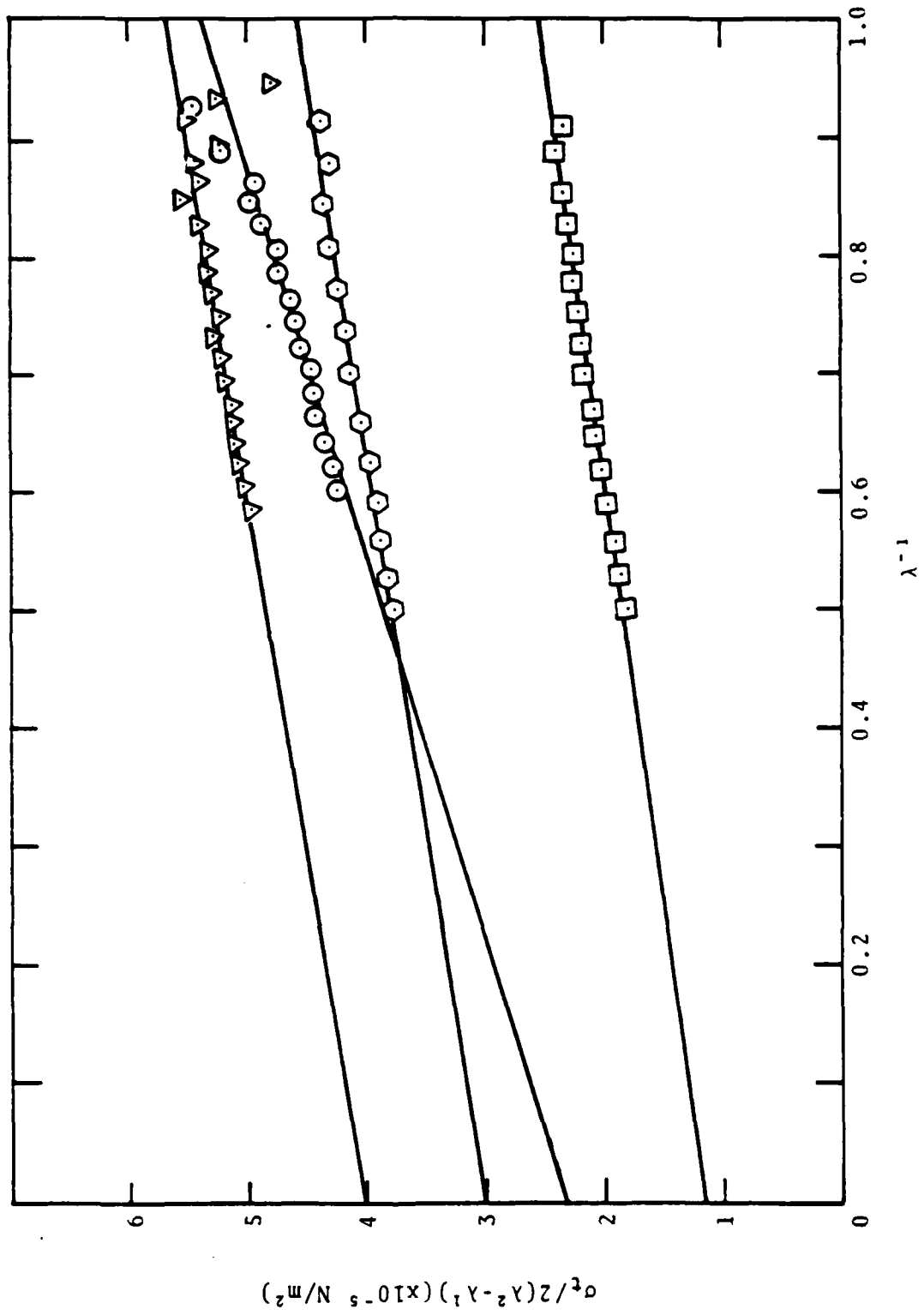
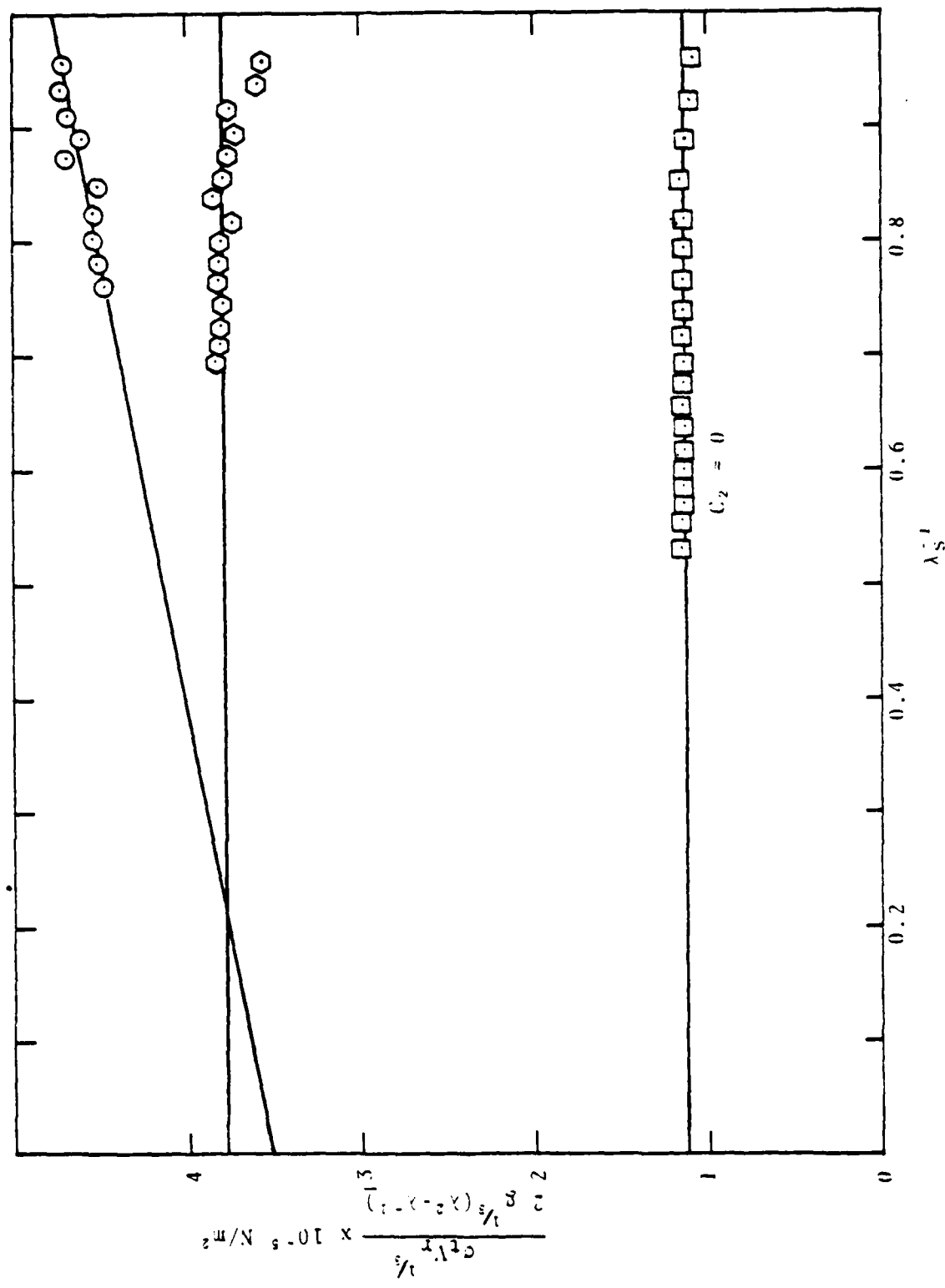


Figure 11. Mooney-Rivlin plot of samples: ∇ : TB₁, \circ : TB₂, \circ : TS₁ and \square ; PB₁

Figure 12. Mooney-Rivlin plot of sample TB₂, TS₁ and PB₁ in hexane.
 O : TB₂, ◯ : TS₁, ◻ : PB₁
 λ_s = extension ratio based on swollen length; v_r = volume swelling ratio; g = gel fraction.



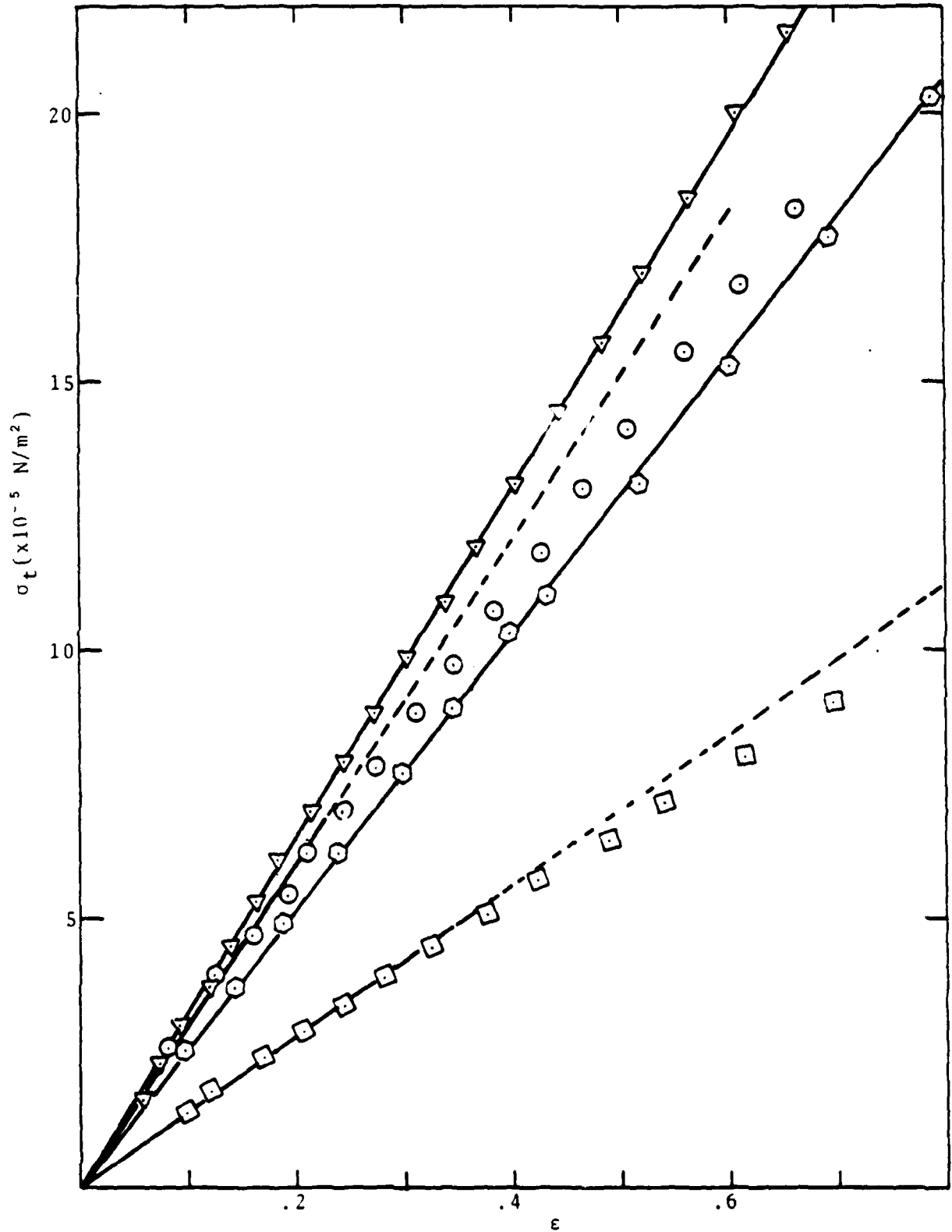


Figure 13. True stress vs. strain of samples

∇ : TB₁, O : TB₂, \hexagon : TS₁ and \square : PB₁

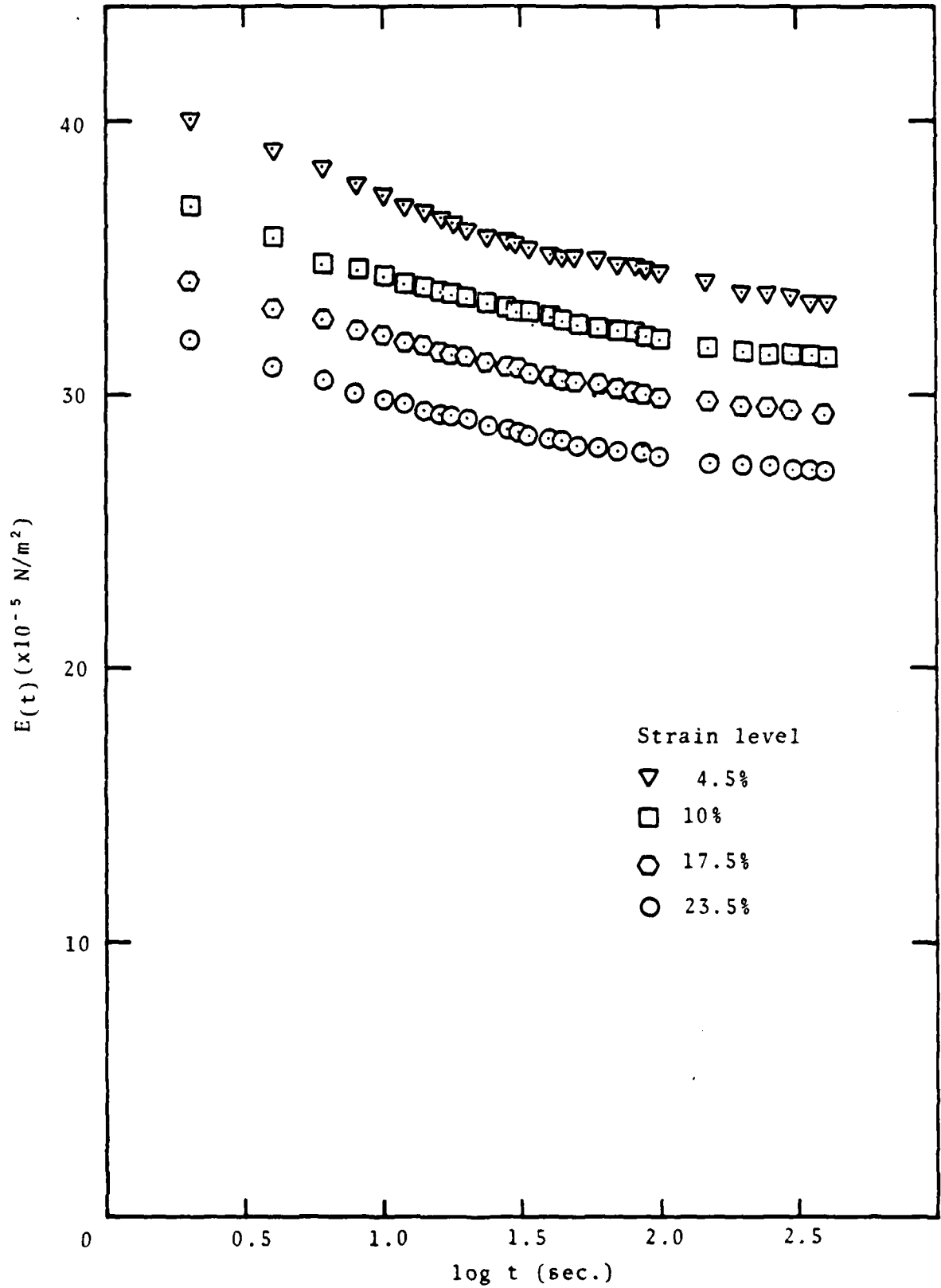


Figure 14. Stress-relaxation data for Sample TB₁.

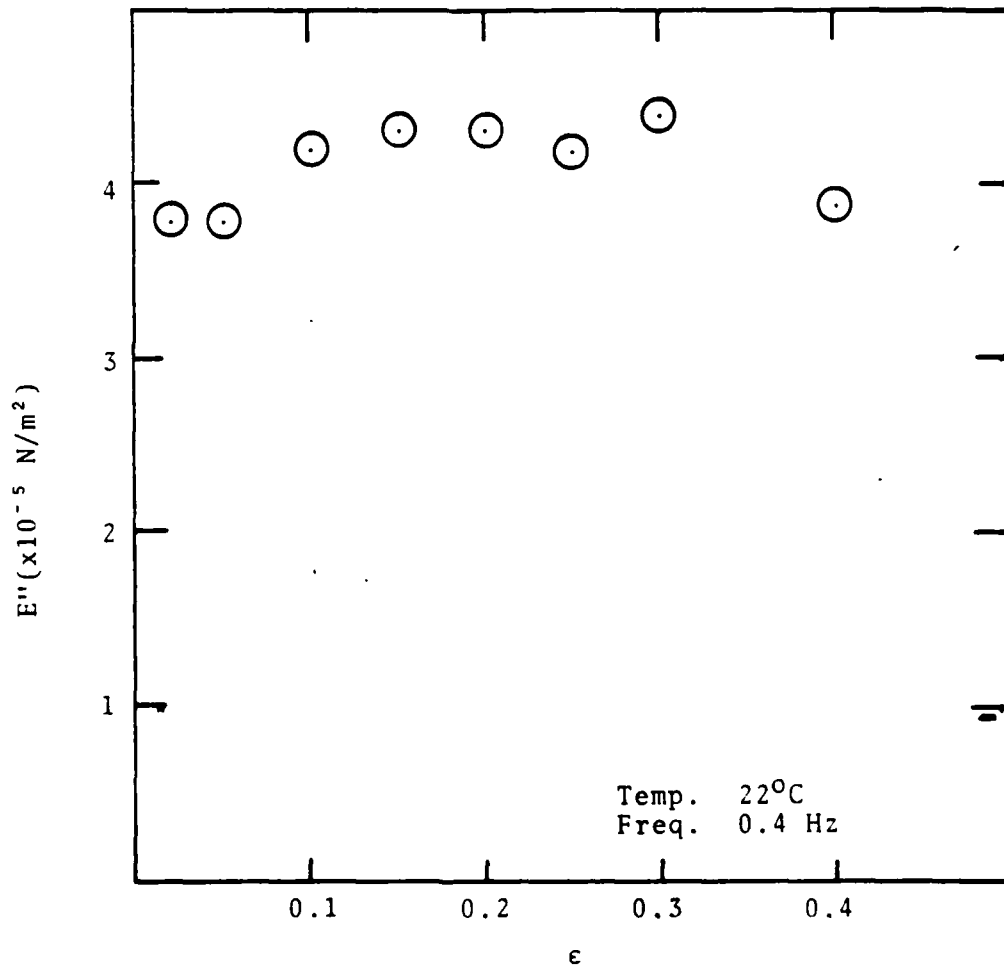


Figure 15. Loss modulus vs. static deformation ϵ for sample TB₁.

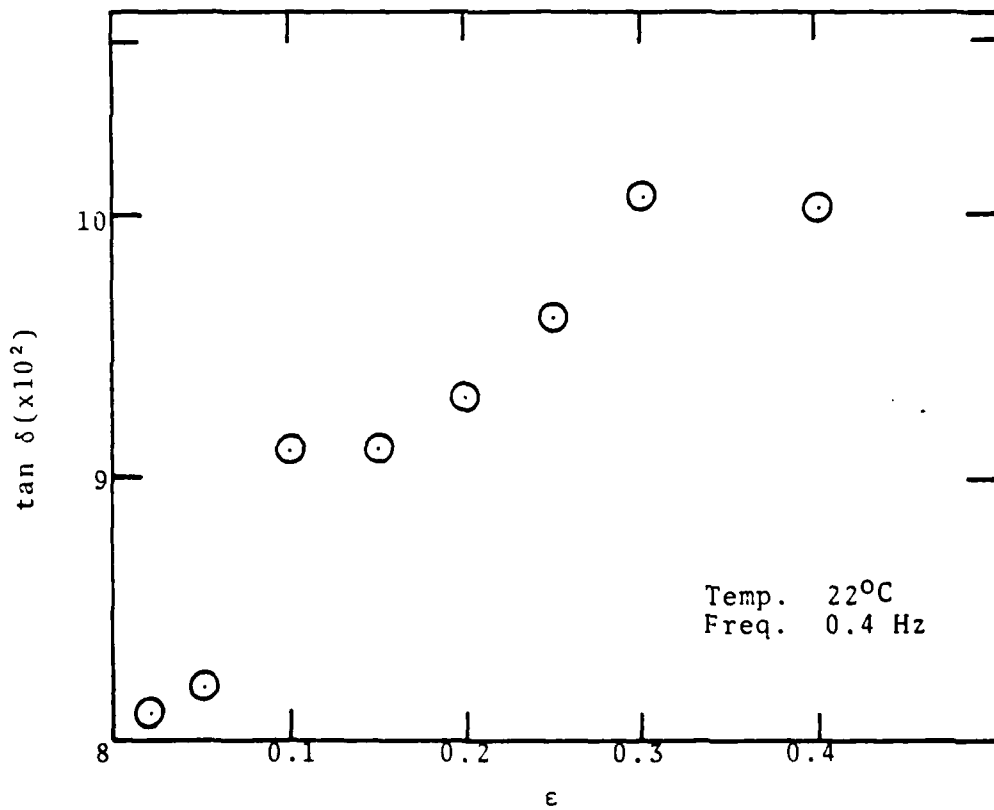


Figure 16. $\tan \delta$ vs. static deformation ϵ for sample B₁.

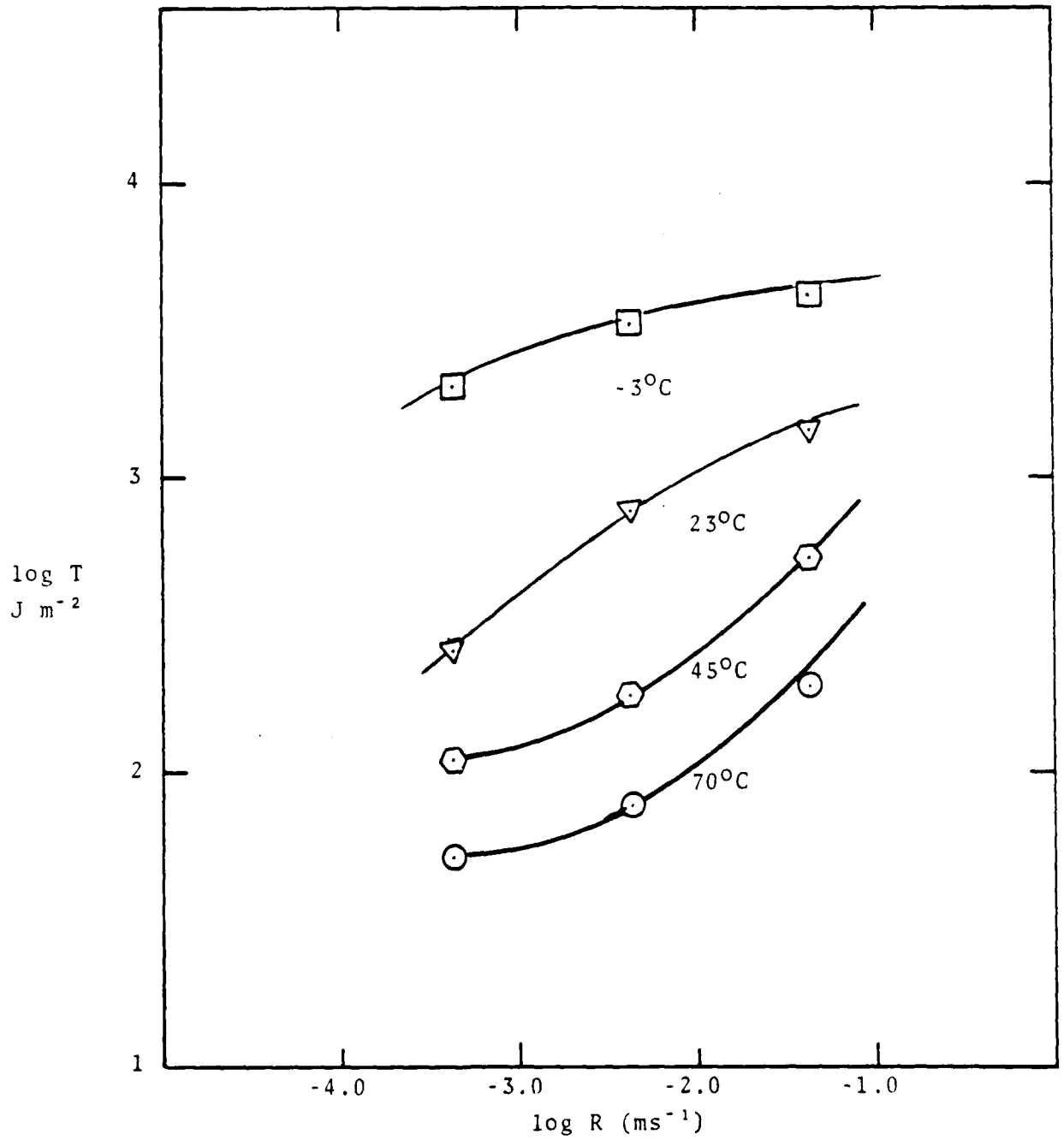


Figure 17. Temperature and rate effects on tearing energy T for sample TB_{11} .

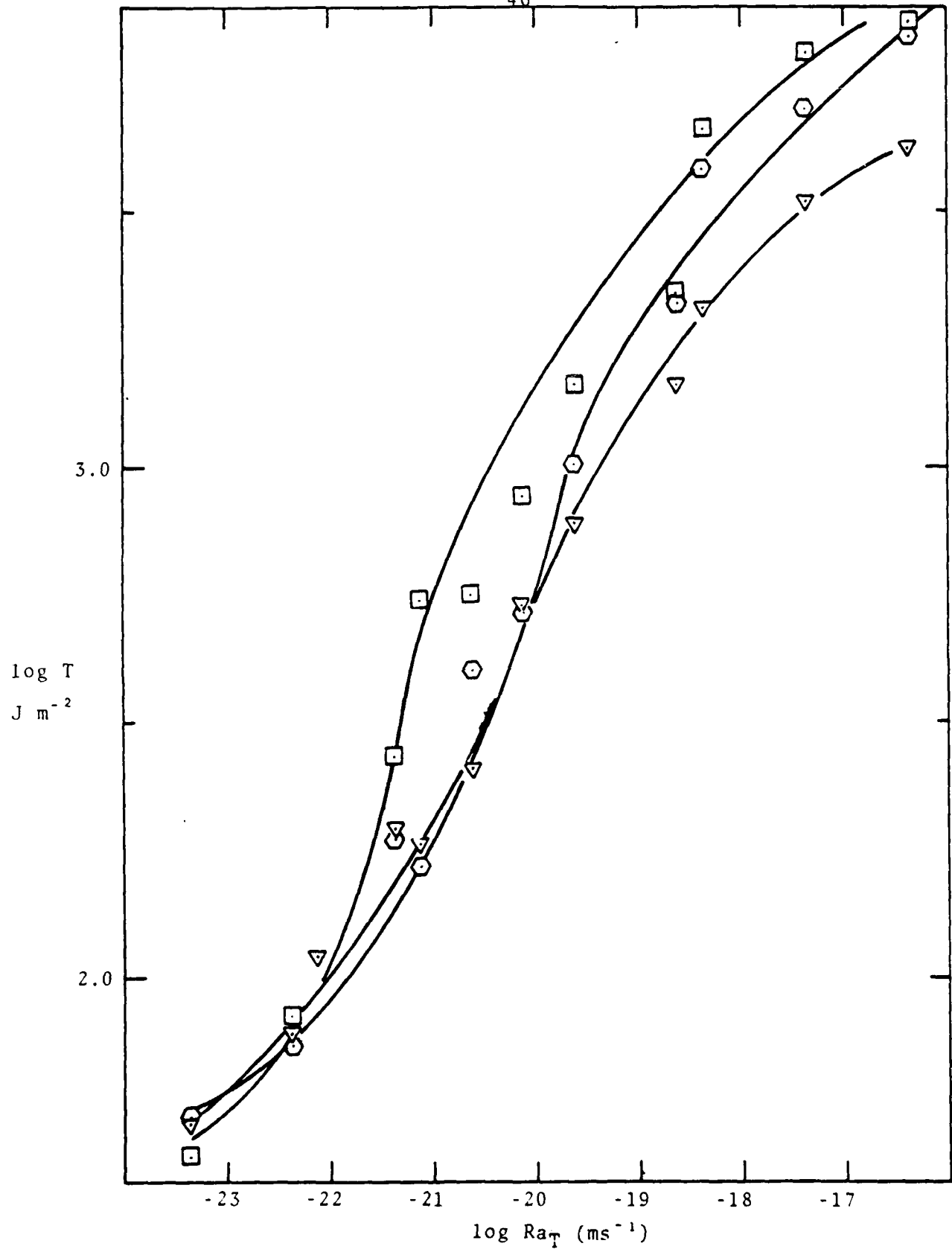
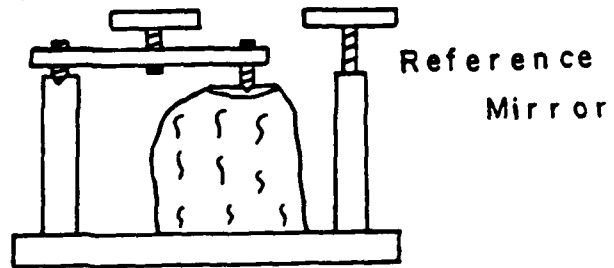


Figure 18. Master curves of tear energy vs. effective strain rate for samples ∇ TB₁₁, \circ : TB₂₃ and \square : TB₃₃.

A.

Tripod and Mirror



B.

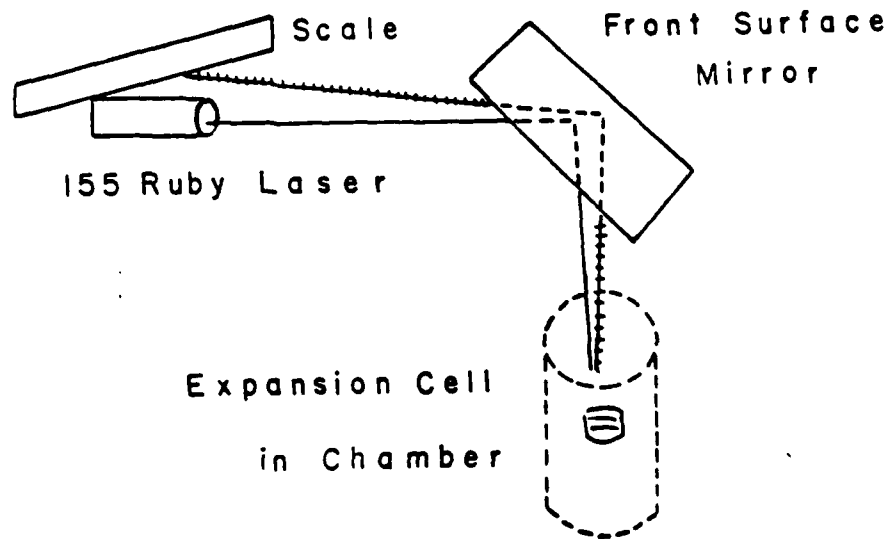


Figure 19. Schematic illustrations of thermal expansion apparatus
 A. Detail of sample in cell
 B. Line drawing of apparatus

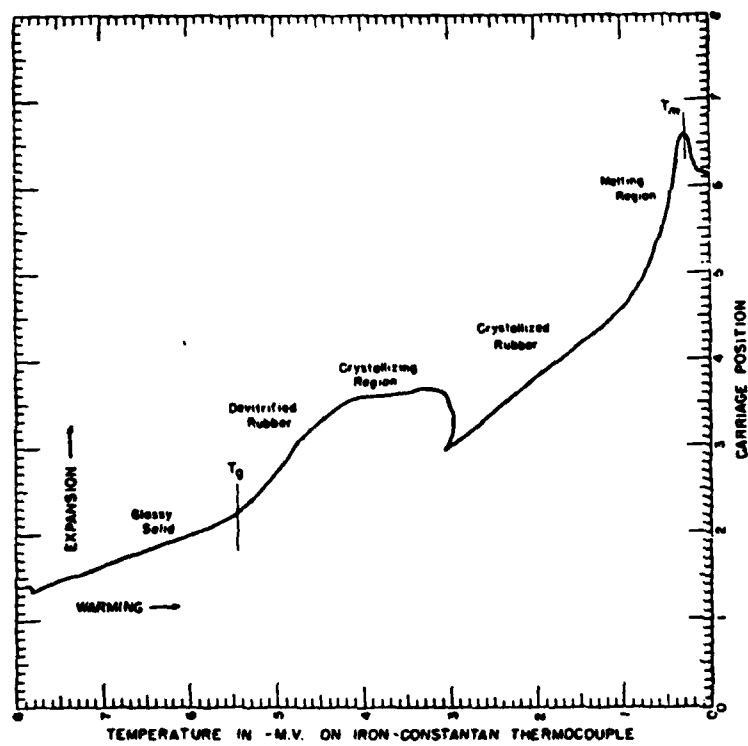


Figure 20. Typical differential thermal expansion curve for high cis polybutadiene rubber.⁷

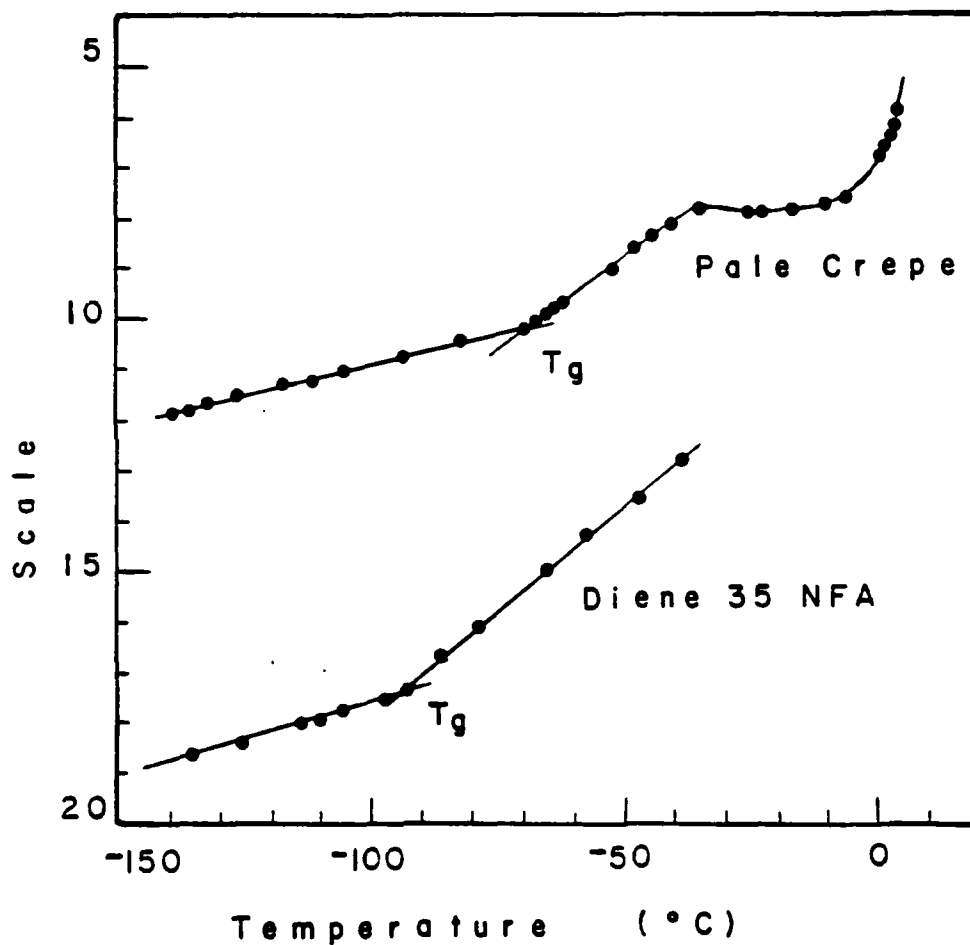


Figure 21. Thermal expansion curves for Diene 35NFA and Pale Crepe obtained on the apparatus described in Figure 19.

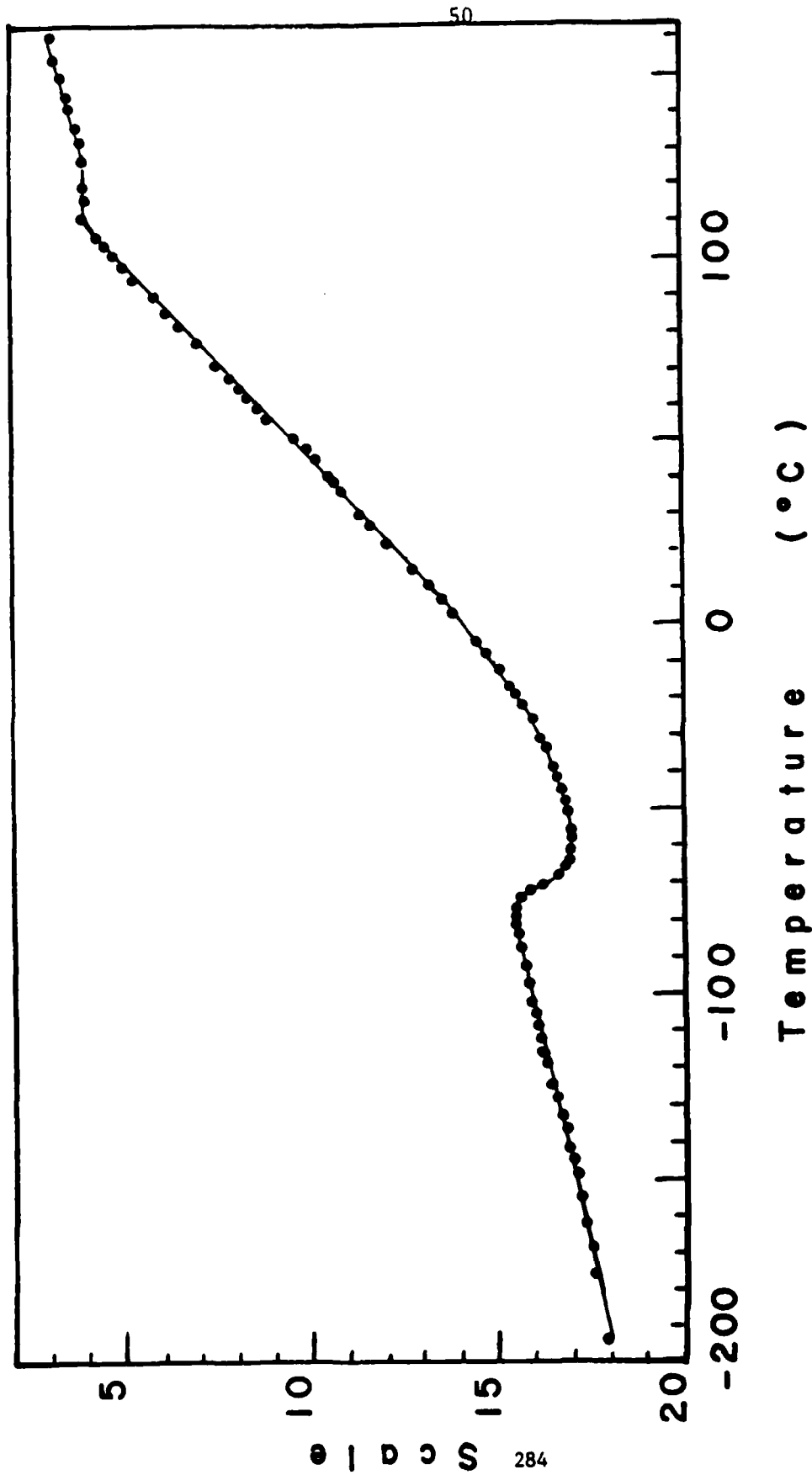


Figure 22. Typical thermal expansion curve obtained using sample TB₂₄, and the apparatus described in Figure 19.

MICROGRAPHS

- Plate 1 Nodules ranging in size from 100-400 nm. from a 4/3 TETA/EPON 828 surface after etching 24 hours with 1M CrO₃.
- Plate 2 Nodules of 100 to 200 nm. in size from a 4/3 TETA/EPON 828 impact fracture surface.
- Plate 3 An SEM micrograph of a crack initiation region from a 1/1 MDA/EPON 828 fracture surface. Note the fibrillar structures.
- Plate 4 Nodules taken from surface seen in Plate 3 after replication, near a fibril.
- Plate 5 Replica of surface seen in Plate 3. The end of a fibril which was torn from the surface. Note the directional flow of material towards the ridge.
- Plate 6 Replica of surface seen in Plate 3. A fibril torn from the surface overshadowing a ridge behind it.
- Plate 7 Replica of surface seen in Plate 3. A fibril above the ridge from which it emanated.



Plate 1. locules ranging in size from 100-400 nm from a 4/5 ETT/ETON 626 surface after etching 24 hours with 1% CrO₃.



Plate 2. Nodules of 100 to 200 nm. in size from a 4/3 TETA/EPON 828 impact fracture surface.



Plate 3. An SEM micrograph of a crack initiation region from a 1/1 MDA/EPON 828 fracture surface. Note the fibrillar structures.



Plate 4. Nodules taken from surface seen in Plate 3 after replication, near a fibril.



Plate 5. Replica of surface seen in Plate 3. The end of a fibril which was torn from the surface. Note the directional flow of material towards the ridge.



Plate 7. Replica of surface seen in Plate 5. A fibril above the ridge from which it emanated.

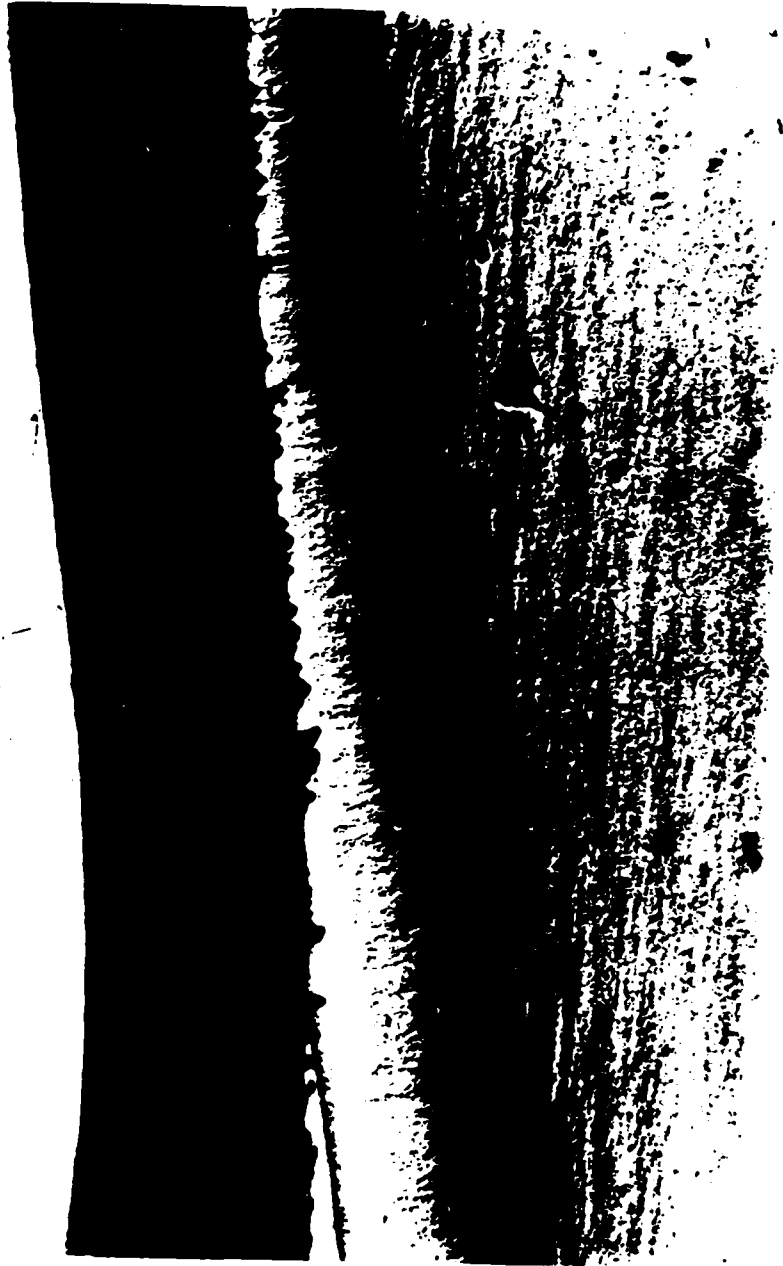


Plate 6. Replica of surface seen in Plate 3. A fibril torn from the surface overshadowing a ridge behind it.

Appendix 5.2
Numerical Studies of Crack Problems in Finite Elasticity

Dr. Eric Becker
Dr. Tinsley Oden
University of Texas

Science of Fracture Research Project
AFOSR Contract #49620-78-C-0101

School of Engineering
University of Pittsburgh
Pittsburgh, PA 15261

University of Texas Report will be submitted separately

Appendix 5.2

Numerical Studies of Crack Problems in Finite Elasticity

University of Texas at Austin
Institute of Numerical Analysis

Dr. Eric Becker
Dr. Tinsley Oden

Science of Fracture Research Project
AFOSR Contract #49620-78-C-0101

School of Engineering
University of Pittsburgh
Pittsburgh, PA 15261

Note: This report had not yet been received at
time of publication.

DATE
FILMED
— 8